Methods of Measuring and Simulating the Intracluster Light of Galaxy Clusters

Thesis submitted to the University of Nottingham for the degree of
Master of Philosophy, February 2024.

Jordan S. de-Ville

Registration Number: 20359819

Supervised by

Steven P. Bamford
Nina Hatch
Alfonso Aragón-Salamanca

Contents

List of Tables

List of Figures

Abstract

This thesis examines the Intracluster Light (ICL) of galaxy clusters, using both simulated and real observations. We, first, used data from the Millennium MAMBO lightcone to devise a method of simulating realistic images of the ICL for a given cluster. These simulated images may be used to infer the limiting capabilities of ICL detection codes, and to test whether reduction pipelines are suitable for ICL studies. They also allow users to further optimise their codes, as the input ICL variables are known.

We worked with the ICL science working group of the *Euclid* collaboration, using our method to simulate images compatible with the *Euclid*-VIS instrument, so that members could test their codes in preparation for the launch of *Euclid*. On inserting our images into a *Euclid*-VIS field mosaic image, which was processed with *Euclid*'s pipeline, we discovered that the standard pipeline produced images with a background that was not sufficiently flat at the levels required, and would have removed any ICL present in the images prior to reduction. The need for an alternative background subtraction method was subsequently suggested, which should be optimised for studies of faint, extended sources.

We then measured the ICL radial profiles for clusters in HSC-SSP images, and investigated how the ICL fraction changes as a function of cluster redshift and mass, using a sample of 72 clusters in the redshift range $0.1 \leq z \leq 0.8$. These clusters originate from two cluster catalogs: a sample of 18 XMM Cluster Survey (XCS) clusters, which are also included as part of a previous work (Furnell et al., 2021); and a sample of 54 clusters that are detected using the CAMIRA cluster-finding algorithm. Using HSC *i*-band data, we applied a surface brightness thresholding method to find an average ICL fraction of ~ 0.24, which is typical of clusters in this redshift range. It was also found that there was no correlation between the ICL fraction and cluster redshift nor the ICL fraction and cluster mass. The former is in disagreement with the previous work, which used the same XCS sample of clusters and HSC *i*-band data to find a well-defined anti-correlation. We argue that the disagreement may be due to: this work using a more refined method that corrects for contaminant photometric cluster galaxies being included in calculations; this work masking the BCG using segmentation data versus

the previous author using a fitting method; or this work using more recent data that has been processed in an optimal way for faint, extended sources - the previous work required 'divot corrections' to account for an overly harsh background subtraction in the HSC pipeline at the time. The lack of correlation established between ICL fraction and cluster mass comes as no surprise, as this is commonly found in ICL studies and can be explained using ICL formation models.

We finish by outlining a new ICL detection algorithm: `ficl`. This automated code makes use of the best aspects of the three most common ICL detection methods in tandem: surface brightness thresholding, profile fitting and wavelet filtering. We use `ficl` in its current, incomplete form on a simple toy model image, as proof of concept, to show that it is already capable of recovering 60% of the ICL that was put in to the model.

Acknowledgements

Chapter 1

Introduction

This thesis investigates the faint, diffuse component of galaxy clusters - the intracluster light (ICL). We use a combination of simulated and observed data to discern how/when the ICL might be formed, as well as its evolution as a function of both cosmic time and cluster mass. This is motivated by the prospect of a deeper understanding of cluster accretion history and the nature of dark matter and dark energy.

We propose two methods of disentangling the ICL from its native cluster: the first is based on a simple surface brightness (SB) threshold applied to the cluster, which we use to analyse a sample of 72 clusters out to a redshift $z = 0.8$; the second is, at this time of writing, a concept that combines the best aspects of existing methods, which may help in potentially solve some longstanding issues in ICL analyses. Perfecting such a method, as well as testing the accuracy of existing methods, requires test data that the user can tweak as they wish - i.e. realistically simulated images of ICL. Therefore, we also propose a method of simulating images of clusters with realistic ICL using lightcone data.

In this chapter, a comprehensive background of the ICL is given, along with the relevant literature. Chapter 1.1 addresses the properties of the ICL, including its relationship with the brightest cluster galaxy (BCG), its relationship with the cluster and and its connection with dark matter and (potentially) dark energy. In Chapter 1.2 the difficulties in observing and subsequently measuring the ICL are outlined, along with popular existing methods that attempt to isolate the ICL from its cluster. The method of simulating realistic images of ICL is contained within Chapter 2, which also includes preparatory work for the *Euclid* collaboration's ICL science working group (SWG). Chapter 3 concerns measuring the ICL using a SB threshold method and presents the results and analysis on 72 HSC galaxy clusters in the *i*-band. A new, improved method for measuring the ICL is discussed in Chapter 4, which combines various aspects of

existing methods. The progress to date is presented, including some preliminary results on a simple toy model. Finally, the conclusions of this thesis are outlined in Chapter 5, along with future work.

Throughout this thesis, where applicable, we adopt a standard ΛCDM cosmology, with parameters: $H_0 = 70 \text{kms}^{-1} \text{Mpc}^{-1}$, $\Omega_M = 0.3$, $\Omega_\Lambda = 0.7$, $h_{100} = 0.7$.

1.1 Intracluster Light (ICL)

During the first half of the 20th century, Fritz Zwicky began his research into groups and clusters of galaxies. While studying the Coma cluster he noticed that to account for its large velocity dispersion, the density of luminous matter should be greater than 400 times that derived from observations (Zwicky, 1933). It was in this paper where the phrase *dark matter* was first used to describe this missing mass and Zwicky was keen to try and account for its existence. Just four years later, Zwicky postulated a potential solution to the missing mass problem: a faint component in galaxy clusters formed by stars that are stripped from galaxies, that fill the space between the galaxies (Zwicky, 1937). The existence of this stellar halo was indeed confirmed a few years later, as Zwicky observed a faint, diffuse and extended component in the Coma cluster (Zwicky, 1951). However, it was realised soon after this discovery that this faint envelope of light was not capable of accounting for the mass-to-light ratios of galaxy clusters (e.g. de Vaucouleurs, 1960; Oemler, 1973).

While Zwicky's discovery of the faint, diffuse component of galaxy clusters (intracluster light, or ICL, hereafter) did not solve the missing mass problem, it opened up a new avenue of research. More and more studies were made on the ICL (e.g. Matthews et al., 1964; Arp & Bertola, 1969; de Vaucouleurs & de Vaucouleurs, 1970; Mattila, 1977; Melnick et al., 1977; Thuan & Kormendy, 1977); however, these were limited studies due to observations at the time being made using photographic plates and photomultiplier tubes. Since the advent of CCD chips, it has become easier to study the ICL due to deeper, higher quality data (the first study that use CCD imaging for ICL studies was that of Bernstein et al., 1995). This has led to an abundance of studies that have scrutinised the ICL, giving more insight into its properties and its potential as a cosmological probe.

1.1.1 The ICL and its Cluster

Typically, the Intracluster Light (ICL) contributes between ~5-50% to the total optical cluster light (e.g. Jiménez-Teja et al., 2018; Kluge et al., 2021; Ragusa et al., 2021;
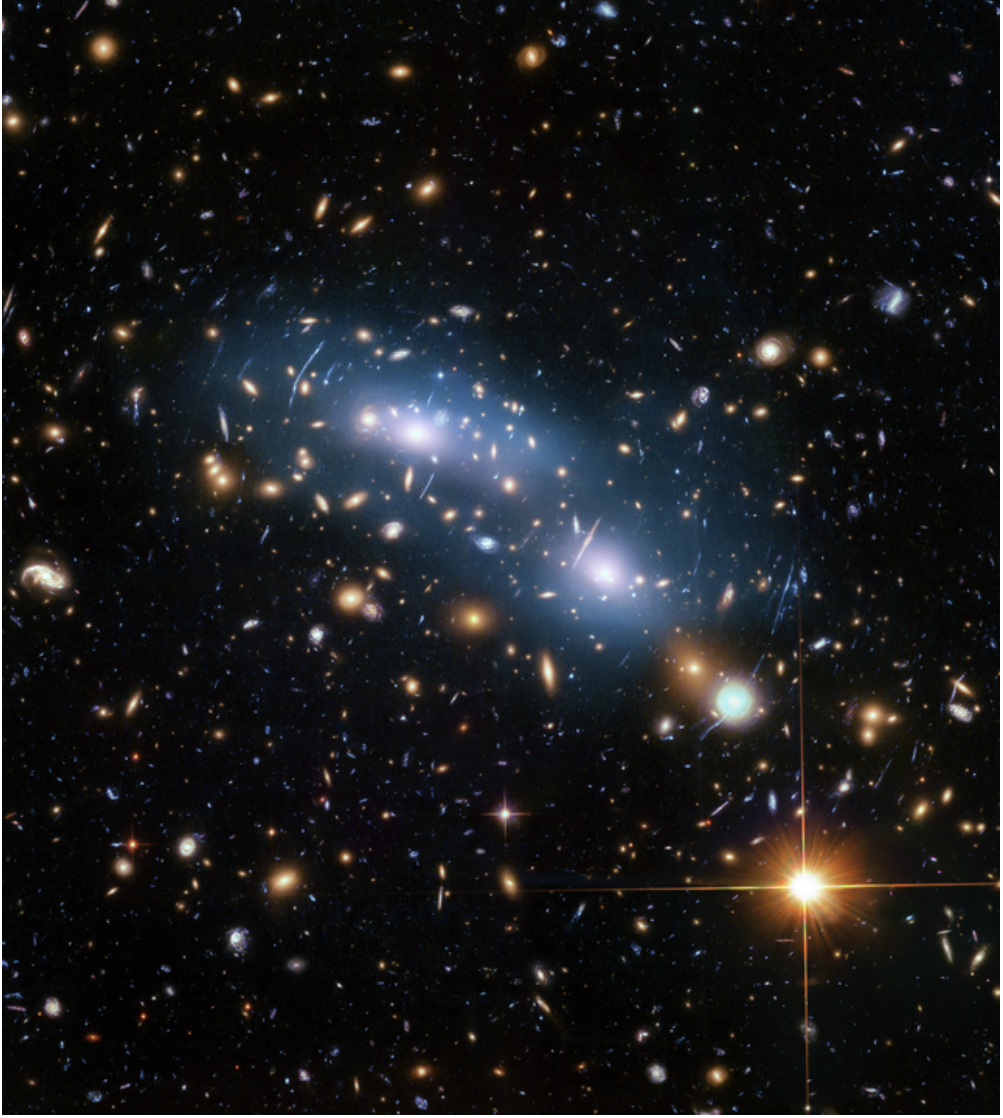
Figure 1.1: Galaxy cluster MACS J0416.1-2403 ($z \sim 0.4$) taken from the Hubble Frontier Fields program. The faint, diffuse light is shown in blue, and is most strongly concentrated around the two central galaxies. *Credits: NASA, ESA and M. Montes*.

Furnell et al., 2021), i.e. the sum of the luminous contributions from cluster galaxies and the ICL. Figure 1.1 shows an example of a galaxy cluster with ICL that is clearly visible. There are various physical processes by which the ICL may form over time in the cluster. How important each of these processes are may be inferred from the stellar colours/populations of the ICL.

Tidal forces within galaxy clusters may strip the outskirts of massive galaxies or even completely rip apart low-mass satellites (e.g. Peng et al., 2011; Jiménez-Teja et al., 2018, 2019). Both processes should create a radial colour gradient in the ICL, going from red at small cluster radii to blue at large cluster radii:

- **Stripping of massive galaxies:** Massive galaxies have internal colour gradients (La Barbera et al., 2012), meaning that the metallicity of stars that are liberated from these galaxies is related to the galactocentric radius at which they are stripped. In galaxy clusters, tidal forces tend to be stronger nearer the centre, meaning that deeper, redder stars are stripped at small cluster radii while bluer stars from the outskirts of these galaxies are stripped at larger cluster radii.

- **Disruption of dwarf satellites:** Low-mass dwarf galaxies have low metallicities (Zaritsky et al., 1994, this means that they are bluer in colour). Therefore, tidal forces at large cluster radii are capable of tearing apart low-mass, blue dwarfs (Melnick et al., 2012).

Indeed, these colour gradients are observed (e.g. Iodice et al., 2017; DeMaio et al., 2018), meaning that tidal stripping of galaxies is evidently an important contributor to the formation of ICL. However, it appears that the stripping of massive galaxies may contribute significantly more stars to the ICL (e.g. Montes & Trujillo, 2014), because the number of dwarf galaxies required to account for the total luminosity of the ICL may drastically alter the cluster luminosity function (DeMaio et al., 2018). Nevertheless, theoretical models that are able to reproduce the observed metallicity gradients predict that the stripping of low-mass galaxies ($9 < \log{(M/M_\odot)} < 10$) is the most important contributor at the early stages of ICL formation (Contini et al., 2019).

As well as tidal stripping, stars may be ejected from galaxies undergoing major mergers with the central brightest cluster galaxy (BCG), via violent relaxation (Murante et al., 2007; Lidman et al., 2013). If this ICL formation channel is dominant, the major mergers will abolish any existing stellar colour gradient (Di Matteo et al., 2009; Eigenthaler & Zeilinger, 2013), meaning that an observed flat stellar colour gradient will imply that this process is most important. This has been observed in a sample of 10 galaxy clusters going out to redshift $z = 0.3$ (Krick & Bernstein, 2007); however, this sample was incomplete at high redshifts (it did not include low-mass, low-luminosity, low-density, high-redshift clusters due to sensitivity limitations), leaving only 5 clusters that were unaffected by selection-bias. Therefore, it is impossible to say whether these clusters were fully representative of the entire range of cluster properties.

The ICL may also grow as a result of accretion of pre-processed ICL from infalling groups onto the galaxy cluster (Rudick et al., 2006). In this scenario, the ICL fraction rises sporadically, increasing at every accretion event. Figure 1.2 shows the growth of the ICL component as 4 massive groups collapse to form one massive complex, taken from an N-body simulation. Observationally, it is impossible to track every accretion event onto any particular cluster; however, a recently merged system will exhibit substructures (e.g. see the work of Mohammed et al., 2016).
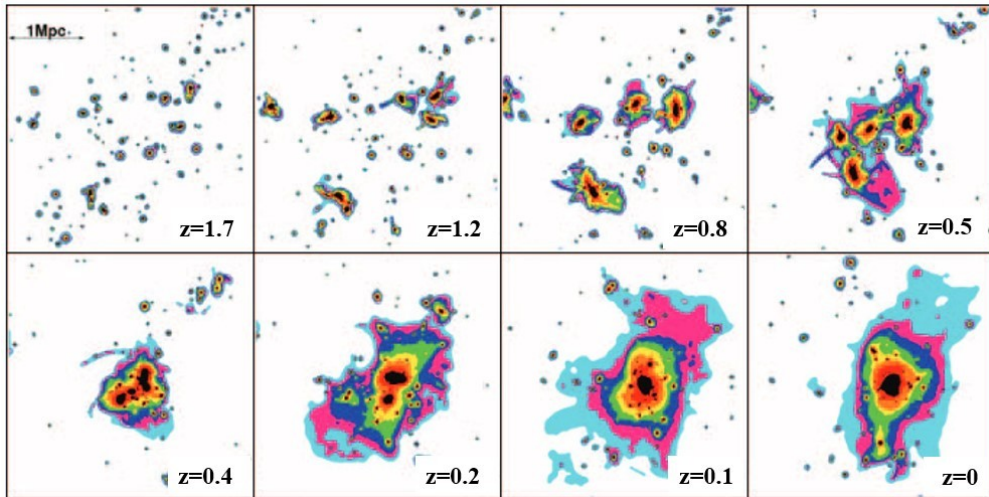
Figure 1.2: Figure 6 from Rudick et al. (2006), modified to show the redshifts of each step. Growth of the ICL due to 4 massive groups collapsing to form one massive complex. The colours represent the ICL of decreasing surface brightness from black to light blue. The groups are well-pronounced by $z = 0.8$, and, by $z = 0.4$, have collapsed to form a very massive, concentrated structure. By $z = 0$, the combined ICL has mixed to form a single, smooth, diffuse component.

The last, perhaps least dominant, formation channel of the ICL is by means of in-situ star formation from infalling gas clouds (e.g. Puchwein et al., 2010). This may be associated with faint, diffuse UV emissions (Hatch et al., 2008), but identifying these star-forming regions is difficult because of current UV detection limits.

It has been suggested that, by $z = 0$, almost half of the member galaxies within a cluster have been accreted in galaxy groups (Bahé et al., 2013). This means that the pre-processed ICL in these groups may contribute a significant amount to the cluster ICL fraction, particularly below $z = 1$ (as found in Rudick et al., 2006). In fact, Contini et al. (2014) showed in simulations that up to ~30% of the ICL in clusters may have originated from pre-processed ICL from accreted groups. Therefore, studying how the ICL fraction depends on total cluster mass may offer an insight into this mechanism, since one might expect more massive systems to have accreted more groups and thus more pre-processed ICL.

Observational studies are inconclusive as to whether there is a relation between cluster mass and ICL fraction: some see no correlation at all (e.g. Krick & Bernstein, 2007; Burke et al., 2015; Ragusa et al., 2021), while others see a clear increase of ICL fraction with increasing cluster mass (e.g. Jiménez-Teja et al., 2018; Zhang et al., 2019; Sampaio-Santos et al., 2021). This inconsistency is mirrored by theoretical models as some predict a positive correlation (e.g. Lin & Mohr, 2004; Murante et al., 2007; Purcell et al., 2007), others no correlation (e.g. Henriques & Thomas, 2010; Contini et al., 2014), and even a negative correlation has been found (Cui et al., 2014). It is possible

that the theoretical models do not show consistent results due to intrinsic differences in the simulations. Also, there is an important caveat to consider and that is that the ICL fraction can vary dramatically depending on what radius the ICL is defined, which differs in each study.

The inconsistencies in the relation between the ICL fraction and the total cluster mass may be explained, in part, in terms of the concentration of the cluster and the evolutionary stage of the cluster. Contini et al. (2014) used simulations to demonstrate that the ICL fraction increases strongly with both how concentrated the cluster is[1] and how evolved the cluster is. The latter relation particularly stands out here: *the ICL is an excellent tracer of the dynamical evolutionary stage of galaxy clusters* (see also Aguerri et al., 2006; Da Rocha et al., 2008).

1.1.2 The ICL and the Brightest Cluster Galaxy (BCG)

The ICL component is strongly believed to be related to the BCG – the galaxy that resides at the barycenter of the cluster, which tends to also be the most massive and extended – because it is often mostly concentrated around it (Mihos et al., 2005; Arnaboldi et al., 2012). Furthermore, the BCG and ICL component are usually well-described by the same Sérsic profile within the central region of the cluster (Gonzalez et al., 2005; Seigar et al., 2007).

However, at larger radii the ICL shows a growing ellipticity with radius (Gonzalez et al., 2005; Huang et al., 2018; Montes et al., 2021) and can also exhibit a position angle that deviates from that of the BCG (Kluge et al., 2021), meaning that the ICL and BCG stellar components must be truly different from one another. This is kinematically confirmed by integrated light spectroscopy (Edwards et al., 2016; Gu et al., 2020) and planetary nebula kinematics (Arnaboldi et al., 1996; Longobardi et al., 2018) of several nearby BCGs, which show that the velocity dispersions of stars within the BCG increase radially until they eventually match the velocity dispersions of cluster galaxies. This is consistent with ICL stars being bound to the cluster's dark matter halo.

The ICL is formed during the hierarchical buildup of its cluster, due to interactions that strip galaxies of their stellar content (see, for example, Rudick et al., 2010). Therefore, characterising the ICL reveals the assembly history of its cluster and, since the ICL and BCG are strongly associated with one another, understanding the ICL is key to understanding how the BCG grows with time.

---

[1]Defined as the ratio between scale radius (assuming a Navarro-Frenk-White, NFW, profile) and virial radius, R_{200}.
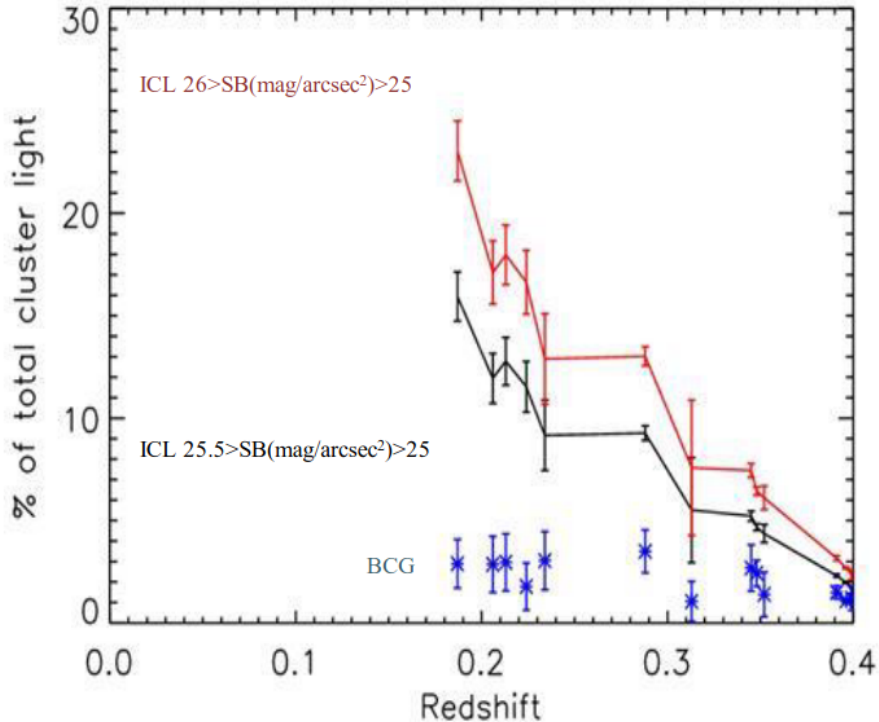
Figure 1.3: Figure 5 from Burke et al. (2015). Contributions of the ICL (taken in two different surface brightness slices) and the BCG light to the total light of 13 galaxy clusters over the redshift range $0.19 < z < 0.40$, taken from Hubble's CLASH survey. A steep growth with decreasing redshift is exhibited by the ICL component, while the BCG shows very little growth.

While the central regions of BCGs are expected to have formed at high redshifts and on short timescales (Dubinski, 1998), the outer regions of BCGs are likely formed as a result of accretion from multiple minor mergers over time (Trujillo et al., 2011). Observations show that BCGs tend to be fully assembled at redshift $z \sim 1$ (Collins et al., 2009), and they show very little (if any) mass growth between $0 \lesssim z \lesssim 1$ (Lidman et al., 2012; Burke et al., 2015; Zhang et al., 2016). This is in contrast with the ICL, which can show significant growth since $z = 1$ (see Figure 1.3, for example).

Theoretical models that come in the form of N-body simulations (e.g. Rudick et al., 2006) and semi-analytic models (e.g. Contini et al., 2018) also predict that the ICL should show significant growth since $z = 1$; however, they over-estimate the mass growth of BCGs, predicting a growth rate of 3-4 since $z = 1$ (De Lucia & Blaizot, 2007). In order to alleviate this tension between theory and observations, it is often assumed that many of the stars that are accreted onto the BCG actually end up forming part of the ICL (Laporte et al., 2013; Contini et al., 2018). This resolution highlights the strong relation between the ICL and BCGs.

1.1.3   The ICL as a Dark Matter Tracer

As already discussed, the ICL is formed by stripping galaxies of their stellar content. These stars remain unbound to any particular galaxy in the cluster, and so are freely floating in the DM halo potential well. Because DM particles are collisionless, and it is also reasonable to assume that the stars in the ICL are collisionless, the ICL should serve as a dark matter distribution tracer in galaxy clusters.

Though this area of ICL science has only seriously been probed over the past few years, there are some older studies that made the link between the ICL and the DM within galaxy clusters. For example, Zibetti et al. (2005) fit an NFW profile to the ICL spatial distribution in their sample of nearly 700 galaxy clusters. A decade later, Giallongo et al. (2015) were perhaps the first to make the suggestion that the ICL may be used to trace the DM distribution in clusters. This has been confirmed to be the case in one dimension by Sampaio-Santos et al. (2021), who compared the ICL surface brightness profiles of 528 galaxy clusters to their dark matter profiles (constructed using weak-lensing data), using data from the Dark Energy Survey in the redshift range $0.2 \leq z \leq 0.35$. They found that these profiles were comparable, indicating a strong relation between the dark matter distribution and the ICL.

It was Montes & Trujillo (2019) who published the first study that explicitly showed that the ICL follows the same global distribution of the DM halo in three dimensions. In their study, they used a sample of 6 Hubble Frontier Fields clusters to compare the distributions of: the DM (from gravitational lensing measurements), the ICL, and the cluster's hot gas content (from X-ray emissions), using a method known as the 'Modified Hausdorff Distance' (MHD). Figure 1.4 shows the results from one of the clusters they studied. Two of the main findings, most relevant here, were that: the X-ray emissions from the hot intracluster gas cannot be used as a global DM distribution tracer for unrelaxed clusters because gas is highly collisional, meaning that it is delayed in settling into the DM potential (hence the offset in Figure 1.4); the ICL and DM distributions are strongly connected. Follow-up theoretical work (also using the MHD method) by Alonso Asensio et al. (2020), using a set of 30 clusters simulated using the Cluster-EAGLE hydrosimulations (Barnes et al., 2017), confirmed the findings of Montes & Trujillo (2019). They, too, found that the *baryonic* matter distribution is not traced by the ICL distribution. The same conclusions have also been established by Yoo et al. (2022), who used a different method of comparing spatial distributions of the ICL and dark matter on 6 clusters selected from the Galaxy Replacement Technique simulation (Chun et al., 2022), which is specifically tailored to studies of the ICL.

Recently, Deason et al. (2021) argued using simulations that the ICL boundary may be closely related to the boundary of the DM halo, the "Splashback radius". This has been

somewhat confirmed observationally by Gonzalez et al. (2021), who found a potential splashback feature in the surface brightness profile of the ICL in MACS J1149.5+2223 ($z = 0.54$), at around 1.4Mpc from the centre of the cluster. If confirmed, then the ICL may be used to determine some of the physical parameters of the DM. Furthermore, it may even be used as a test of modified gravity and dark energy, since the splashback radius is sensitive to these phenomena (Contigiani et al., 2019).
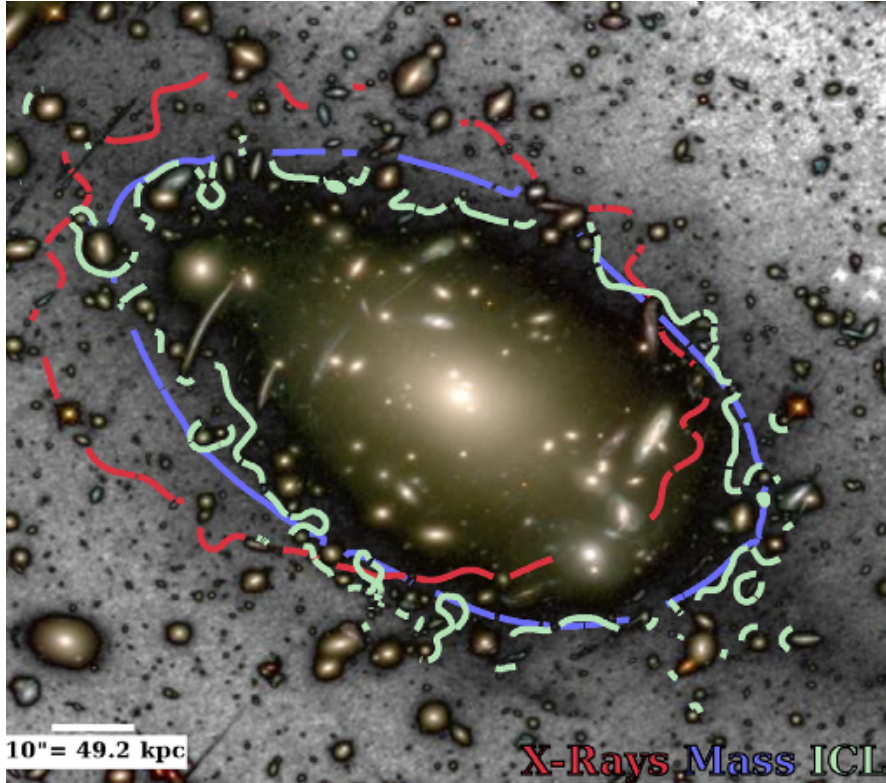
Figure 1.4: Taken from Figure 3 of Montes & Trujillo (2019). Comparisons of the distributions of the DM, the ICL and the hot gas in Abell S1063. The relevant contours are colour-coded as red (intracluster gas), blue (dark matter) and green (ICL).

Motivated by the science discussed in Section 1.1.1, I use a sample of Hyper-Suprime Camera clusters in the *i*-band to investigate the ICL properties as a function of cosmic time and cluster mass/richness, which is the topic of Chapter 3.

1.2 Difficulties in Detecting the ICL

1.2.1 Problems Faced by Surveys

Observing such a faint, extended surface brightness feature (typically 1% of the brightness of the night-sky or even fainter, e.g. Bernardi et al., 2017) comes with its limitations. Historically, most surveys have not been designed to operate in a way to optimise

their detections of low surface brightness features, giving large statistical uncertainties. One way of handling statistical uncertainties present in ICL studies is to stack the data from a large sample of clusters, with their ICL normalised (as in Zhang et al., 2019). However, this averages out any structures within individual clusters.

Estimating and subtracting the background poses further difficulties. The most common method (as implemented in Source Extractor, or SExtractor; Bertin & Arnouts, 1996) divides images into a grid of sections, with the size of each section specified by the user. SExtractor makes a first pass by estimating the local background in each section (covering the whole frame), using a combination of kappa-sigma-clipping and mode-estimation[2]. If the mode and clipped median statistic disagree by more than 30%, SExtractor falls back to a simple median for estimating the local background. Each section then has a median filter applied to it, suppressing any local flux spikes, and a spline is fitted to the data. Interpolating between each section gives the background map, which is ultimately subtracted from the image. Choosing the size of the sections presents a trade-off of undesired outcomes: if the sections are too small SExtractor will over-subtract the flux around extended objects, if the sections are too large SExtractor cannot model spatial variations in the background level, leading to an inaccurate representation of the global background map. The former case occurs most often (see, for example, section 5.8.5 of Aihara et al., 2018b), which can lead to significant underestimates of the ICL (e.g. Zackrisson et al., 2009; Krick et al., 2012). Akhlaghi & Ichikawa (2015) have put forth a promising alternative sky background estimator in *Noise Chisel*, which is a noise-based non-parametric technique primarily used for detecting irregular galaxies and their substructure (see Figure 2 of the paper for its implementation).

Finally, there are a variety of observational artefacts that may contaminate ICL measurements. Some examples of these are: satellite trails (see, for example, top panel of Figure 3 in Singhal et al., 2021), ghosts (see, for example, Figure 3 in Bosch et al., 2018), and PSF wings from bright stars (these are addressed in relation to the ICL in DeMaio et al., 2018; Montes & Trujillo, 2018). The latter here may be rectified by accurately modelling the PSF, which is by no means an easy task; however, accounting for the vast majority of flux contaminants from observational effects in an automated way is extremely complicated (Duc et al., 2015), with most diluting into the final coadd images. This, along with the other issues discussed here, presents a huge task for future pipelines, in order to generate pristine data for the most intricate ICL studies.

In Chapter 2 I show how I simulate realistic ICL for testing ICL detection codes, with reference to some preparatory work I was involved in with the *Euclid* collaboration. I will also show that, because *Euclid*'s standard pipeline is optimised for purposes out-

---

[2]see `https://sextractor.readthedocs.io/en/latest/Background.html` for full details.

side of studying faint, extended features, ICL studies using *Euclid*-imaging requires an alternative data processing pipeline.

1.2.2 The Ill-Defined ICL

It is widely accepted that the ICL is formed by stars that are stripped from cluster galaxies, and these stars remain bound to the potential of the cluster, rather than any of its constituent galaxies. However, because it is impossible to resolve the individual stars of the ICL, astronomers must come up with observational-based methods of disentangling the ICL from its cluster – in particular, the BCG to which it is associated. These methods are usually derived from parameter-based priors, which can involve strong assumptions about the ICL, resulting in differing amounts of ICL and indirect comparisons between studies that use different methods. Here, the three most common observational techniques will be addressed, with examples for each.

It is worth noting that theoretical methods exist, capable of separating the ICL from its cluster, but these require a wealth of information about the cluster that is only available using simulated data. Since this thesis only concerns ICL from an observational perspective, I will only go as far as listing a few relevant references: using the 'binding energy' of stars in the ICL (Dolag et al., 2010; Murante et al., 2004, 2007; Sommer-Larsen et al., 2005); using the mass density of stars in the ICL (Rudick et al., 2009, 2011); tracking the stellar-stripping from satellite galaxies and violent mergers using a semi-analytic model (Contini et al., 2018, 2019).

Surface Brightness Thresholding

The simplest technique to separate out the ICL from its cluster is to define a cut in the surface brightness (dependent on the band of the observation): pixels with values lower than this cut are assigned to the ICL, while pixels above the threshold are assigned to cluster galaxies. This technique is susceptible to contamination from the faint outskirts of galaxies and extended wings of the PSF, leading to an over-estimation of the total ICL light (Presotto et al., 2014). However, avoiding contamination by reducing the threshold dramatically reduces the area from which the ICL signal may be recovered.

It is possible to alleviate this issue by applying a fainter surface brightness threshold to everything except the BCG, which is commonly defined by a *B*-band cut of $\mu_B \sim$ 25mag arcsec^{-2} (e.g. Feldmeier et al., 2004; Krick & Bernstein, 2007; Presotto et al., 2014; Burke et al., 2015; Furnell et al., 2021).

Parametric Fitting

A more computationally-demanding alternative is to fit parametric surface-brightness profiles to the galaxies, e.g. as a double/triple Sérsic (Sérsic, 1963), then subtract these from the image to leave behind the ICL (e.g. Gonzalez et al., 2005; Zhang et al., 2019; Kluge et al., 2021; Montes et al., 2021). However, if the ICL is not explicitly included in the model, then the optimisation will attempt to use the outskirts of galaxies to remove the diffuse light. On the other hand, adopting a specific parametric form for the ICL makes strong assumptions, compromising the utility of the results.

Recently, Zhang et al. (2019) found that the ICL could be represented by a triple Sérsic fit. They used a stacked surface-brightness profile of ∼ 300 Dark Energy Survey (DES) clusters at $z \sim 0.25$ and found that: a core component is dominant in the ICL within 10kpc of the cluster centre; between 30kpc and 100kpc a bulge component dominates; beyond 200kpc a diffuse component dominates the ICL. The sum of these well-describes the stacked profile (see Figure 1.5).
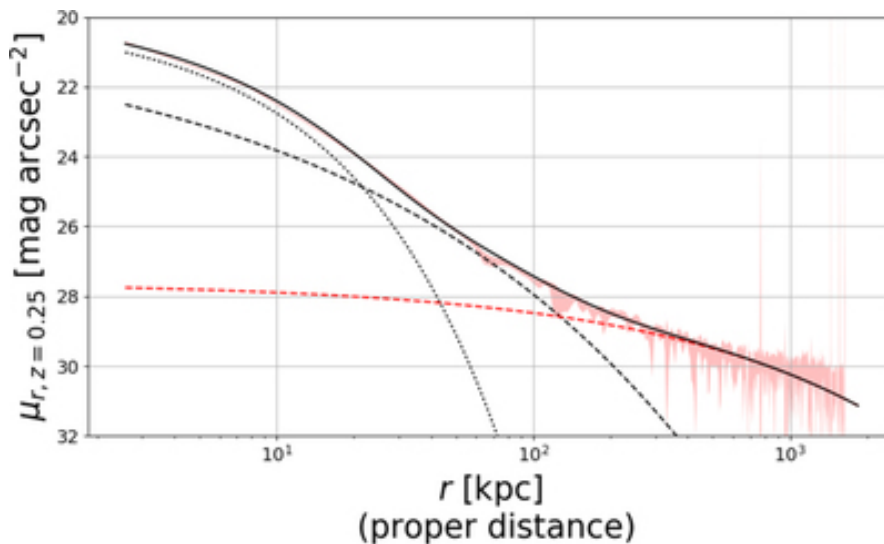
Figure 1.5: Taken from Figure 10 of Zhang et al. (2019). The stacked surface-brightness profile of the ICL of 300 DES clusters (shaded red), fitted by a triple-Sérsic profile (black solid line), composed of: a core component (black dotted line), a bulge component (black dashed line) and a diffuse component (red dashed line).

Non-Parametric Fitting (Wavelet Analysis)

Another approach is to perform wavelet-filtering to remove objects on specific scales (small galaxies), while retaining large scale features (the ICL). This kind of analysis was first utilised by Slezak et al. (1994), when they investigated substructures of 11 X-ray clusters of galaxies. In recent years, there have been several examples of wavelet-based analyses of ICL (see, for example, Adami et al., 2005; Guennou et al., 2012;

Ellien et al., 2021). However, users must be cautious as such algorithms can run into difficulties when images contain galaxies of similar size to the ICL.

Figure 1.6 shows a comparison of the resulting ICL when using each method outlined here, applied to two different clusters.
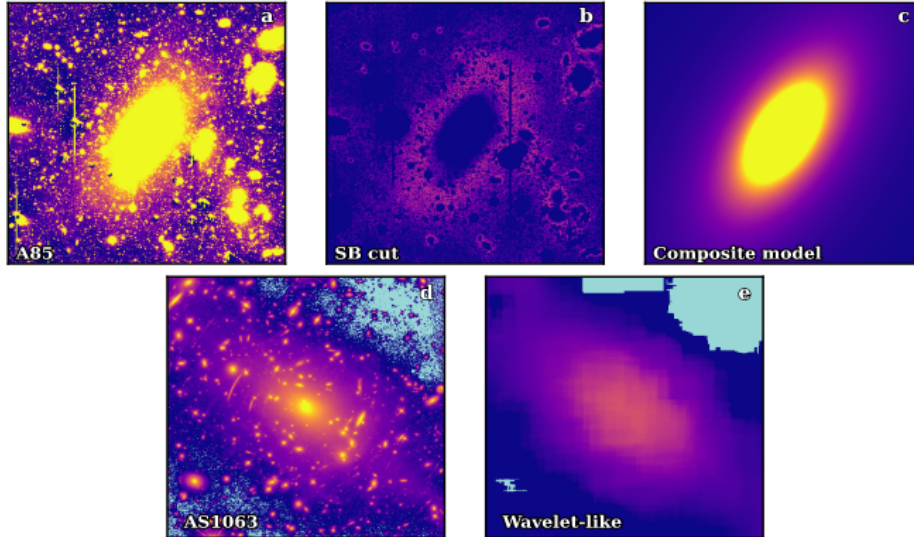
Figure 1.6: Taken from Figure 1 of Montes (2022), individual references therein. Resulting ICL extracted from Abell 85 (top row) and Abell S1063 (bottom row), using different techniques: (panel b) surface brightness thresholding to define the ICL, (panel c) parametric fitting of galaxies and ICL using Sérsic profiles, and (panel e) non-parametric fitting using wavelet analysis.

In Chapter 4, I outline the concept of a new ICL detection code currently under construction. This code combines elements of each of the three detection methods discussed in this section, and it hopes to offer an automated, non-parametric way of separating out the ICL from its cluster and the BCG.

1.2.3 Outline of Thesis

In Chapter 2 I begin by providing a method of simulating realistic images of galaxy clusters that contain ICL, followed by preparatory work I did for *Euclid*'s ICL science working group. This work involved simulating images using *Euclid* instrumentation, so that different ICL codes could be tested prior to launch. The suitability of *Euclid*'s standard data processing pipeline for ICL studies is also discussed, along with ongoing/future work.

Chapter 3 concerns the work I did on implementing an automated surface brightness thresholding method to measure the ICL. After giving a detailed description of the code, I apply this method to 72 galaxy clusters in the redshift range $0.1 \leq z \leq 0.8$,

originating from two different catalogs (the XMM Cluster Survey, Romer et al. 2001, and CAMIRA, Oguri 2014; Oguri et al. 2018), using HSC *i*-band data. The results are examined for correlations between ICL and cluster properties, and compared with other studies that use clusters with similar mass and redshift range. The Chapter ends with a discussion of suggested future work, which will ultimately lead to a paper.

In Chapter 4 I outline a new method of measuring the ICL, which combines the advantages of existing methods in a hybrid approach. The code is yet to be completed at this time of writing, but the work done to date is set out and proof-of-concept results are provided. The next steps in finalising the code are given, along with subsequent future work.

Chapter 2

Simulating Realistic ICL and *Euclid* Preparatory Work

2.1 Overview

The upcoming *Euclid* survey will provide an excellent sample of clusters to study the ICL in depth. *Euclid* consists of a 1.2m-aperture telescope with two instruments: the visual imager (VIS) and the near-infrared spectrometer and photometer (NISP). Over a third of the celestial sphere will be covered by the *Euclid* survey over a 6 year period; the VIS instrument's wide field of view (0.787deg×0.709deg), spectral resolution (0.1arcsec) and sensitivity (25mag) makes *Euclid* an ideal candidate for optical studies of the ICL. Moreover, *Euclid* will operate on a large halo orbit at Lagrangian point 2 (L2), which will be highly stable - this is very ideal for observing faint surface brightness features. I was involved in a project with the ICL science working group in *Euclid*, testing ICL detection codes in preparation for *Euclid*'s launch. The objectives were: to forecast for what range of cluster masses and redshifts *Euclid*'s VIS camera will be able to detect ICL, to test the effect of the reduction pipeline's background subtraction and develop suitable alternatives, and to evaluate and compare the performance of different ICL detection codes within the group.

In order to forecast what range of cluster redshifts and masses *Euclid* will be able to detect ICL, we required realistic images that contained stars, galaxies, clusters and ICL. These needed to be simulated using the appropriate instrumentation (in our case, that of *Euclid*'s VIS camera) and reduced using the same pipeline that *Euclid* will use on real data. Note that the standard pipeline, which was still in development at this time of writing, is focused on measuring accurate ellipticities and position angles of small galaxies, for weak-lensing measurements. We had access to the most up-to-date and realisti-
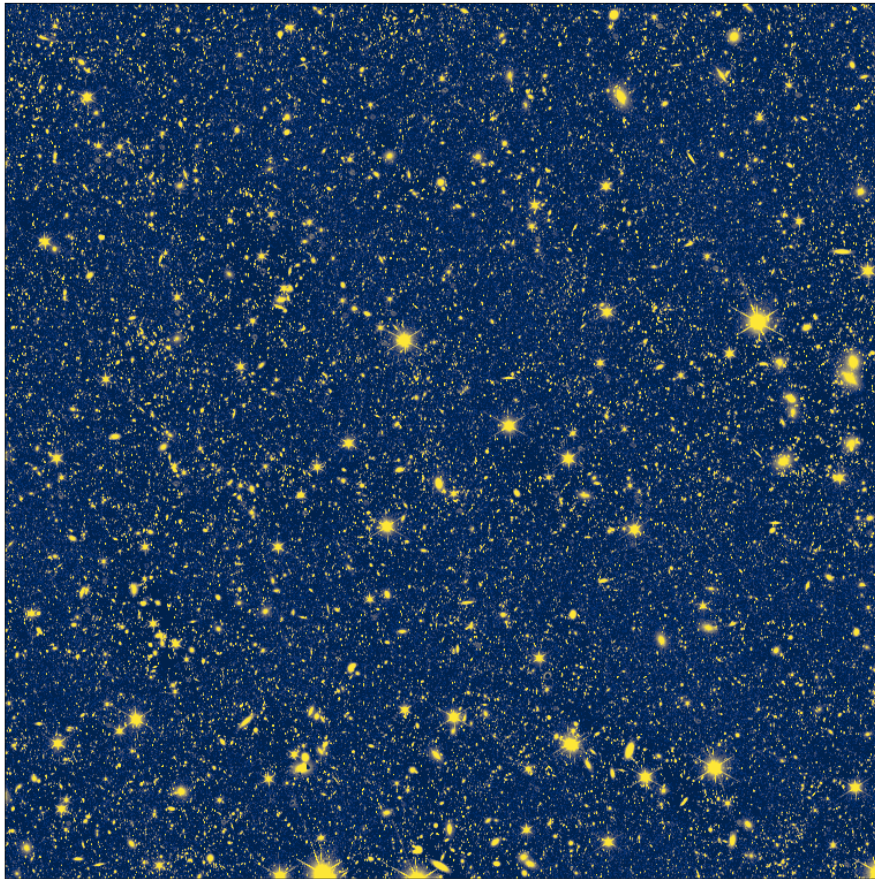
Figure 2.1: The simulated mosaic image from *Euclid* that we place our cluster image onto. This image has been simulated using the instrumentation of *Euclid*'s VIS instrument, and has been processed via the data reduction pipeline. The mosaic covers an area of $0.53° \times 0.53°$ on the sky.

cally simulated images from *Euclid* that had been processed by the reduction pipeline. Though these contained realistic stars and galaxies, they did not contain galaxy clusters with ICL (this is probably due to the fact that observing faint surface brightness features is not a primary objective of *Euclid*).

Therefore, this chapter concerns work done on simulating images of galaxy clusters that contain ICL, which were added on to one of the realistically simulated *Euclid* images (the one we used is shown in Figure 2.1). However, this work was interrupted when we found that the pipeline was too harsh in its background subtraction (discussed later on in the chapter). Since this issue was being handled by other members of the group, I moved away from this project to focus on my own work, and so I will only discuss work that was done up to this point here.

2.2 Simulating Images of Clusters with ICL

The data we used to simulate the cluster galaxies were taken from the Millennium MAMBO lightcone. This lightcone is generated based on the full dark-matter Millennium simulation (Springel et al., 2005), using semi-analytical models of galaxy formation from Henriques et al. (2015), consisting of realistic galaxy properties from the Empirical Galaxy Generator (EGG; Schreiber et al., 2017). The relevant parameters we obtained for each galaxy from the lightcone were: positions on the sky (RA/dec), AB apparent magnitudes in the *Euclid*-VIS band, bulge-to-disk stellar mass ratios, bulge half-light radii, disk half-light radii, bulge axis ratio, disk axis ratio. We sampled position angles and Sérsic indices (Sérsic, 1963) from random distributions.

We modelled the galaxies as two-component, bulge+disk Sérsic profiles. In order to obtain realistic Sérsic indices for every cluster galaxy, we, first, created a cumulative distribution function (CDF) using a sample of observationally inferred Sérsic indices of bulges (n_{bulge}), taken from Kennedy et al. (2016), while assuming exponential profiles for each disk (i.e. $n_{disk} = 1$; this is also in line with the work of Kennedy et al. (2016)). We then randomly sampled the n_{bulge} from the resulting probability density function (PDF). It is worth noting that `Galsim` struggles to create images corresponding to $n \geq 6$ profiles, so we had to limit n_{bulge} accordingly. Figure 2.2 shows the distribution for 4000 bulge Sérsic indices. The position angle (ϕ) for each galaxy was randomly sampled from a uniform distribution, between $0 \leq \phi \leq 2\pi$.
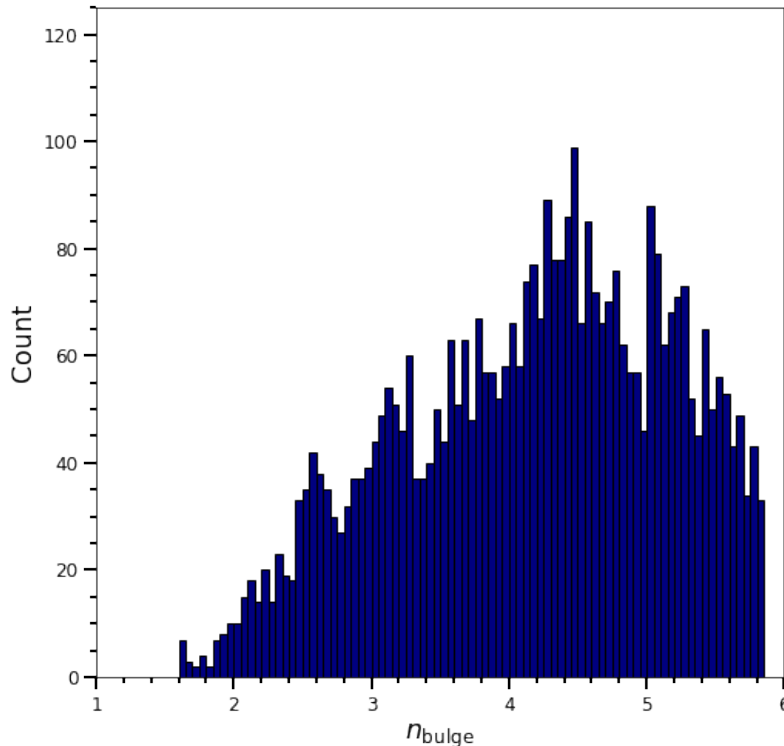
Figure 2.2: Sérsic indices of 4000 randomly sampled galaxy bulges, computed using the PDF that was constructed based on the results in Kennedy et al. (2016) (see their Figure 6). Note that a large sample of galaxies was chosen here purely for illustration purposes - in practice we sample the same number of n_{bulge} as the number of member galaxies in the cluster.

As mentioned in Section 1.1.2, simulations struggle to account for the hierarchical growth of the BCG with the cluster, so their models tend to be unrealistic. Therefore, we removed the lightcone's bulge+disk model of the BCG (retaining the total flux and centroid) and replaced it with a single component Sérsic profile. This profile has the same total flux as the lightcone BCG, but a half-light radius and Sérsic index adapted from the work of Kluge et al. (2020), who fit a composite BCG+ICL model to observational data. The median values of their Sérsic indices (n) and half-light radii (r_e) for the decomposed BCG+ICL model are given in Table 2.1 (provided by M. Kluge in private communication). Denoting the half-light radii from Table 2.1 as $r_{e,0}$, the half-light radius of the BCG or ICL in a cluster of stellar mass $M_\star$ is scaled as

$$r_e = \left(\frac{0.83 \log \frac{M_\star}{M_\odot} - 8.55}{1.74} \right) \log r_{e,0}. \tag{2.1}$$

Equation 2.1 is formulated based on the data in Figure 2.3.

	n	r_e [kpc]
BCG	4.58	22.61
ICL	0.76	189.5

Table 2.1: Sérsic index (n) and half-light radius (r_e) of the decomposed BCG+ICL model from Kluge et al. (2020)
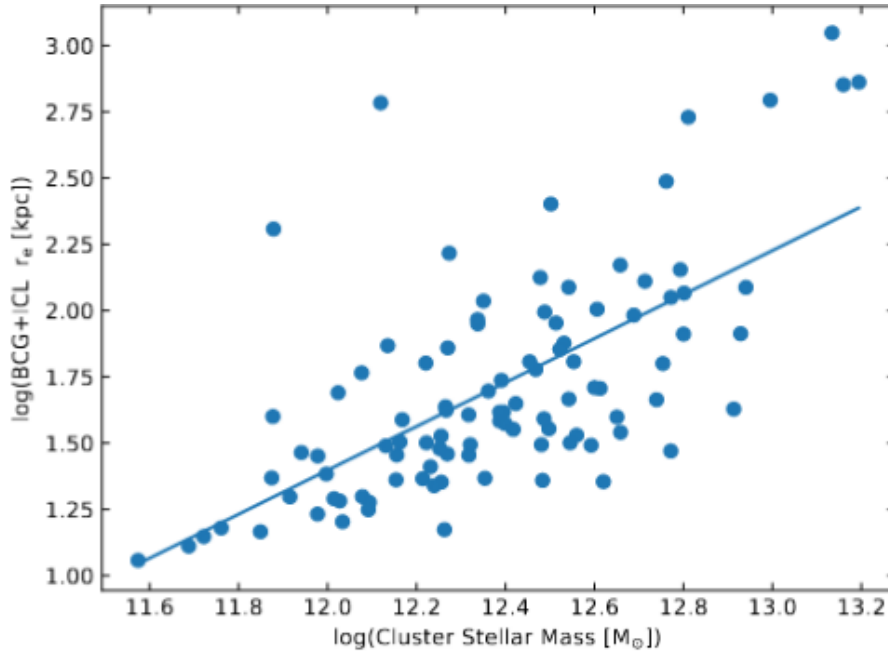
Figure 2.3: Half-light radius of the combined BCG+ICL model, fit to observed data, versus total cluster mass (based on the work of Kluge et al., 2020, provided via private communication).

We estimated the position angle and ellipticity of the BCG from a principle component analysis of the cluster, by using each cluster galaxy's position relative to the centroid of the BCG (a mathematical description of principal component analysis in relation to the ICL shape will be provided in Chapter 3). This is because the BCG+ICL tends to have a similar shape to the cluster (e.g. see Kluge, 2019)

We modelled the ICL as a single-component Sérsic profile that was initially concentric to the BCG with the same position angle and ellipticity. The Sérsic index and half-light radius given to the ICL profile were assumed using the same methodology as for the BCG. The flux of the ICL profile was taken arbitrarily as a specified fraction of the total cluster flux (considering contributions from cluster galaxies and the ICL), within the typically observed limits (see Section 1.1.1).

In order to produce an image of the cluster and its ICL from the analytical profiles, we used GalSim (Rowe et al., 2015). Fluxes were converted from physical units to electrons using the predicted zeropoint of *Euclid*'s VIS instrument (25.5mag). Positions

on the sky and physical size units from the lightcone were converted to pixels using the VIS instrument's pixel scale (a simple, linear mapping). The size of the cluster image was chosen to encompass all the cluster galaxies, with an additional margin of an arcminute so that no galaxies sat on the edge of the image. Each profile was convolved with a model for *Euclid*'s VIS instrument's point-spread function (PSF; see Figure 2.4), and then had Poisson noise added to it.
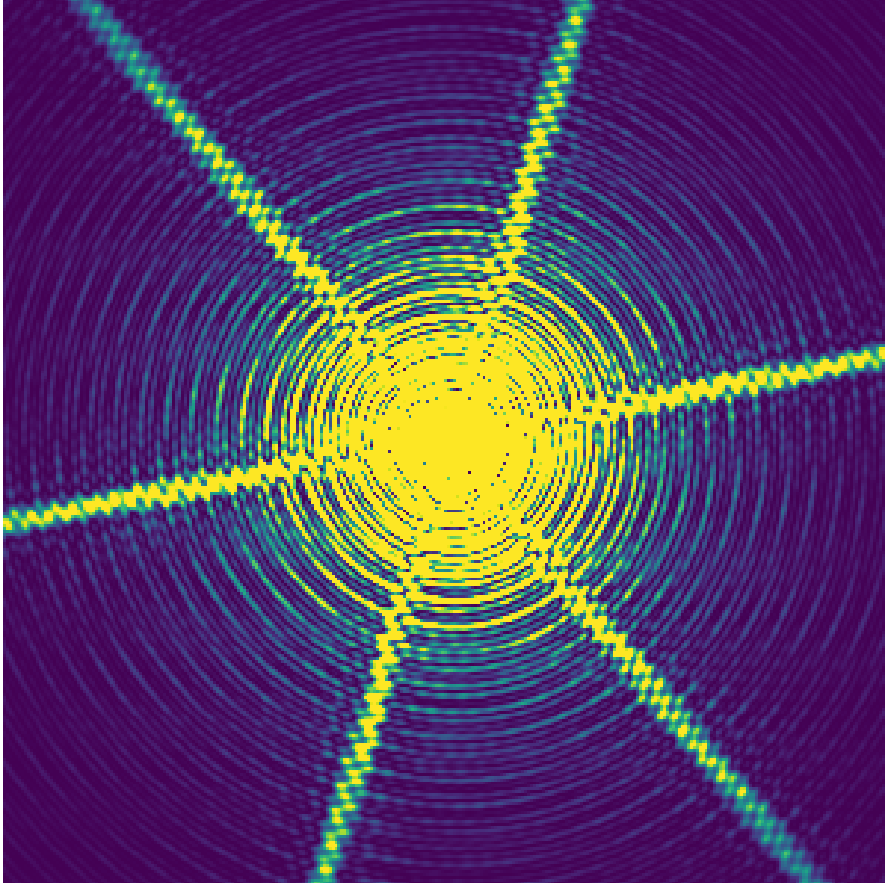
Figure 2.4: The PSF model for *Euclid*-VIS camera's PSF. This was convolved with each galaxy profile.

A total of 18 cluster images were simulated (including a red-herring image with no ICL), using the same cluster each time from the Millennium MAMBO lightcone, and separately added to the same region of the original image simulated by *Euclid*. Within these images, we varied the following ICL parameters:

1. **Total flux and half-light radius:** For these, we varied the ICL flux while adjusting the half-light radius to maintain a constant central surface brightness. 5 images were created, with ICL flux ranging from 2% to 50% of the total cluster flux.

2. **Total flux:** This time, central flux is not constant as half-light radius is fixed (using the original value). 5 images were created in the same manner as the previous example - note that this actually produced 4 new images, due to one of the clusters being the same as the standard in the previous category.

3. **Ellipticity:** Keeping the flux of the ICL fixed at 20% of the total cluster flux, the ellipticity was varied across 5 images, from 0 to 0.5.

4. **ICL centroid:** Again, the flux of the ICL is fixed at 20%, while its centroid is varied across 3 images, from 10kpc offset to the BCG to 50kpc offset to the BCG.

Figure 2.5 shows 4 example cluster images, with varied ICL parameters, before they were added onto the *Euclid* mosaic image.
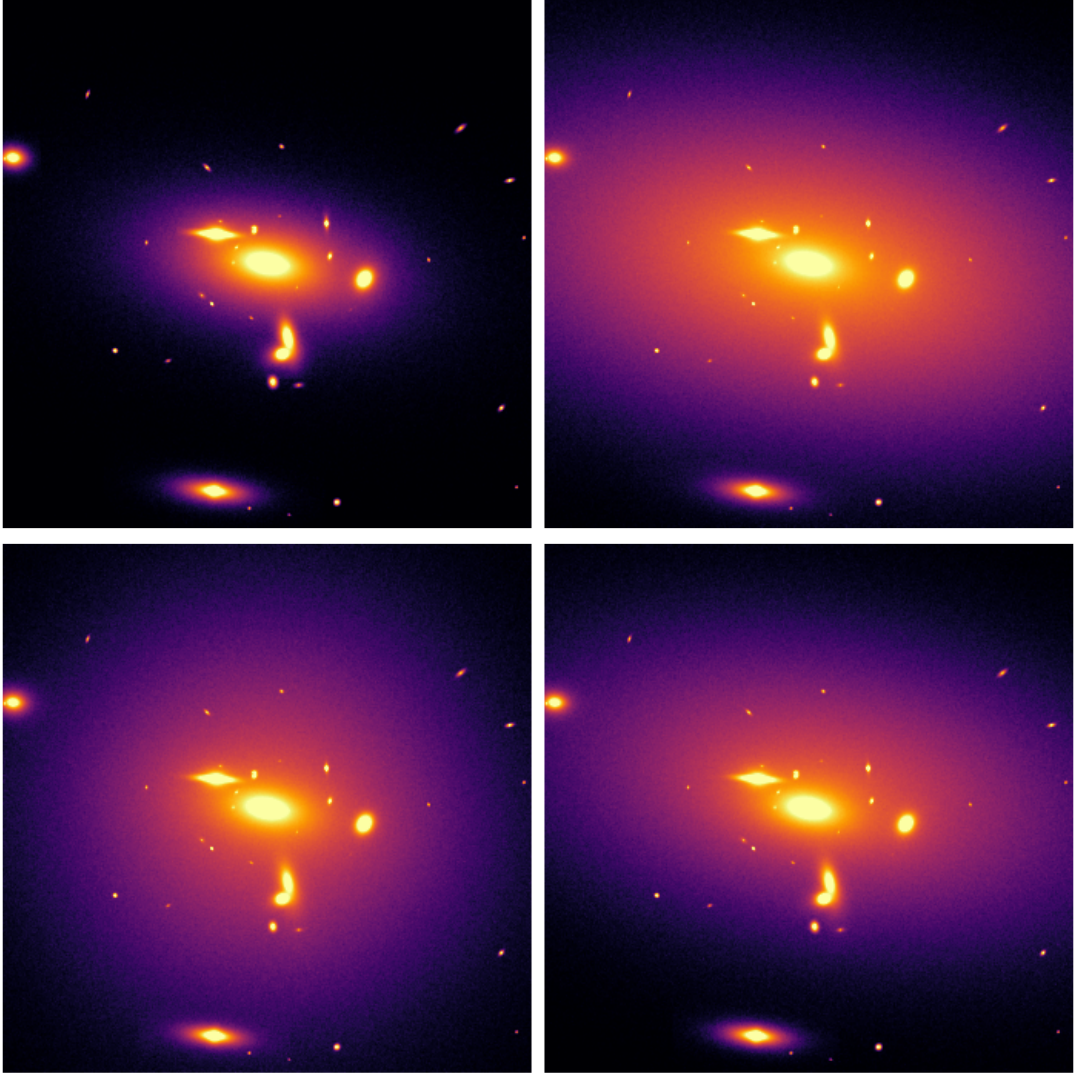
Figure 2.5: Comparing images of clusters with different ICL parameters, before they were added onto the *Euclid* mosaic image. These show: (*top left*) an ICL with a flux equating to 2% of the total cluster light in the constant central surface brightness run; (*top right*) an ICL with a flux equating to 36% of the total cluster light in the varying central surface brightness run; (*bottom left*) an ICL with zero ellipticity in the varying ellipticity run; (*bottom right*) an ICL with an offset of 50kpc from the BCG centroid. Note that the surface brightness limits were chosen here so that the ICL is clearly visible, and each image is zoomed in to 260″ on a side, with the BCG at the centre.

The resulting images were distributed amongst our collaborators in the ICL science working group within *Euclid*, so that they could test their ICL detection algorithms. Figure 2.6 shows a region of Figure 2.1 before and after one of the cluster images was added.
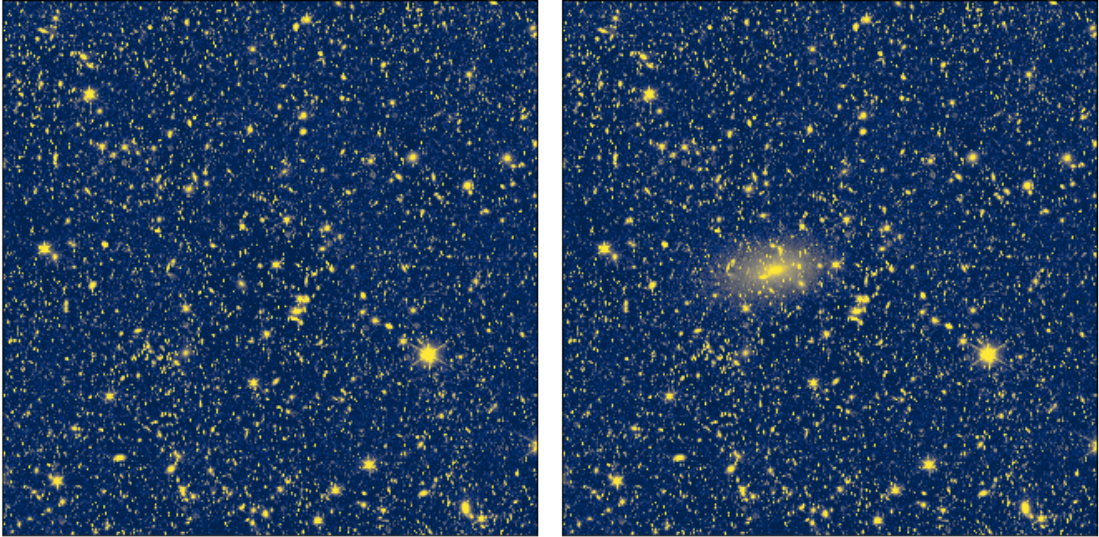
Figure 2.6: Region of Figure 2.1 before (left) and after (right) one of the cluster images was added. This particular cluster is at $z = 0.2$ and has an ICL component with: an ICL fraction of 50%, a shared centroid with the BCG, and an ellipticity and position angle taken from a principle component analysis of the cluster. These images are both $0.30°$ on a side.

2.3 Euclid's harsh background subtraction

One of our collaborators managed to fit the ICL in our simulated images with a two component Sérsic model, but noticed an unusual feature: the data repeatedly dipped below the expected model at a certain radius (see Figure 2.7). After applying surface brightness cuts to Figure 2.1, we realised that the background was uneven; this was due to being overly subtracted in particular regions (see Figure 2.8). The region that we added our cluster onto had contained one of these regions, and this is where we were seeing dips in the data compared with the model.

This is concerning because the ICL is extremely faint - having a harsh background subtraction will potentially obliterate the ICL signal. *Euclid*'s pipeline performs two background subtractions: the first subtraction is done via `NoiseChisel` (Akhlaghi & Ichikawa, 2015; Akhlaghi, 2019), which is optimised for the detection of diffuse, extended bodies that may get buried in noise. The second subtraction is done via `SExtractor` (Bertin & Arnouts, 1996). The operational procedure of `SExtractor`'s background subtraction is outlined in Section 1.2.1, and it is heavily influenced by bright pixels (such as those containing stars). Therefore, it is our suspicion that this part of the pipeline was causing problems in the overall background subtraction.
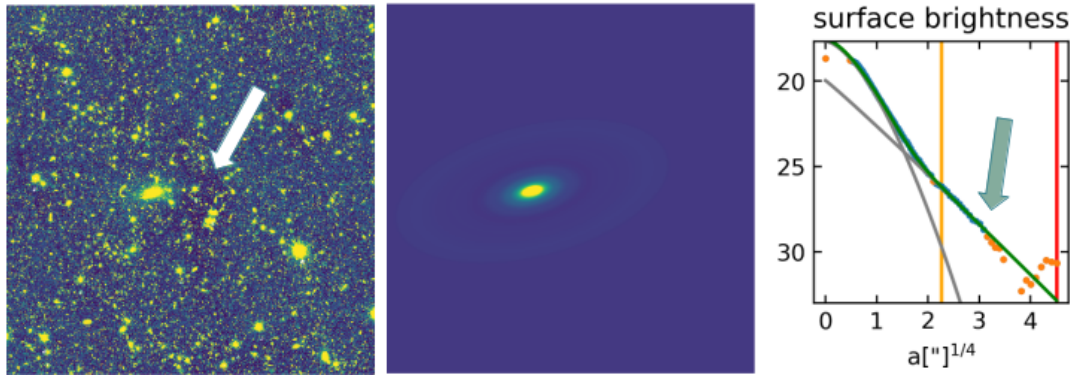
Figure 2.7: One of the radial profiles that a collaborator produced from our simulated images, described in Section 2.2. The left panel shows the full cluster + *Euclid* mosaic image, the middle panel shows the ICL profile obtained by fitting with a double Sérsic profile, and the right panel shows the surface brightness (in mag arcsec^{-2}) as a function of semi-major radius. The grey curves in the right panel are the individual components of the double Sérsic fit to the data, with the combined profile shown as the green curve. The data (orange points) match what is expected from the combined Sérsic profile until $a^{\frac{1}{4}} \sim 3 - 4 \text{arcsec}^{\frac{1}{4}}$ - this region corresponds to the region in the left panel pointed out by the arrow, which has a visible dearth in flux. Plots provided by Matthias Kluge.

2.4 Summary and Future Work

A procedure for simulating realistic Cluster+ICL images has been outlined in this chapter. This work is useful in preparing surveys for studying the ICL and testing the performance of ICL detection algorithms. The cluster images were constructed using data from the Millennium MAMBO lightcone (Springel et al., 2005), with the ICL parameters being derived from its cluster properties (though these were varied to create multiple slightly differing images). The Cluster+ICL images were added onto a *Euclid*-VIS simulated mosaic image (generated by *Euclid*'s simulations group), which had already been processed via the data reduction pipeline.

It was found that *Euclid*'s background subtraction algorithm is too harsh for ICL studies, and will likely diminish a significant amount of the ICL signal in images. A postdoctoral fellow at the University of Nottingham (C. Bellhouse) has followed on from the work set out in this chapter and added cluster images onto unprocessed, raw exposures that *Euclid* simulates, and passed them through the reduction pipeline. This has revealed that, just as expected, a significant loss in the ICL signal is seen when using *Euclid*'s standard reduction pipeline, as shown in Figure 2.9. C. Bellhouse is also using the method of simulating images outlined in this chapter to quantify the detectability of the ICL as a function of its cluster redshift and mass, and to test the performance of different ICL measurement methods - I will be a co-author on the resulting paper for this work. It is advisable that, should ICL studies be conducted using *Euclid* images, an alternative background subtraction should be applied to the raw, unprocessed data that
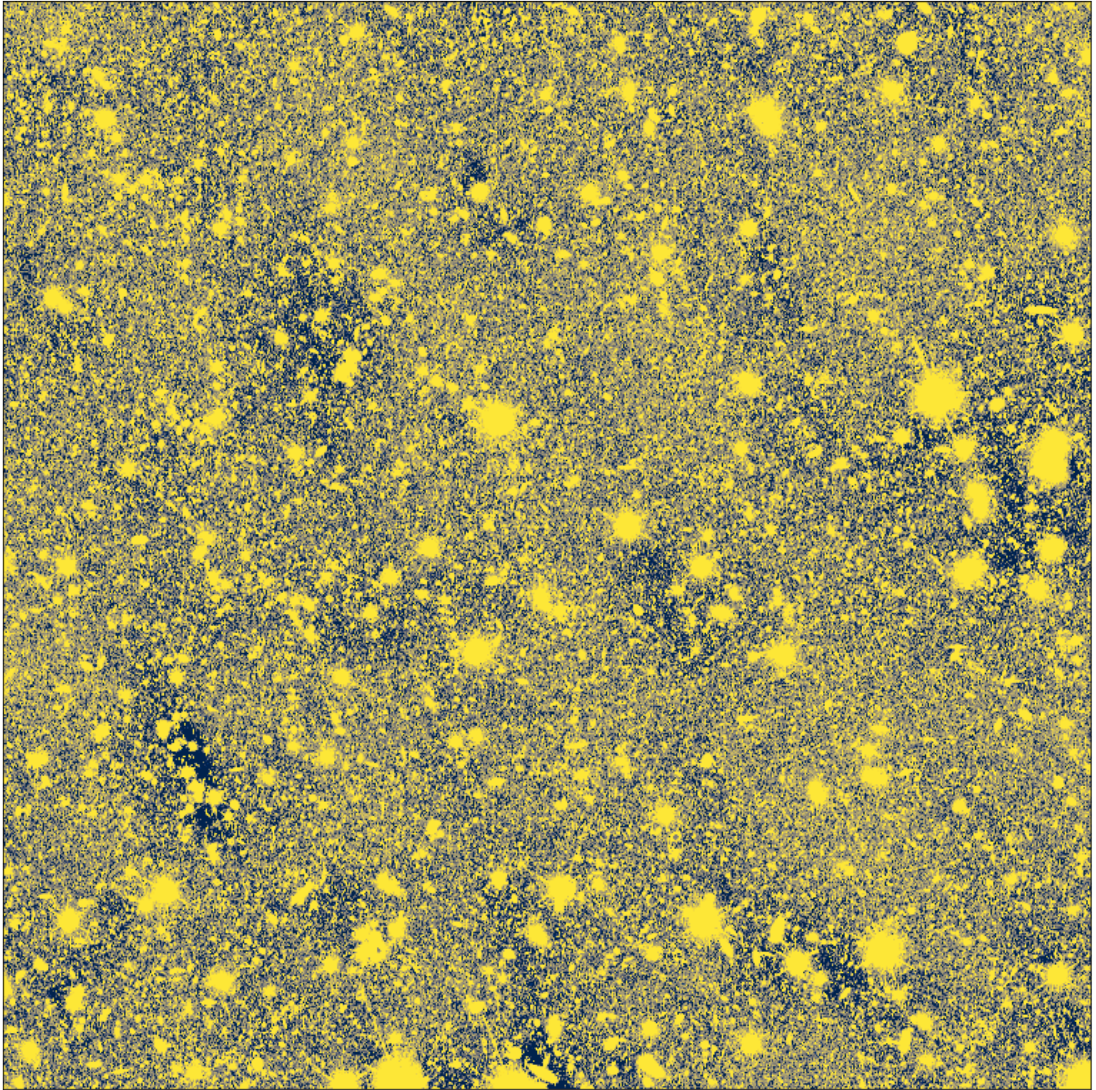
Figure 2.8: Same image as in Fig. 2.1, but with surface brightness cuts that emphasise the background. The background subtraction pipeline is producing a patchy image, consisting of many overly subtracted (dark) regions.

is suitable for this kind of science, instead of using data processed by *Euclid*'s standard pipeline. The galaxy evolution and ICL groups of *Euclid* are currently working on this.
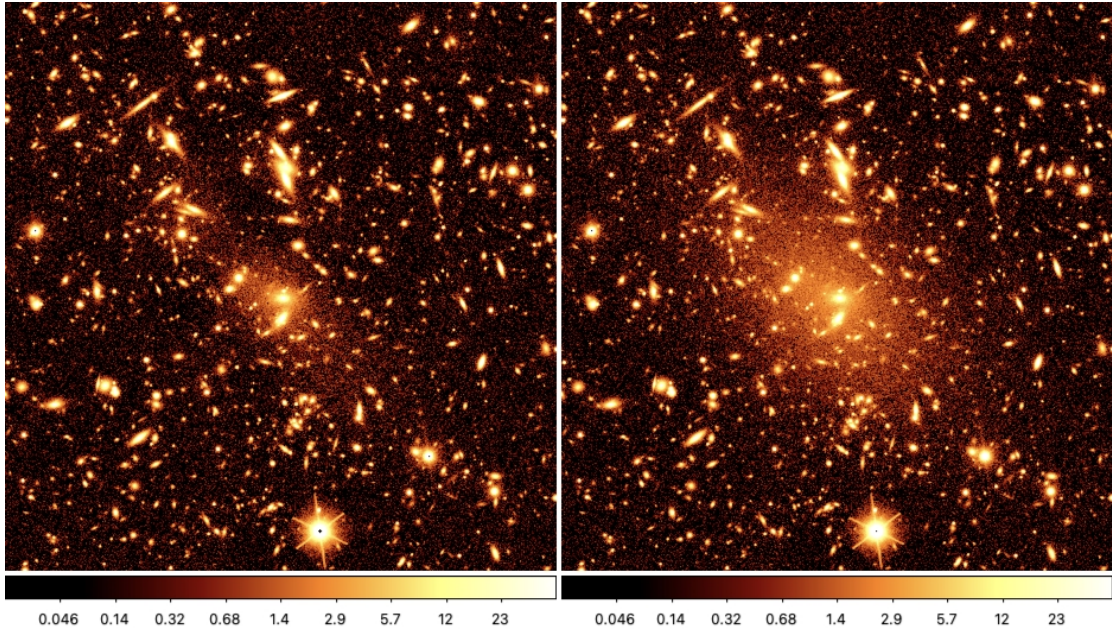
Figure 2.9: (Right panel) A cluster image, simulated using the methodology outlined in Section 2.2, that has been added onto a raw, unprocessed field exposure simulated by *Euclid*, and (left panel) the same image after being processed by *Euclid*'s reduction pipeline. Both images here are 240″ on a side and the colorbar shows the flux values, in counts, calculated using *Euclid*'s VIS instrument zeropoint. This figure, provided by C. Bellhouse (University of Nottingham), explicitly shows a significant loss in the ICL signal through use of the reduction pipeline, and highlights the need for an alternative for future ICL studies.

Chapter 3

Measuring the ICL in HSC Clusters using an Automated SB Threshold Method

The contents of this Chapter represent the work I did as part of my final project at the University of Nottingham. After some further analysis (described in Section 3.7.3), this work will form the basis of a journal paper.

3.1 Overview

Our primary goals here were: to implement an automated version of the traditional approach to measuring ICL, demonstrate it on a real dataset and study correlations between ICL and cluster properties. This work was inspired by the work of Furnell et al. (2021), who applied a combination of masking and surface brightness thresholding to a sample of X-ray selected clusters (see Section 3.3.1), cross-matched with the HSC Subaru Strategic Program (SSP) deep layer footprint, to analyse the ICL as a function of cosmic time. Although Furnell et al. (2021) had already measured the ICL in these clusters, we decided it was appropriate to try to reproduce their results for the following reasons:

1. **Access to Public Data Release 3 (PDR3):** The original study made use of HSC-SSP PDR1 but we now have access to the most up-to-date data from PDR3. This marks a significant improvement because the global sky background subtraction has been improved in a way that complements studies of extended objects. It was noted in PDR1 (section 5.8.5 of Aihara et al., 2018b) that the background sub-

traction was performed on a CCD-by-CCD basis, using pixel grids that had their sizes chosen to preserve small-scale features, at the cost of degrading extended features (see Bosch et al., 2018, for the full description of the HSC pipeline at PDR1). This meant that the wings of both the ICL and extended cluster galaxies were oversubtracted, leading to a reduced ICL signal and dearths of flux around cluster galaxies ('divots'). To account for this, Furnell et al. (2021) proposed a post-processing fix in divot-corrections: interpolating galaxy profiles to try and estimate the over-subtracted flux.

A solution to the global background subtraction of the HSC pipeline was implemented in PDR2, which modelled the sky across the entire field-of-view, as opposed to modelling the sky for each individual CCD (alleviating biases due to bright, extended objects and preventing discontinuities between CCDs in the sky model Aihara et al., 2019). Further improvements were made to the sky model in PDR3, to remove biases in regions near dead CCDs or the field edge (see Figure 7 of Aihara et al., 2022). Coadd images with the global sky model subtracted from them are available to users in an intermediary state before they undergo local sky-subtraction (necessary for source detection and measurements), which preserves the wings of objects that may be lost as a result of harsh deblending. Therefore, we do not require divot-corrections when using PDR3 data, giving a more accurate representation of the ICL.

As well as the improved sky background subtraction, the star masking in HSC-SSP's recent data releases has improved. At PDR1, star masks were created using the NOMAD reference catalog (Zacharias et al., 2004). Furnell et al. (2021) noted that this catalog is incomplete, and so opted to create their own masks using the catalog from GAIA DR2 (Gaia Collaboration et al., 2018). In HSC-SSP PDR2 and PDR3, star masks were created based on GAIA DR2 data, meaning the star masking was much more complete than before. It was also noted in PDR3 that improvements were made to the size of star masks, as these were now dependent on the filter (see Section 4.2 in Aihara et al., 2022). Therefore, using PDR3 data means we do not require reference catalogs of stars for masking, as these are contained in the HSC mask images.

2. **We outline an alternative method of determining the total cluster flux, with a statistical background correction:** In order to estimate how much of the total light of a cluster is ICL, it is necessary to estimate how much flux is due to cluster galaxies. It is not clear in Furnell et al. (2021) exactly how they obtain their cluster galaxy flux estimate, and there is no information on what these values actually are (we assume they they just summed up all the light within R_{500} after doing some, unspecified, masking). Therefore, we provide a method of assigning membership

to galaxies using spectroscopic data, where available, or photometric data with a statistical background subtraction.

3. **Our method is automated:** Some of the masking is done by eye in Furnell et al. (2021), which becomes time-consuming with large samples of clusters. We avoid this by ensuring that our masking is done on an automated basis, provided that the relevant input parameters are known. This also removes any human biases that may propagate in the final results.

With our analysis, we explore some of the ideas discussed in Section 1.1.1, specifically how the ICL evolves with cosmic time and cluster mass/richness. We then apply the method to a larger sample of clusters.

3.2 The HSC-SSP Survey

3.2.1 Survey Description

The HSC instrument (Miyazaki et al., 2018) is composed of 104 science CCDs (equating to 870 Megapixels) that offer a resolution of 0.168"/pix, and it covers a field of view of 1.5deg in diameter. The camera is mounted on the prime focus of the 8.2m Subaru Telescope, located at the summit of the inactive volcano Mauna Kea in Hawaii. This site offers excellent seeing conditions, with a median of 0.6" in the *i*-band; combining this with the large aperture and wide field of view makes HSC a particularly suitable instrument for carrying out ICL studies.

The HSC-SSP (Aihara et al., 2018a,b, 2019, 2022) resembles one of the deepest ground-based, publicly available, optical surveys, with a 5σ limiting depth of $i \sim 26.8$mag. Since its first-light in March 2014, the HSC-SSP has been scheduled to observe over a total of 330 nights, with data being collected in three separate layers across multiple passbands (*grizy* plus 4 narrow-band filters): 'Wide' (1200deg^2), 'Deep' (27deg^2) and 'UltraDeep' (3.5deg^2). In this work we use *i*-band, Deep-layer data, which is split across 4 fields: XMM-LSS, E-COSMOS, ELAIS-N1[1], DEEP2-F3.

3.2.2 HSC-SSP PDR3 Data Reduction

Data from the third release of the HSC-SSP survey is processed via the eighth version of HSC's pipeline tool, `hscPipe` (full implementation outlined in Bosch et al., 2018,

---

[1]This is the only field that is not covered by the Wide-layer of the HSC-SSP survey.
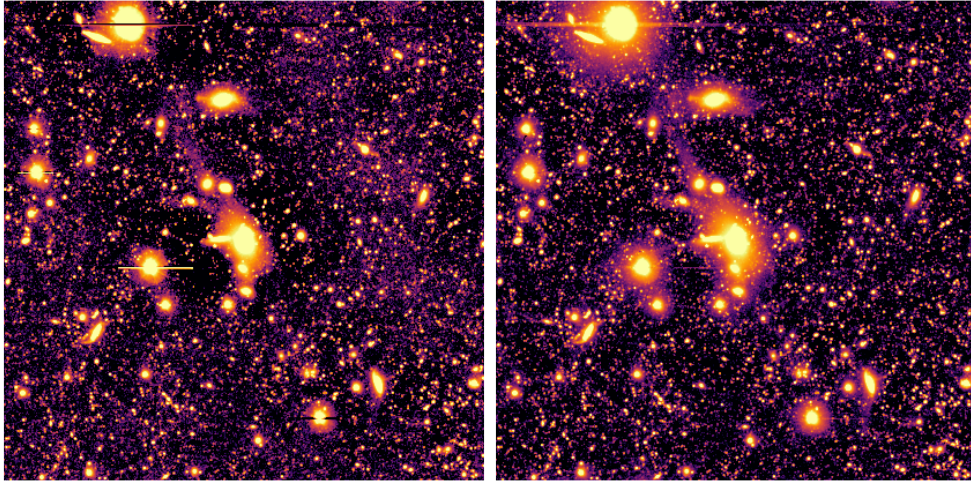
Figure 3.1: Galaxy cluster XMMXCS J022456.1-050802.0 (see Table 3.1) imaged using PDR1 data (left) vs PDR3 data (right). Both images are 370″ on each side. Note that the image on the left has been fully processed, while the image on the right is at an intermediary stage before local sky-subtraction, a feature that only became available at PDR3. It is clear that more ICL signal is recovered in the most recent data release, marking a significant improvement for studies of the ICL.

although only at version 4). This software is open source and licensed for public use under version 3 of the GNU public license. As already mentioned, the pipeline used to process PDR3 data marks a significant improvement from the one used to process PDR1 data (`hscPipe 4`). The biggest concern for ICL studies was that `hscPipe 4` would oversubtract the flux around bright, extended objects in the background subtraction, as was noted in Aihara et al. (2018b) and also shown in Huang et al. (2018). Figure 3.1 shows a comparison of the galaxy cluster XMMXCS J022456.1-050802.0 (the first cluster in the sample used by Furnell et al., 2021) from PDR1 and from PDR3. The ICL signal is reduced and the flux around bright sources is visibly over-subtracted in the PDR1 version.

The sky contribution was estimated and subtracted individually for each CCD in the fourth version of `hscPipe`, using a sixth-order variance-weighted Chebyshev polynomial, fit to the 3σ-clipped average values in 128×128 bins of pixels across the whole detector (typically ~256×256 pixels in size, known as 'superpixels'), ignoring any pixels that belong to sources. Due to the relatively small size of the superpixels in comparison to the size of a CCD (2048×4176 pixels), the sky model was heavily influenced by pixels in regions containing bright, extended objects. Furthermore, the sky model exhibited discontinuities where images spanned across multiple CCDs.

In `hscPipe 8`, used to process PDR3 data, the global sky frame is estimated and subtracted as follows: (1) a clipped mean is calculated for superpixels of size 8k × 8k pixels, not including pixels that belong to sources; (2) the superpixels are then fit with 2D polynomials to construct a sky background model; (3) the background model is subtracted from the science image; (4) a scaled-sky frame is constructed by separately stacking many (typically several tens) science exposures with large dithers and this is also subtracted from the image – this removes static features that have a smaller scale than the initial sky background sky model. An additional step is taken to remove small-scale fluctuations at very low flux levels: superpixels of 256×256 pixels in size are used to estimate the background, which is then subtracted; sources are then carefully detected, characterised and masked; the sky is put back in and the process is repeated three times. Doing this retains the wings of bright sources while removing small-scale flux variations.

The global sky subtraction represents the end of the first stage of the data reduction process (CCD processing). Prior to this, basic data reduction is performed (flat-fielding, bias and dark frames), brighter-fatter corrections due to source intensity dependence on the measured PSF are made, and cross-talk and CCD non-linearity corrections are carried out. Also at this stage, bad and saturated pixels are identified and these are included in mask images, which can be obtained in parallel with science and variance images, using HSC's DAS cutout tool. After CCD processing, there are two more stages of data reduction to produce the final pipeline output images: *Joint Calibration* to refine photometric and astrometric calibrations after CCD processing, and *Image Coaddition*. The images used in this work are in an intermediate state, just after global sky subtraction and subsequent coaddition, but before the final aggressive background subtraction (this final step gives images that the photometry measurements are performed on). Therefore, extended objects in these images, which would usually be affected by the aggressive background subtraction, are preserved, enabling more accurate characterisation of the ICL.

Note that in this Chapter, the images analysed are obtained in the form provided by the HSC archive – I do not run any parts of the pipeline on the unprocessed images myself for this work.

3.3 Data

We use galaxy clusters identified in two datasets. The first, which was also used in Furnell et al. (2021), is a set of X-ray clusters from the XMM Cluster Survey (XCS; Romer et al., 2001), while the second is an optically-selected cluster catalog from the HSC-SSP,

constructed using the CAMIRA cluster finding algorithm (Oguri, 2014; Oguri et al., 2018). Details of the XCS (also given in Furnell et al., 2021) and the CAMIRA cluster finding algorithm are given below.

3.3.1 The XMM Cluster Survey

The XCS is a serendipitous X-ray survey, searching for galaxy clusters using archival data from the XMM-Newton space telescope. X-ray surveys of clusters have the upper hand over their optical counterparts as they are less biased with regards to the nature of their detections: X-ray measurements are far less susceptible to contamination by multiple structures along the projected line-of-sight, as they relate to the intrinsic properties of galaxy clusters, e.g. intracluster medium (ICM) temperatures and spatial distributions, rather than relying on overdensities from optical catalogs. This makes the XCS a desirable survey for constructing a sample of clusters.

In order to confirm detections as true galaxy clusters, the XCS implements two rounds of scrutiny. The first categorises X-ray detections as point-like and extended-like, the latter resembling a possible cluster, using XMM's Automated Pipeline Algorithm (XAPA; see Mehrtens et al., 2012). However, this pipeline can provide false rejections/confirmations if: a cluster has multiple X-ray peaks as opposed to a single smooth profile, leading to rejection; bright, non-cluster sources contain 'bleed trails', which are mistaken as extended emissions, or Active Galactic Nuclei (AGN), misclassifying them as a cluster. Therefore, a second round of examination is performed by members of the XCS collaboration, who validate these detections by-eye, using a regime that ranks objects from definite clusters to definite contaminants (known as the 'XCS Zoo').

The most recent XCS data release (DR2; Manolopoulou et al., in preparation) is composed of nearly 1300 optically confirmed galaxy clusters, with over 200 of these being completely new to literature. These clusters are cross-matched for spectroscopy with the SDSS DR13 (Albareti et al., 2017), DEEP2 (Newman et al., 2013) and VIPERS DR2 (Guzzo et al., 2014) surveys. Their spectroscopic redshifts are computed by, first, using a biweight location estimator (as in Beers et al., 1990) on the spectroscopic redshifts of all galaxies that fall within 1.5 arcminutes of the XAPA-computed centroid, with varying spectroscopic completeness, followed by re-calculation after applying a velocity dispersion cut of $\Delta v \pm 3000 \mathrm{kms}^{-1}$ about the initial redshift, within a physical radius of 1.5Mpc from the XAPA centroid.

3.3.2 The CAMIRA Catalog

The CAMIRA cluster-finding algorithm (Oguri, 2014) operates based on the fact that all galaxy clusters are observed to have a well-defined, highly regular population of elliptical and lenticular galaxies. This 'red sequence' of galaxies exhibits a tight correlation between colour and luminosity (the colour-magnitude relation; Visvanathan & Sandage, 1977), which has been known for quite some time (Baum, 1959). The algorithm first fits all photometric galaxies with the stellar population synthesis (SPS) model from Bruzual & Charlot (2003), and then it estimates the likelihood of them being on the red sequence as a function of redshift. Each galaxy is assigned a 'number parameter' as a function of redshift, based on the likelihood of it being a red sequence galaxy. Using these number parameters, three-dimensional richness maps are constructed and cluster candidates are identified based on peaks in cluster richness. Note that the richness parameter here is defined as the number of red sequence cluster members with masses $M \gtrsim 10^{10.2} M_\odot$ within a circular aperture of radius $R \simeq 1h^{-1}\mathrm{Mpc}$.

The CAMIRA algorithm was first used in Oguri (2014), where it was applied to imaging data from SDSS DR8 (Aihara et al., 2011), covering roughly $11960\mathrm{deg}^2$ on the sky. A catalog of 71743 galaxy clusters was constructed in the redshift range $0.1 \leq z \leq 0.6$. The cluster redshift estimates were compared with spectroscopic redshifts from the following external cluster catalogs: XCS (Mehrtens et al., 2012), the Meta-Catalog of X-ray detected Clusters (MCXC; Piffaretti et al., 2011), ACCEPT (Cavagnolo et al., 2009) and the Sloan Giant Arcs Survey (SGAS; note that only 24 clusters from the works of Bayliss et al., 2011; Oguri et al., 2012; Bayliss et al., 2014, were used). This comparison revealed that the photometric estimates derived from CAMIRA were accurate with low bias and scatter. The author also found a strong correlation between the CAMIRA-estimated cluster richness and X-ray luminosities and temperatures, taken from the aforementioned cluster catalogs.

More recently, the CAMIRA algorithm has been applied to HSC-SSP Wide PDR3 data (Oguri et al., 2018, note that this paper refers to PDR1 data, but the catalog itself has since been updated to include PDR3 data). This initially led to the detection of 1921 high purity, high completeness galaxy clusters in the redshift range $0.1 \leq z \leq 1.1$, covering an area of $\sim 232\mathrm{deg}^2$ – the catalog has since grown to include 7939 clusters. As before, the authors found that the sample was accurate with low bias and scatter, and the richness is concordant with the cluster X-ray properties. In this work, we require deep HSC data to analyse the ICL with as much accuracy as possible. Therefore, we

use the most recent Deep-layer catalog from Oguri et al. (2018), consisting of 248 HSC galaxy clusters[2].

3.4 Sample Selection

3.4.1 XCS Sample

For the XCS sample, we use the same data as in Furnell et al. (2021). A summary of how the sample was obtained is given below:

- The XCS-DR2 North (Manolopoulou et al., in preparation) catalogue of clusters was cross-matched with the entire HSC-SSP PDR1 footprint (Wide, Deep and UltraDeep layers), producing a match for 202 clusters.

- The clusters and their BCGs were required to have spectroscopic redshifts, further reducing the sample to 79 clusters.

- The cluster redshift and BCG redshift were not allowed to deviate from each other in velocity space by more than $\Delta v = \pm 5000 \text{kms}^{-1}$. This criterion reduced the sample by 8, leaving 71 clusters.

- The clusters had to have X-ray parameters from XAPA - 53 satisfied this requirement. Of these, 29 resided in the HSC-SSP PDR1 Deep footprint.

- 1.5Mpc^2 cutouts of the 29 Deep-layer clusters were downloaded using HSC's DAS cutout tool. This led to the rejection of 11 more clusters due to them having too much bright foreground object contamination or being on the edge of the survey (7 clusters), or being deemed poor candidates by the authors (4 clusters).

The 18 XCS-HSC clusters are described in Table 3.1.

---

[2]Available at:
`https://github.com/oguri/cluster_catalogs/blob/main/hsc_s20a_camira/camira_s20a_dud.tbl`

Table 3.1: The 18 XCS-HSC clusters used in this work, adapted from Table 2 of Furnell et al. (2021) – note that only the parameters relevant to this work have been kept from the original table.

XCS ID	α_{2000}	δ_{2000}	z	R_{500} [Mpc]	M_{500} [$10^{14}M_{\odot}$]
XMMXCS J022456.1-050802.0	36.234	-5.134	0.084	0.331	0.112
XMMXCS J161039.2+540604.0	242.664	54.101	0.339	0.483	0.457
XMMXCS J233137.8+000735.0	352.908	0.126	0.224	0.537	0.553
XMMXCS J232923.6-004854.7	352.348	-0.815	0.300	0.746	1.611
XMMXCS J161134.1+541640.5	242.892	54.278	0.337	0.729	1.567
XMMXCS J095902.7+025544.9	149.761	2.929	0.349	0.765	1.836
XMMXCS J095901.2+024740.4	149.755	2.794	0.501	0.406	0.327
XMMXCS J100141.6+022538.8	150.424	2.427	0.124	0.509	0.424
XMMXCS J095737.1+023428.9	149.405	2.575	0.373	0.741	1.716
XMMXCS J022156.8-054521.9	35.487	-5.756	0.259	0.544	0.595
XMMXCS J022148.1-034608.0	35.45	-3.769	0.432	0.873	3.001
XMMXCS J022530.8-041421.1	36.378	-4.239	0.143	0.568	0.602
XMMXCS J100047.3+013927.8	150.197	1.658	0.221	0.73	1.382
XMMXCS J022726.5-043207.1	36.861	-4.535	0.308	0.716	1.438
XMMXCS J022524.8-044043.4	36.353	-4.679	0.264	0.626	0.917
XMMXCS J095951.2+014045.8	149.963	1.679	0.372	0.557	0.734
XMMXCS J022401.9-050528.4	36.008	-5.091	0.324	0.515	0.544
XMMXCS J095924.7+014614.1	149.853	1.77	0.124	0.472	0.339

3.4.2 CAMIRA Sample

The CAMIRA catalogue does not directly provide cluster mass or size information. Instead, the catalog provides richness values derived for each cluster, which can be used to estimate M_{200}. In applying CAMIRA to a mock galaxy catalog – constructed for testing purposes – Oguri et al. (2018) fit a power-law to the median values of M_{200} as a function of the respective CAMIRA-computed richness values (see their Figure 13). They found that

$$\langle \log(M|N) \rangle = a_M \log\left(\frac{N}{30}\right) + b_M, \tag{3.1}$$

where $\langle \log(M|N) \rangle$ is the median mass-richness relation, which we assume to be equivalent to $\log(M_{200})$, a_M and b_M are fitting parameters with best-fit values of 1.31 and 13.89 respectively, and N is the 'mask-corrected richness' (as defined in Oguri, 2014) computed by the CAMIRA algorithm. The authors noted a scatter of $\sigma_{\log M} = 0.19$ on this relation. We then calculate the concentration parameter, defined in Neto et al. (2007) as

$$c_{200} = 4.67(M_{200}/10^{14}h^{-1}M_{\odot})^{-0.11}, \tag{3.2}$$

and use this to calculate the value for R_{500}, assuming that the halo is relaxed and can be described by the Navarro-Frenk-White (NFW; Navarro et al., 1996, 1997) profile. With our estimates for R_{500}, we downloaded cutout images of all 248 S20a CAMIRA Deep-layer clusters using HSC's DAS cutout tool, with every image being $3R_{500}$ on each side.

The initial sample of galaxy clusters covered a redshift range of $0.1 < z < 1.2$ – we began by limiting the sample to $z < 0.8$, which gave 189 clusters. Further inspection of the images led us to conclude that those with a richness less than ~ 20 did not appear as obvious cluster candidates, centred on a BCG surrounded by satellite galaxies. This richness cut was also applied to the mock clusters that were used to fit the CAMIRA mass-richness relation, derived by Oguri et al. (2018) (Equation 3.1). After applying redshift and richness cuts, our sample reduced to 101 clusters.

A further 41 clusters were omitted due to poor data quality (e.g. edge of survey or too many artefacts), too much star masking (particularly candidates with star masks that overlap significantly with the BCG, see Section 3.5.1), too much excess flux from foreground objects/potentially merging clusters or candidates that we are not fully confident are truly clusters with ICL – this reduced the sample to 60. We then noticed that 6 of the CAMIRA clusters were included already in the sample used by Furnell et al. (2021), so we chose to eliminate these because we are more confident in the X-ray derived parameters. Therefore, our CAMIRA sample contained 54 clusters in total, given in Table 3.2. In Figure 3.2, we give the distribution of $\log \frac{M_{200}}{M_\odot}$ for our final cluster sample, which were calculated using Equation 3.1.

Table 3.2: The main parameters of the 54 CAMIRA-detected sample of clusters used in this work. R_{500} values are estimated using the methodology outlined in Section 3.4.2.

CAMIRA-HSC ID	α_{2000}	δ_{2000}	z	R_{500} [Mpc]	Richness, N
HSCJ021528-044041	33.868	-4.678	0.332	0.836	67.1
HSCJ021635-042812	34.145	-4.470	0.455	0.515	24.2
HSCJ021837-054025	34.655	-5.674	0.256	0.533	21.8
HSCJ021942-045231	34.923	-4.875	0.316	0.548	24.7
HSCJ022351-053640	35.960	-5.611	0.493	0.519	25.5
HSCJ022358-043505	35.992	-4.585	0.490	0.477	20.9
HSCJ022433-041419	36.139	-4.239	0.252	0.527	21.3
HSCJ022636-040410	36.649	-4.070	0.334	0.499	20.1
HSCJ022828-042608	37.116	-4.435	0.427	0.549	27.4
HSCJ022933-043948	37.388	-4.663	0.610	0.534	30.5
HSCJ023028-043349	37.616	-4.564	0.271	0.620	31.6
HSCJ095536+010310	148.898	1.053	0.451	0.585	32.5
HSCJ095606+023650	149.024	2.614	0.488	0.480	21.1
HSCJ095728+033956	149.366	3.665	0.169	0.628	29.7

Table 3.2 – continued from previous page

CAMIRA-HSC ID	α_{2000}	δ_{2000}	z	R_{500} [Mpc]	Richness, N
HSCJ095824+024916	149.600	2.821	0.341	0.519	22.1
HSCJ095918+033052	149.826	3.514	0.718	0.445	22.0
HSCJ100022+022328	150.091	2.391	0.218	0.693	39.1
HSCJ100252+031427	150.716	3.241	0.548	0.531	28.4
HSCJ100300+013152	150.750	1.531	0.695	0.482	26.0
HSCJ100452+025434	151.215	2.909	0.108	0.545	20.4
HSCJ100459+015442	151.246	1.912	0.209	0.553	22.9
HSCJ100532+023518	151.381	2.588	0.348	0.869	74.4
HSCJ160159+552418	240.496	55.405	0.406	0.609	34.3
HSCJ160434+551301	241.142	55.217	0.379	0.501	21.2
HSCJ160439+543137	241.164	54.527	0.257	0.989	93.1
HSCJ160508+545208	241.283	54.869	0.605	0.479	23.5
HSCJ160551+544727	241.461	54.791	0.261	0.614	30.6
HSCJ160600+545854	241.501	54.982	0.540	0.468	21.0
HSCJ160605+542841	241.520	54.478	0.778	0.525	34.4
HSCJ160633+535359	241.638	53.900	0.362	0.700	45.4
HSCJ160639+560806	241.663	56.135	0.789	0.497	30.5
HSCJ160903+534302	242.262	53.717	0.744	0.483	27.3
HSCJ161101+561748	242.752	56.297	0.296	0.608	30.9
HSCJ161112+553451	242.799	55.581	0.224	0.788	53.1
HSCJ161221+532107	243.087	53.352	0.174	0.578	24.6
HSCJ161225+555438	243.103	55.910	0.274	0.686	40.1
HSCJ161249+540837	243.206	54.144	0.161	0.607	27.3
HSCJ161317+560119	243.323	56.022	0.494	0.481	21.4
HSCJ161412+554132	243.550	55.692	0.254	0.527	21.2
HSCJ161415+544328	243.564	54.725	0.338	0.787	58.5
HSCJ161434+542551	243.643	54.431	0.233	0.646	33.6
HSCJ161634+553955	244.143	55.665	0.253	0.669	37.0
HSCJ161704+545025	244.268	54.840	0.429	0.486	20.6
HSCJ161826+542543	244.608	54.428	0.544	0.481	22.4
HSCJ161834+551751	244.642	55.297	0.260	0.664	36.7
HSCJ161915+551341	244.811	55.228	0.353	0.537	24.3
HSCJ161925+551436	244.853	55.243	0.672	0.538	32.8
HSCJ232209-012057	350.537	-1.349	0.352	0.578	28.8
HSCJ232540-001112	351.418	-0.187	0.571	0.464	21.2
HSCJ232732+005634	351.883	0.943	0.256	0.764	50.8
HSCJ233015-011940	352.564	-1.328	0.508	0.521	26.1
HSCJ233031+003810	352.629	0.636	0.260	0.581	26.9
HSCJ233128+003654	352.867	0.615	0.260	0.621	31.3
HSCJ233328-000122	353.366	-0.023	0.503	0.502	23.9
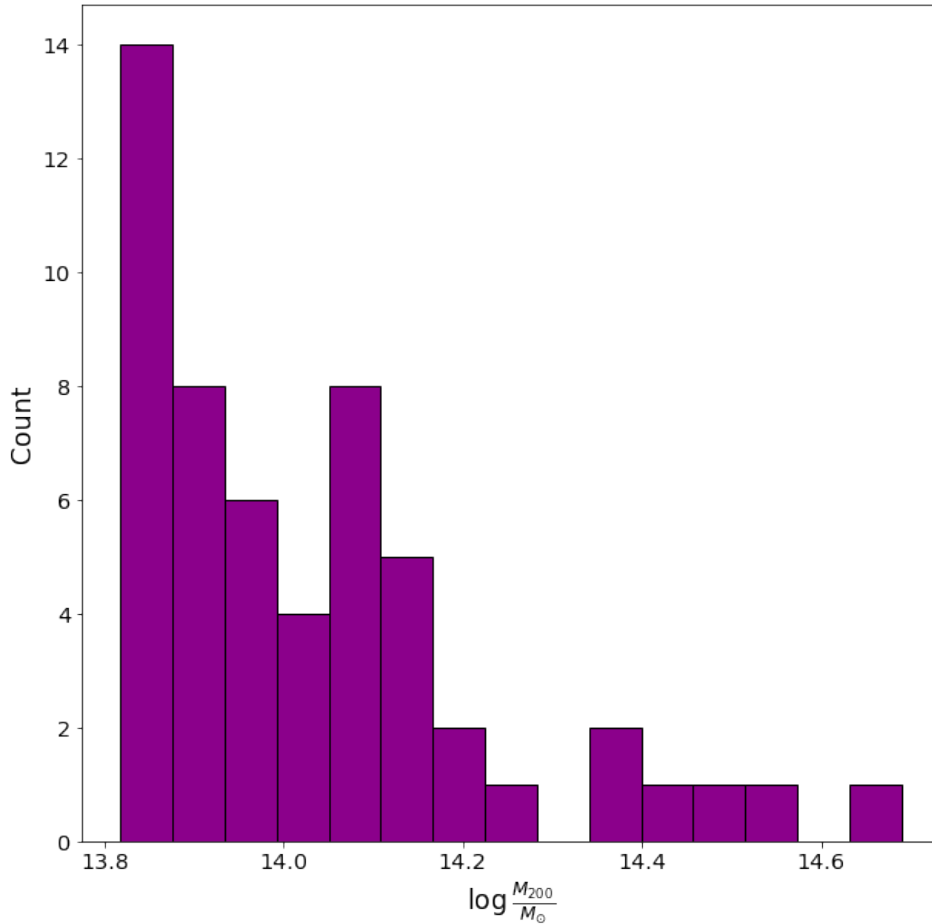
Figure 3.2: Distribution of the $\log \frac{M_{200}}{M_{\odot}}$ values of our final sample of 54 CAMIRA-detected clusters.

3.5 Method

3.5.1 Masking

We apply four mask layers to the HSC *i*-band science images, such that the remaining flux is that of the ICL with as little contamination from artefacts, stars and cluster/field galaxies as possible. The layers are outlined below.

1. **HSC Mask:** The first mask layer aims to identify regions in the image that have been affected by bad/saturated pixels and stars. Although this information is con-

tained within the mask image generated by the HSC pipeline, we only utilize the binary masks corresponding to bad/saturated pixels.

We do not use binary masks corresponding to stars from the HSC pipeline because many of these are larger than necessary, resulting in a potentially diminishing ICL signal. The purpose of these HSC star masks is to account for dip features, present after local sky subtraction, which exhibit areas of over-subtraction around stars. Therefore, the HSC pipeline automatically applies a mask of radius 0.011111° to all stars fainter than 10mag.

Because we use images in an intermediate stage before local sky subtraction and after global sky subtraction, we construct our own masks using the parameters in the HSC PDR3 bright object mask catalog[3], with the dip features removed. We also double the size of each star mask as the halo wings often remain visible. Clusters that have star masks which overlap with more than 50% of a 50kpc region surrounding the BCG are automatically discarded from the sample, as these mask too much of the highest signal regions of the ICL, making analysis inaccurate. Figure 3.3 shows the cluster XMMXCS J022456.1-050802.0 before and after the HSC mask is applied.
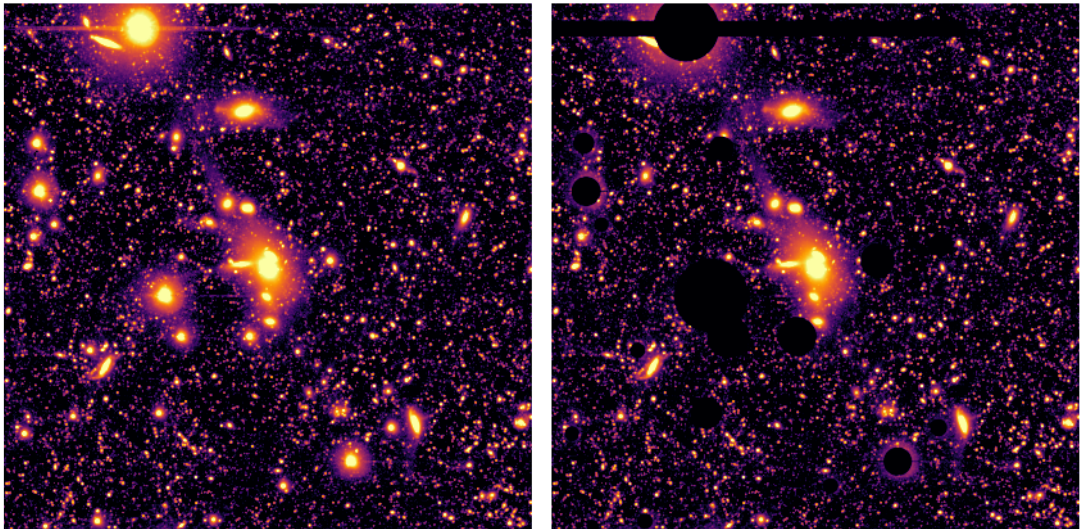
Figure 3.3: XMMXCS J022456.1-050802.0, from the sample in Table 3.1, before and after the HSC mask is applied. This constitutes the first mask layer, removing any bright stars in the image that would skew measurements of the ICL. The images are 370″ on a side.

2. **3σ Object Detection Mask:** We then run object detection on the image with a 3σ detection threshold using `photutils`. Groups of pixels which exceed the

---

[3]https://hsc-release.mtk.nao.ac.jp/archive/filetree/pdr3_wide/deepCoadd/ BrightObjectMasks/. This link can only be viewed with HSC membership.
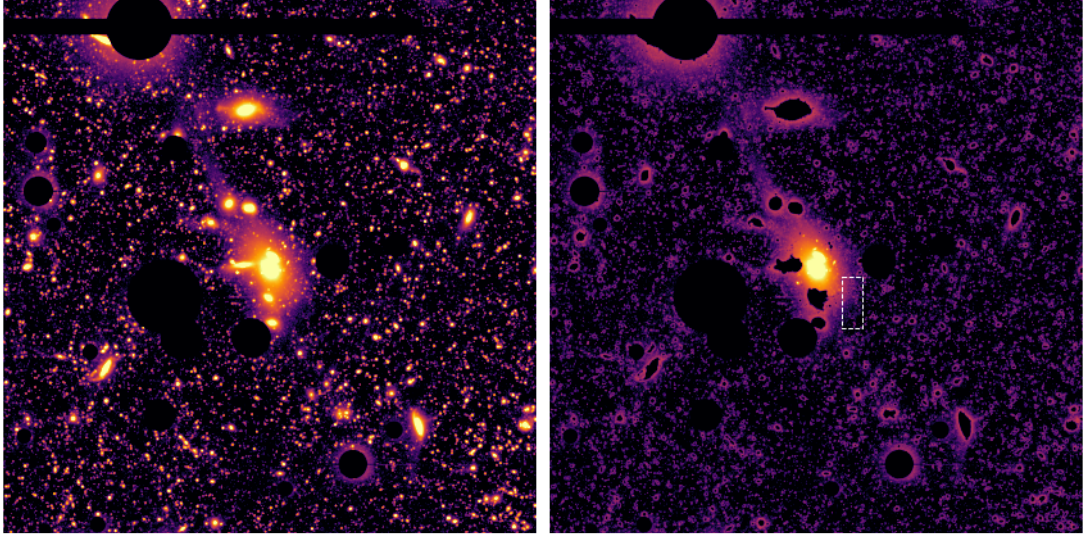
Figure 3.4: Same as in Figure 3.3, before and after the source mask is applied to the HSC-masked image. This constitutes the second mask layer, removing any bright, unmasked sources in the image that would skew measurements of the ICL. The images are 370″ on a side. In the right-hand panel, a dashed, white rectangle is shown – this corresponds to the region in Figure 3.5.

3σ threshold and have a connectivity greater than 6 are assigned to a source, ultimately leading to a segmentation image. We use the segmentation image to mask pixels that belong to sources. We omit the BCG from the mask, as this is handled by the surface brightness threshold mask. Figure 3.4 shows the cluster in Figure 3.3 after applying the second mask layer.

3. **Faint Object Detection Mask:** Intracluster globular clusters (ICGCs) tend to be concentrated in the core regions of galaxy clusters (e.g. Blakeslee, 1999; Longobardi et al., 2018; Lee et al., 2022). These, along with other faint dwarf satellites, can remain undetected in the previous mask layer because their flux peaks are swamped by the ICL. Therefore, to reveal and detect these peaks, we first perform a harsh background subtraction across the image (using a mesh size of 50 pixels) and then run source detection with a slightly lower 2σ threshold. The segmentation image array is used for the mask again and we make sure to omit repeated detections from the previous mask (as well as the BCG) – this is so that bright central galaxies are not overly-masked, which would diminish the ICL signal. The result of applying this mask layer is shown in Figure 3.5.
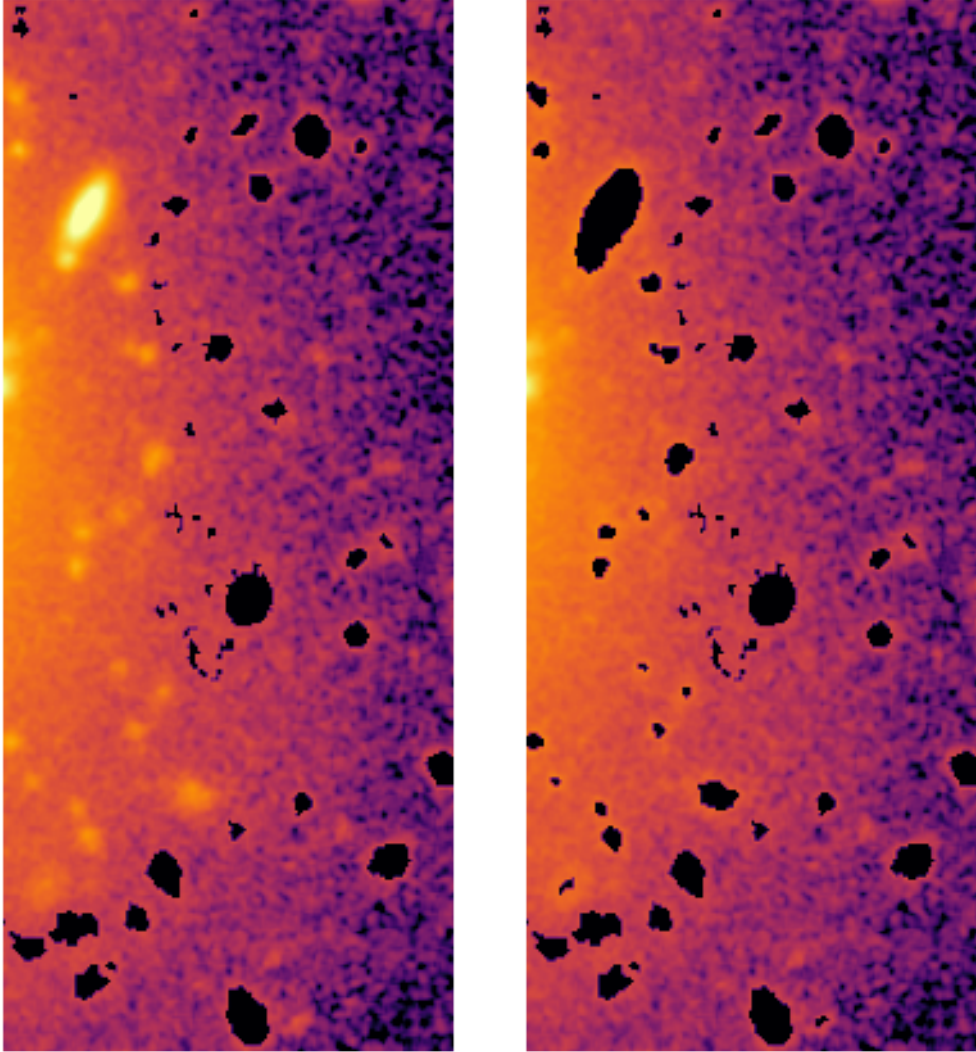
Figure 3.5: Same as in Figure 3.3 and Figure 3.4, before and after the faint source mask is applied. This constitutes the third mask layer, removing any faint, unmasked sources in the image, near to the BCG, that would skew measurements of the ICL. Note that in this image we have zoomed in to a region to the right of the BCG, to show more clearly that sources hidden by the bright regions of the ICL are being picked up and masked. These images correspond to a size of $15'' \times 30''$, and the region of this cutout is shown as the white dashed rectangle in Figure 3.4.

4. **Isophotal Threshold Mask:** The final layer of the mask is defined by a surface brightness threshold of $\mu_{B,rest} = 25\,\text{mag arcsec}^{-2}$ (as in Burke et al. 2015 and Furnell et al. 2021). Below this value, we assume that the flux is from the ICL. Since we are working with *i*-band data, we convert the restframe *B*-band limit to an observed *i*-band surface brightness using Eq. 6 in Furnell et al. (2021):

$$\mu_{i,obs} = \mu_{B,rest} + 2.5 \log_{10}(1 + z)^4 + k_{i,B}(z), \qquad (3.3)$$

where $\mu_{i,obs}$ is the limit at which we observe $\mu_{B,rest}$, $2.5 \log_{10}(1 + z)^4$ is the bolometric cosmological dimming term and $k_{i,B}(z)$ is the *k*-correction term. $k_{i,B}(z)$ is computed as follows:

$$k_{i,B}(z) = M_{i,obs}(z) - M_{B,rest}(z), \qquad (3.4)$$

where $M_{i,obs}(z)$ and $M_{B,rest}(z)$ are the pseudo-absolute magnitudes derived for each respective waveband as a function of redshift. To calculate these, we utilize Ezgal (Mancone & Gonzalez, 2012), assuming an old stellar population with a redshift of formation of $z_f = 3$, solar metallicity ($Z_\odot$), and subsequent passive evolution using the models of (Bruzual & Charlot, 2003) and a Chabrier IMF (Chabrier, 2003).

We perform source detection, as before, with $\mu_{i,obs}$ as the isophotal threshold. The mask is created using the segmentation image, whereby all connected pixels that are brighter than $\mu_{i,obs}$ at the position of the BCG are assigned to the BCG and masked (every other detected source brighter than $\mu_{i,obs}$ is omitted from this mask layer). In Figure 3.6 we show the cluster XMMXCS J022456.1-050802.0 without and with the four mask layers applied. We note that a few small sources close to the BCG do not get detected and masked, which is not the case for every cluster. This will not affect ICL measurements because sigma-clipping will be used to measure the ICL (see next section), which will omit flux peaks from the data. We do still stress, however, the importance of masking to establish a more accurate representation of the ICL-level, as sigma-clipping alone would struggle in cases where there are many unmasked sources (in which case, the average statistics may be based on the 'source-level' rather than the ICL-level). Furthermore, the omission of masking would particularly harm the errors on the ICL flux profile.
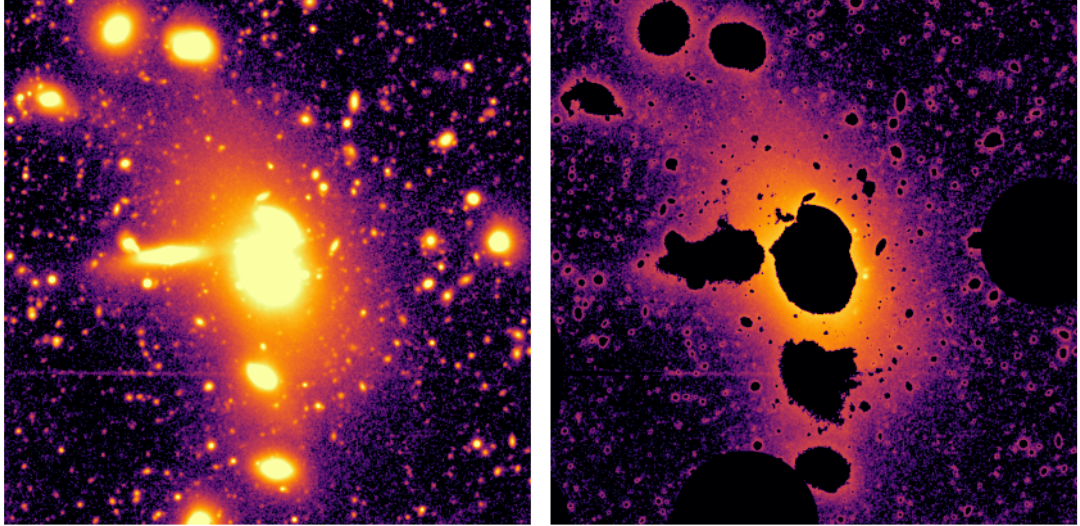
Figure 3.6: XMMXCS J022456.1-050802.0 before and after the full mask is applied, zoomed in to a region of 100″ on a side. While all the bright sources are clearly masked, some small sources very close to the BCG in the brightest regions of the ICL remain undetected. This is not an issue because sigma-clipping will be applied in measuring the ICL, removing contamination by such small objects.

3.5.2 Measuring the ICL

We quantify the ICL flux as that remaining after applying an isophotal threshold and masking out satellite galaxies, bad/saturated pixels and stars. We assume that the isophotal limit defines the BCG/ICL boundary and we measure the ICL out to a distance of R_{500}.

The ICL component of clusters tends to be strongly concentrated around the BCG (Mihos et al., 2005; Arnaboldi et al., 2012), so we use this position as the basis for the ICL centre. We measure the ICL in 200 nested elliptical annuli out to a semimajor axis of R_{500}. To estimate the axis ratio (q) and position angle (θ) of these annuli, we perform a flux-weighted principal-component analysis (PCA) on unmasked pixels out to a radius of $0.4R_{500}$ – we avoid going beyond this for the PCA as the ICL becomes much fainter, so it will be noisier and more susceptible to contamination from any faint galaxy wings that are not included in the mask. We begin by creating a column vector ($\mathbf{w}$) of the normalised pixel values as

$$\mathbf{w} = \frac{(\mathbf{f})^{\top}}{\sum\limits_{i,j} f_{i,j}}, \tag{3.5}$$

where $\mathbf{f}$ is a row vector containing the pixel values and $f_{i,j}$ is the value of pixel (i,j); note that measurements are done only using the pixels remaining after masking. We then compute the weighted covariance matrix of the pixel position vectors with respect

to the centre of the ICL (taken to be the position of the BCG), $\mathbf{X}$, as

$$\text{cov}(\mathbf{X}) = \frac{(\mathbf{X})^{\top}\mathbf{w} \cdot \mathbf{X}}{\sum \mathbf{w} - \frac{\sum \mathbf{w}^2}{\sum \mathbf{w}}}. \tag{3.6}$$

The eigenvalues ($\lambda_{a,b}$) and eigenvectors ($\mathbf{a}$, $\mathbf{b}$) are found by eigenvalue decomposition of cov($\mathbf{X}$), giving information about the semimajor and semiminor axes that best fit the flux-weighted unmasked pixel data. The axis ratio of an ellipse which best fits the data is found by taking the ratio of the square rooted eigenvalues for the semiminor (λ_b) and semimajor (λ_a) axis respectively, i.e.

$$q = \sqrt{\frac{\lambda_b}{\lambda_a}}. \tag{3.7}$$

The corresponding position angle is found by computing the arc-tangent of the semi-major axis eigenvector:

$$\theta = \arctan(\mathbf{b}). \tag{3.8}$$

Figure 3.7 shows the cluster XMMXCS J022456.1-050802.0 bounded by the ellipse defined by Equations 3.7 and 3.8 and a semi-major axis of R_{500}. This represents the outermost point where measurements of the ICL are made, with inner nested elliptical annuli defined by the same shape parameters.
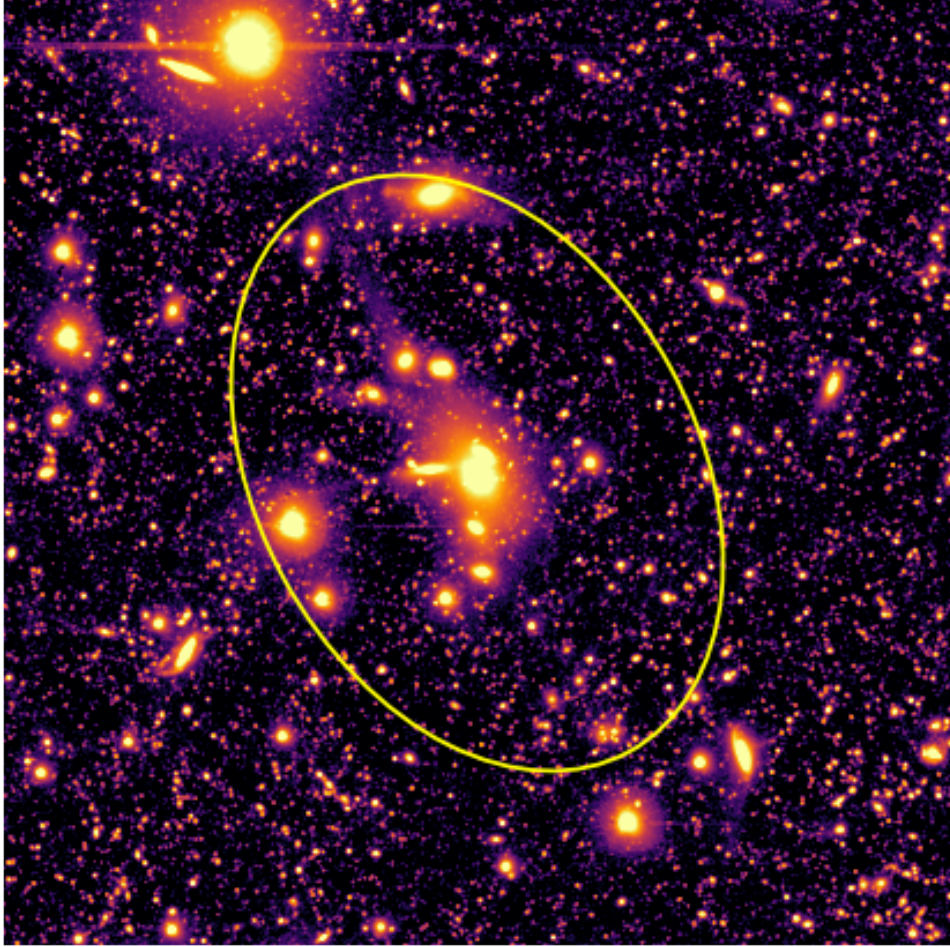
Figure 3.7: XMMXCS J022456.1-050802.0 with an ellipse overlaid, that is defined by the parameters calculated by PCA in Equations 3.7 and 3.8. The semi-major axis is equal to R_{500}. The image is $370''$ on a side.

For each annulus, k, we take the 3σ sigma-clipped mean value of the pixels ($\bar{f}_k$) as the flux of the ICL at that radius. Note that we also considered using the median value, which would be more robust to the shortcomings in the masking, but would have a larger error than the mean by a factor of $\sim \sqrt{2}$. Furthermore, using the median assumes that the true ICL surface brightness is constant within each annulus. However, the ICL may be expected to show some azimuthal structures, e.g. streams and shells, on top of the smooth distribution. Using the mean, albeit with some clipping, will include more of the flux from such ICL structures than would the median. The mean fluxes are converted to the equivalent surface brightness values, with errors derived from the standard error on $\bar{f}_k$ as follows:

$$e_k = \frac{\sigma_k}{\sqrt{N_k}}, \tag{3.9}$$

where σ_k is the standard deviation of the unmasked pixel values in annulus k and N_k is the number of unmasked pixels in annulus k. We then calculate the total ICL flux via

the following equation:

$$f_{\text{ICL}} = \sum_k N_{k,\text{tot}} \bar{f}_k, \tag{3.10}$$

where $N_{k,\text{tot}}$ is the total number of pixels in annulus k. Likewise, the total error on f_{ICL} is found by the following:

$$e_{\text{ICL}} = \sqrt{\sum_k (N_{k,\text{tot}}\alpha_k)^2}. \tag{3.11}$$

3.5.3 Estimating the Total Flux of Cluster Galaxies

In order to determine the ICL fraction, not only is the ICL flux required, but also the total flux of the galaxies in the cluster. Ideally, one would identify which galaxies are cluster members, but this is uncertain. Instead, we exclude galaxies that are unlikely to be cluster members, and then calibrate a statistical correction to remove the contributions of remaining non-members. We begin by obtaining source catalogs for each of the four HSC deep fields out to a redshift of $z = 1.6$. We also assert $z > 0.01$ to omit stars from the catalogs. For every source, these catalogues contain the: position (RA, dec), i-band Kron magnitude (Kron, 1980), photometric redshift (photo-z) and (where available) spectroscopic redshift (spec-z). The photo-zs are computed via DEmP (Hsieh & Yee, 2014). The spec-zs originate from the works of several previous authors - these are listed as follows: Lilly et al. (2009); Bradshaw et al. (2013); McLure et al. (2013); Skelton et al. (2014); Momcheva et al. (2016); Silverman et al. (2015); Le Fèvre et al. (2013); Garilli et al. (2014); Ahumada et al. (2020); Pâris et al. (2018); Liske et al. (2015); Drinkwater et al. (2010); Davis et al. (2003); Newman et al. (2013); Cooper et al. (2011, 2012); Coil et al. (2011); Cool et al. (2013); Colless et al. (2003); Jones et al. (2004, 2009); Masters et al. (2017, 2019); Hasinger et al. (2018); Straatman et al. (2018); Pentericci et al. (2018).

Figure 3.8 shows the position on the sky for each object contained within the deep field catalogs, separated out by photo-z-only or spec-z candidates. While the XMMLSS field appears to have a reasonable coverage of spec-zs, apart from the northern-most region, the other three fields are much more sparse (particularly ELAISN1). The spec-z objects in the COSMOS field are most strongly concentrated in the central-south east region; in the DEEP23 field they are more concentrated in the north region. In Figure 3.9, the redshift distribution for each deep field is plotted for the photo-z and spec-z candidates. It is evident that there are far fewer spec-z objects than photo-z objects across the four fields, meaning that a large proportion of members for every cluster will be designated based on photometric data. Due to the uncertain nature of photometric measurements, each cluster will potentially contain contaminant members, thus impacting estimates of
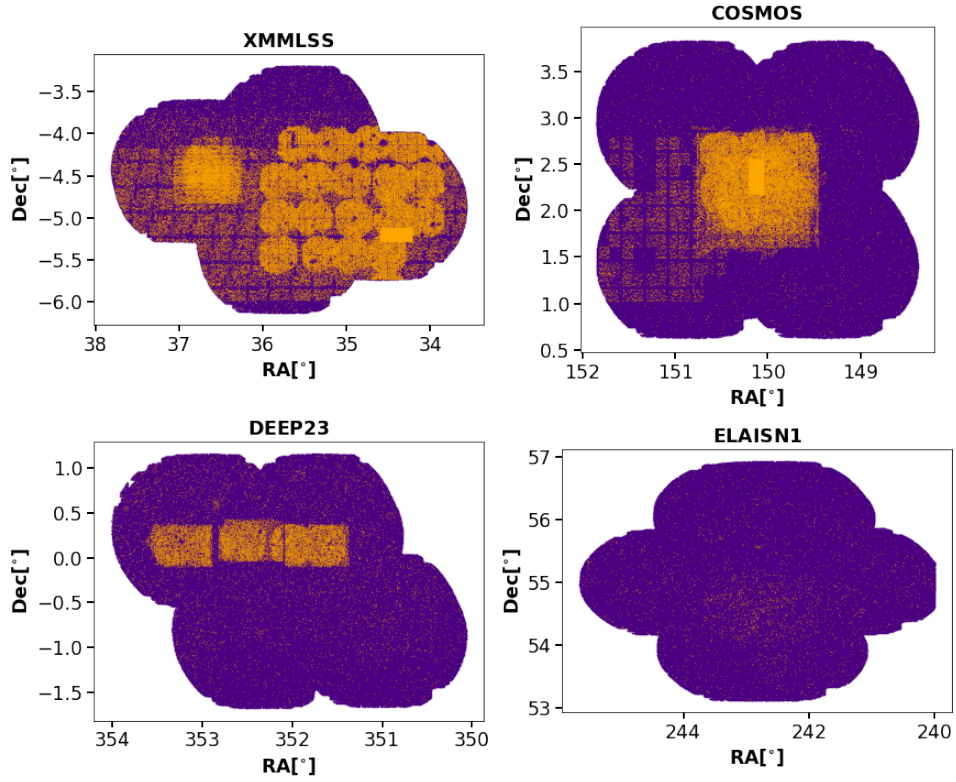
Figure 3.8: Objects from each of the four HSC deep field catalogs out to $z = 1.6$. The magenta data points are objects that only have photometric redshifts, while the yellow data points are objects that have spectroscopic redshifts.
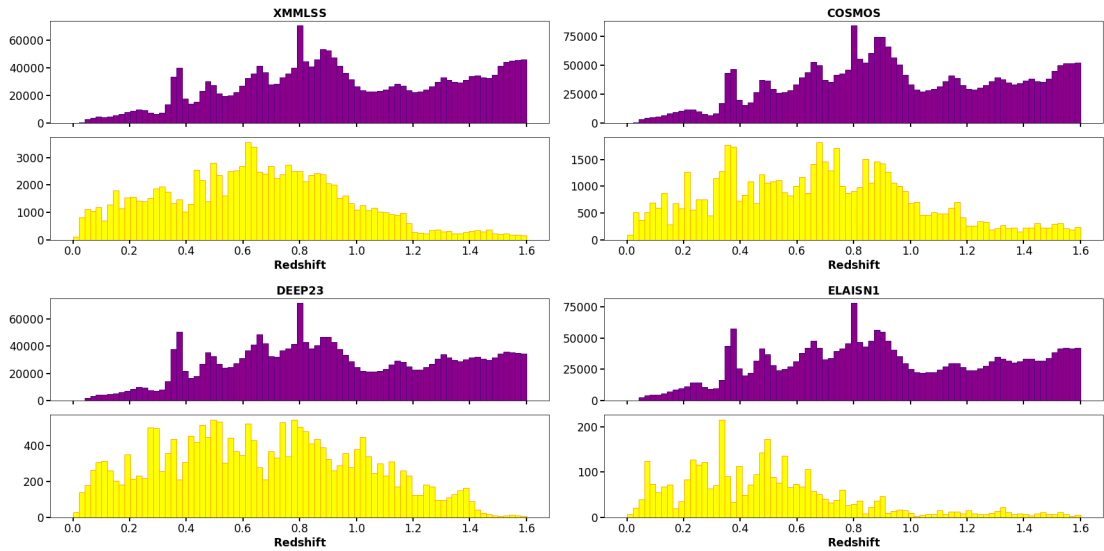
Figure 3.9: Redshift distributions of photometric (magenta) and spectroscopic (yellow) candidates for each deep field, plotted separately due to the small amount of spec-zs compared with photo-zs. Each bin is equivalent to $\Delta z = 0.02$. Note the different vertical scales.

50

total cluster galaxy flux. To minimise this, we apply a 'background correction' after assigning membership to objects (discussed later in this section).

Spectroscopic redshifts are typically more accurate than the cluster velocity dispersion, so the latter can be used to determine membership. On the other hand, the uncertainties on photo-zs are significantly larger than the cluster velocity dispersion, so we can only determine potential cluster members. For objects with spectroscopic redshifts (z_{spec}), we attribute membership to those with spec-zs which fall within a $3\sigma_v$ slice of the cluster redshift (z_{cl}), where σ_v is the velocity dispersion relative to the cluster. We adopt a value of $3\sigma_v = 3000\,\mathrm{kms}^{-1}$ for each cluster, which is towards the upper limit of that typical of galaxy clusters (Struble & Rood, 1999). The redshift slice relative to z_{cl} that corresponds to this velocity dispersion is given by

$$\Delta z_{\mathrm{cl}} = \frac{3\sigma_v}{c}(1 + z_{\mathrm{cl}}), \tag{3.12}$$

where c is the speed of light. Therefore, membership is assigned to all objects contained within an aperture of R_{500} that satisfy $|z_{\mathrm{cl}} - z_{\mathrm{spec}}| \leq \Delta z_{\mathrm{cl}}$. This provides us with a catalog of $N_{\mathrm{spec,cl}}$ member galaxies for each cluster.

In the case of objects with photo-zs, we use the typical error on each measurement (σ_{phot}) to identify candidate cluster members, since this tends to be much larger than Δz_{cl}. Within the redshift range $0.2 \leq z_{\mathrm{phot}} \leq 1.5$, the typical error on the photo-zs is $\sigma_{\mathrm{phot}} \sim 0.05$ (Tanaka et al., 2018). We take Δz_{phot} to be equivalent to a $3\sigma_{\mathrm{phot}}$ spread on each measurement of z_{phot}, i.e.

$$\Delta z_{\mathrm{phot}} = 3\sigma_{\mathrm{phot}}(1 + z_{\mathrm{phot}}). \tag{3.13}$$

Thus, the membership condition in this case is that $|z_{\mathrm{cl}} - z_{\mathrm{phot}}| \leq \Delta z_{\mathrm{phot}}$ within an aperture of R_{500}, providing us with a catalog of $N_{\mathrm{phot,cl}}$ candidate member galaxies for each cluster.

'Contaminant' foreground and background galaxies may also be assigned as candidate cluster members. To account for this, we estimate the contribution from these contaminant galaxies by placing n R_{500}-sized apertures (we choose $n = 4000$, sufficient to accurately estimate the average contamination and its standard deviation) at random positions across the entire field to which that cluster belongs. For each aperture, we count how many galaxies have photo-zs that would satisfy the membership condition for a cluster at $z = z_{\mathrm{cl}}$. We therefore obtain a distribution for the number (N_{bg}) of photo-z candidate members in the absence of a cluster. From this distribution we estimate a mean of $\bar{N}_{\mathrm{bg}}$ and standard deviation $\sigma_{N,\mathrm{bg}}$. Figure 3.10 shows the distribution of N_{bg} for one cluster.
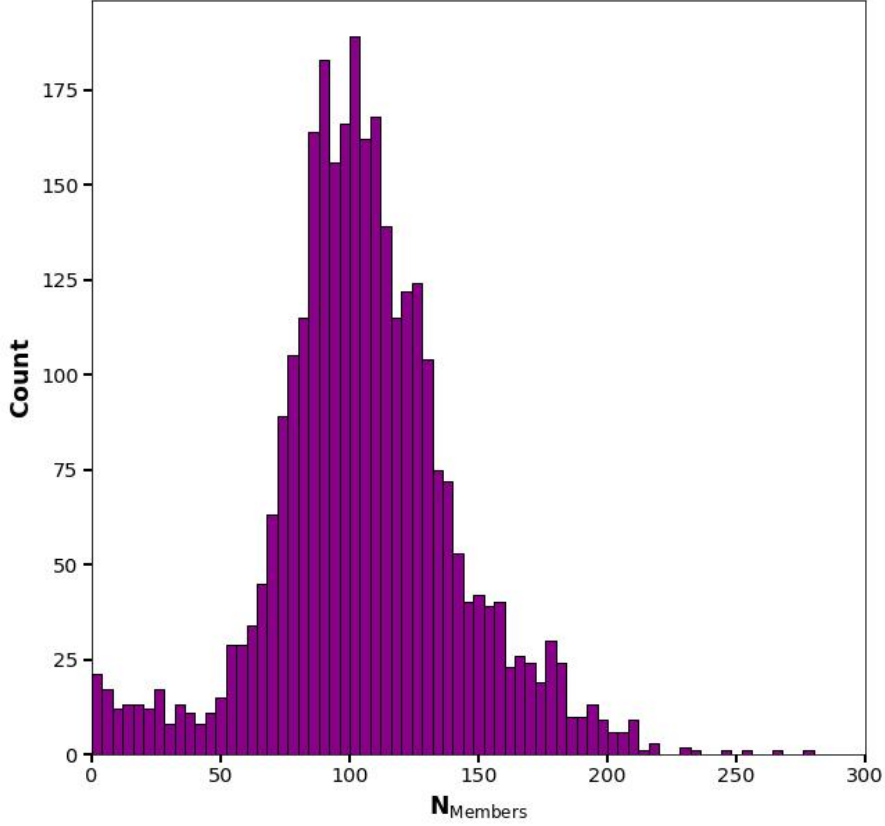
Figure 3.10: The distribution of galaxies that satisfy the photometric membership criteria for XMMXCS J022456.1-050802.0 in the field. The mean membership of this distribution is $\bar{N}_{\mathrm{bg}} \sim 100$ galaxies.

While we count all galaxies in the random apertures, we only counted those without spec-zs in the cluster aperture, meaning that if we did not adjust our background estimate, it would represent a larger correction than what is needed. Therefore, to account for this we scale-down our estimates of $\bar{N}_{\mathrm{bg}}$ and $\sigma_{N,\mathrm{bg}}$ by multiplying them by $c_N = \frac{N_{\mathrm{phot,cl}}}{N_{\mathrm{phot,cl}}(A \vee B)}$, where $N_{\mathrm{phot,cl}}(A \vee B)$ is the number of galaxies with z_{phot} which satisfies the photometric membership criterion either without spectroscopic data (A) or having spectroscopic data that does not meet the spectroscopic membership criterion (B). With that, the corrected value for number of photometric cluster members is given by

$$N^*_{\mathrm{phot,cl}} = N_{\mathrm{phot,cl}} - \bar{N}_{\mathrm{bg}}c_N. \tag{3.14}$$

We then take the sum of the *i*-band fluxes of the photo-*z* cluster members ($f_{\text{phot,cl}}$) and correct for the excess background flux with the following equation:

$$f_{\text{phot,cl}}^{N-\text{corr}} = \left(\frac{N_{\text{phot,cl}}^{*}}{N_{\text{phot,cl}}}\right) f_{\text{phot,cl}}. \tag{3.15}$$

The error on $f_{\text{phot,cl}}^{N-\text{corr}}$ is calculated as

$$e_{\text{phot,cl}}^{N-\text{corr}} = \left(\frac{\sigma_{N,\text{bg}} c_{N}}{N_{\text{phot,cl}}}\right) f_{\text{phot,cl}}. \tag{3.16}$$

Equations 3.14–3.16 assume that the average flux of the contaminant galaxies is the same as that of the true photo-z cluster members, which may not always hold true. Instead of simply counting the number of candidate cluster members in each random aperture, we sum their fluxes. From these we estimate the average contribution of contaminant galaxies to $f_{\text{phot,cl}}$, and its error. Again, we must correct for the fact that spectroscopic non-members have been removed from the cluster aperture, but not the random apertures. In this case, a scale factor of $c_{f} = \frac{f_{\text{phot,cl}}}{f_{\text{phot,cl}(A \lor B)}}$ is applied to the average flux level ($\bar{f}_{\text{bg}}$) and standard deviation ($\sigma_{f,\text{bg}}$) across the *n* apertures, giving the following:

$$f_{\text{phot,cl}}^{f-\text{corr}} = f_{\text{phot,cl}} - \bar{f}_{\text{bg}} c_{f}, \tag{3.17}$$

$$e_{\text{phot,cl}}^{f-\text{corr}} = \sigma_{f,\text{bg}} c_{f}. \tag{3.18}$$

Figure 3.11 shows the distribution of f_{bg} for XMMXCS J022456.1-050802.0.

Using the above, we calculate two ICL fractions, depending on whether we use the membership-corrected photo-*z* member flux, $f_{\text{phot,cl}}^{N-\text{corr}}$, or the flux-corrected photo-*z* member flux, $f_{\text{phot,cl}}^{f-\text{corr}}$ - the latter should typically be less biased, but may be skewed by the presence of very bright objects in some of the random apertures. This is given by:

$$\phi^{x-\text{corr}} = \frac{f_{\text{ICL}}}{f_{\text{ICL}} + f_{\text{gal}}} = \frac{f_{\text{ICL}}}{f_{\text{ICL}} + f_{\text{spec,cl}} + f_{\text{phot,cl}}^{x-\text{corr}}}, \tag{3.19}$$

where $f_{\text{spec,cl}}$ is the total flux from spec-*z* cluster galaxies and *x* indicates either membership or flux-corrected cases. The error on $\phi^{x-\text{corr}}$ is calculated as follows:

$$e_{\phi}^{x-\text{corr}} = \phi^{x-\text{corr}} \sqrt{\left(\frac{\sqrt{\left(e_{\text{phot,cl}}^{x-\text{corr}}\right)^2 + e_{\text{ICL}}^2}}{f_{\text{ICL}} + f_{\text{gal}}}\right)^2 + \left(\frac{e_{\text{ICL}}}{f_{\text{ICL}}}\right)^2}. \tag{3.20}$$
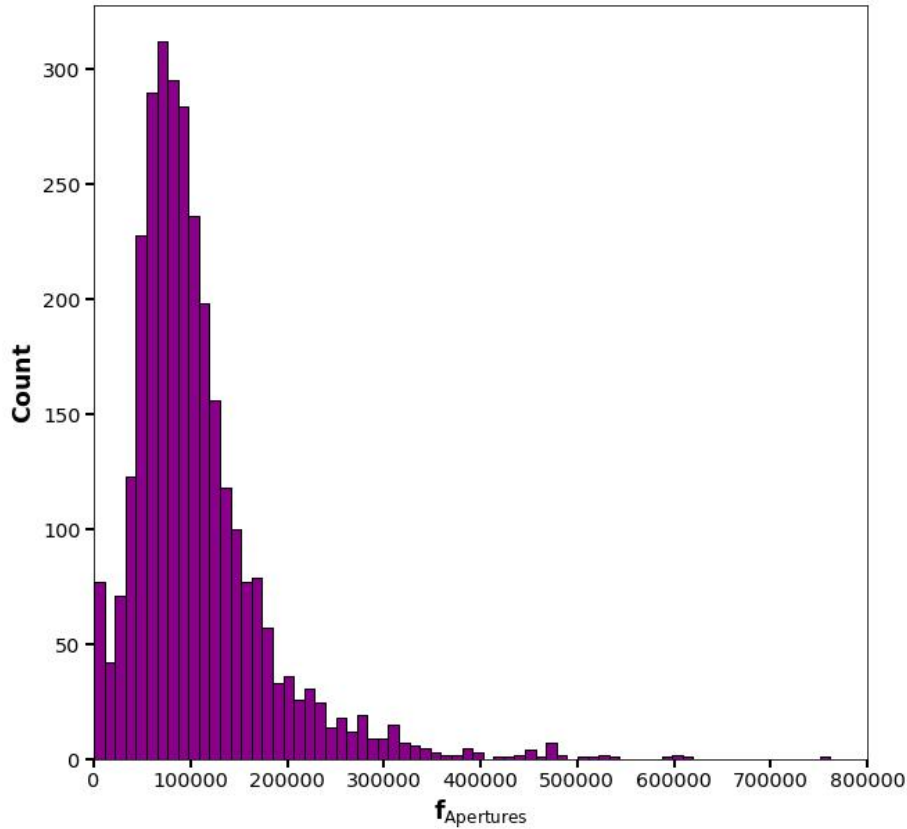
Figure 3.11: The distribution of total galaxy fluxes within R_{500}-sized apertures in the field that satisfy the photometric membership criteria for XMMXCS J022456.1-050802.0. The mean flux of this distribution is $\bar{f}_{\mathrm{bg}} \sim 100000$ counts.

We find that, after scaling, typically $(42.5 \pm 1.4)\%$ of photo-z candidate members are designated as genuine cluster members. We also find that the uncertainty on the total galaxy flux (originating from the photo-z measurements) dominates the ultimate ICL fraction uncertainty, as opposed to the uncertainty on the ICL measurement.

3.6 Results

3.6.1 The XCS Sample and Comparison to Furnell et al. (2021)

For each cluster, we generate an observed i-band surface brightness profile of the ICL using the 3σ sigma-clipped mean values of the unmasked pixels in elliptical annuli ($\bar{f}_k$), going out to R_{500}. Figure 3.12 shows the profile we obtained for the cluster XMMXCS J022456.1-050802.0; in this plot, along with some of the input parameters listed in

Table 3.1, we include the main parameters output by our analysis: the ICL fractions in both corrected cases, the total flux (in counts) of the galaxies in both corrected cases and the total flux (in counts) of the ICL. The ICL flux corresponds to an *i*-band magnitude of $M_i = -22.3$, which was obtained using the conversion

$$M_i = -2.5 \log_{10}(F) + m_{\text{zp}} - 5 \log_{10}\left(\frac{d}{10}\right),\qquad(3.21)$$

where F is the flux of the ICL in counts, $m_{\text{zp}} = 27.0$ is the zeropoint magnitude of HSC and d is the comoving distance to the cluster. The plots for the rest of the clusters in the sample can be seen in Figure A.1. Figure 3.12 demonstrates that the ICL is most strongly concentrated around the BCG, where it has the highest surface brightness, and decreases radially until it becomes indistinguishable from the residual background noise. In elliptical annuli, containing typically ~1000 pixels, the surface brightness values are reaching below 28mag arcsec^{-2}. For this cluster, we measure a convincing ICL profile out to around $0.5R_{500}$, which is around 160kpc along the semimajor axis. It is worth reiterating here that we do not consider anything brighter than $\mu_{B,rest} = $ 25mag arcsec^{-2} to be ICL, which is equivalent to $\mu_{i,obs} = 23.8$mag arcsec^{-2}. The BCG is the masked object at the centre of Figure 3.12 and it extends to a radius of around 20kpc, meaning that we measure the ICL to around 10× that of the BCG - this range is similar to that in Furnell et al. (2021). Although we do not analyse the ICL profiles further in this work, we hope to use them to quantify the extent of the ICL in future work.
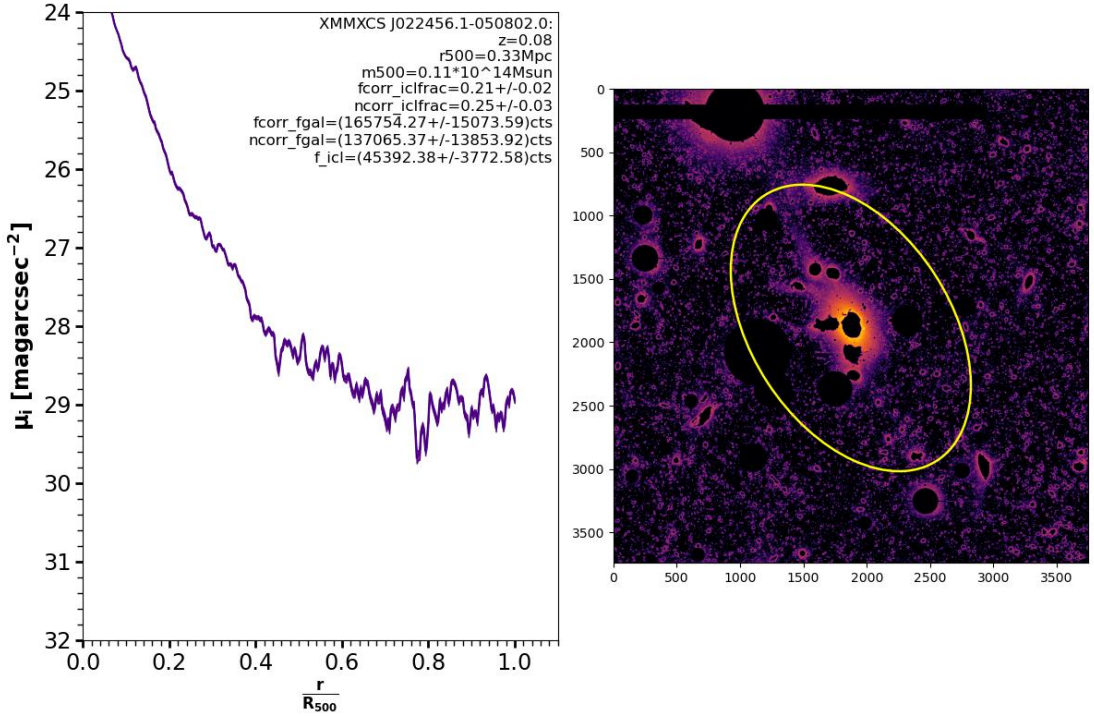
Figure 3.12: The observed-frame *i*-band surface brightness profile of the ICL computed for the cluster XMMXCS J022456.1-050802.0 (left) alongside the respective fully masked image (right), which was created using the methodology set out in Section 3.5.1 – the image is 370″ on a side. On the surface brightness plot we have included relevant input and output parameters of our analysis, with *r* being the semi-major axis of the elliptical annuli, and on the image we have overlaid a yellow ellipse which extends to R_{500}, with the shape parameters calculated using the methodology in Section 3.5.2.

We measure a statistically significant ICL fraction in every cluster, with a significance of $>3\sigma$, and typically $\sim5\sigma$. For these massive X-ray clusters, we find an average N-corrected(F-corrected) ICL fraction of 0.23(0.22), with a standard deviation of 0.08(0.09). These values are very similar to the average ICL fraction of 0.24 found by Furnell et al. (2021), who used the same sample of clusters. Table 3.3 shows the main results of this work for the XCS sample of clusters. We compare our corrected ICL fractions those of Furnell et al. (2021) in Figure 3.13. We find that, although the mean and scatter of our ICL fractions aligns nicely with the work of Furnell et al. (2021), there are significant differences between the measurements for individual clusters. We discuss this further in Section 3.7. In Figure 3.14 and Figure 3.15, we plot the corrected ICL fractions as a function of redshift and M_{500} respectively. We also include the results from Furnell et al. (2021) on these plots.

We performed Spearman's Rank analysis to check if any correlation exists in either case, using `Pingouin` (Vallat, 2018). Here, we take *p*-values less than 5% as evidence of a correlation, which corresponds to values less than $\log_{10}(p_S) = -1.3$. For Fig-

ure 3.14, we obtained a Spearman's rank correlation coefficient of $r_S = 0.095$ and a corresponding p-value of $\log_{10}(p_S) = -0.15$ in both corrected cases, indicating that there is no obvious correlation between ICL fraction and redshift. This is in disagreement with Furnell et al. (2021), who found a strong anti-correlation with $r_S = -0.79$ and $\log_{10}(p_S) = -4.02$. We then computed the partial Spearman coefficients, controlling for cluster mass, but there was still no correlation ($r_S = 0.053$ and $\log_{10}(p_S) = -0.075$ in the N-corrected case and $r_S = -0.018$ and $\log_{10}(p_S) = -0.024$ in the F-corrected case – the partial coefficients in Furnell et al. 2021 still showed strong anti-correlation). We carried out the same calculations on Figure 3.15 and obtained Spearman coefficients of $r_S = 0.10(0.24)$ and $\log_{10}(p_S) = -0.17(-0.46)$ in the N-corrected(F-corrected) case, indicating a lack of correlation between ICL fraction and cluster mass. This is in agreement with what Furnell et al. (2021) found. When controlling for redshift, the partial Spearman coefficients still translate to a lack of correlation between cluster mass and ICL fraction ($r_S = 0.068$ and $\log_{10}(p_S) = -0.10$ in the N-corrected case and $r_S = 0.22$ and $\log_{10}(p_S) = -0.40$ in the F-corrected case). The implications of what we have found here are discussed in Section 3.7.

Table 3.3: The main results for the XCS sample of clusters from this work. We have included, for each cluster, the ICL fraction with no photometric contamination correction ($\phi_{\text{uncorrected}}$), the ICL fractions with photometric corrections set out in Equations 3.15 and 3.17 ($\phi^{N-\text{corr}}$ and $\phi^{f-\text{corr}}$ respectively) and their respective errors ($e_\phi^{N-\text{corr}}$ and $e_\phi^{f-\text{corr}}$).

XCS ID	$\phi_{\text{uncorrected}}$	$\phi^{N-\text{corr}}$	$e_\phi^{N-\text{corr}}$	$\phi^{f-\text{corr}}$	$e_\phi^{f-\text{corr}}$
XMMXCS J022456.1-050802.0	0.18	0.25	0.03	0.21	0.02
XMMXCS J161039.2+540604.0	0.12	0.18	0.02	0.18	0.03
XMMXCS J233137.8+000735.0	0.08	0.17	0.03	0.12	0.02
XMMXCS J232923.6-004854.7	0.18	0.30	0.03	0.37	0.10
XMMXCS J161134.1+541640.5	0.13	0.19	0.02	0.19	0.02
XMMXCS J095902.7+025544.9	0.10	0.16	0.02	0.20	0.07
XMMXCS J095901.2+024740.4	0.14	0.23	0.03	0.18	0.02
XMMXCS J100141.6+022538.8	0.12	0.16	0.01	0.16	0.02
XMMXCS J095737.1+023428.9	0.05	0.08	0.01	0.06	0.00
XMMXCS J022156.8-054521.9	0.17	0.26	0.03	0.25	0.04
XMMXCS J022148.1-034608.0	0.18	0.30	0.03	0.27	0.03
XMMXCS J022530.8-041421.1	0.19	0.31	0.04	0.32	0.08
XMMXCS J100047.3+013927.8	0.09	0.15	0.02	0.15	0.02
XMMXCS J022726.5-043207.1	0.24	0.44	0.08	0.40	0.09
XMMXCS J022524.8-044043.4	0.16	0.24	0.03	0.25	0.04
XMMXCS J095951.2+014045.8	0.18	0.26	0.02	0.25	0.04
XMMXCS J022401.9-050528.4	0.19	0.30	0.03	0.32	0.08
XMMXCS J095924.7+014614.1	0.10	0.15	0.01	0.16	0.03
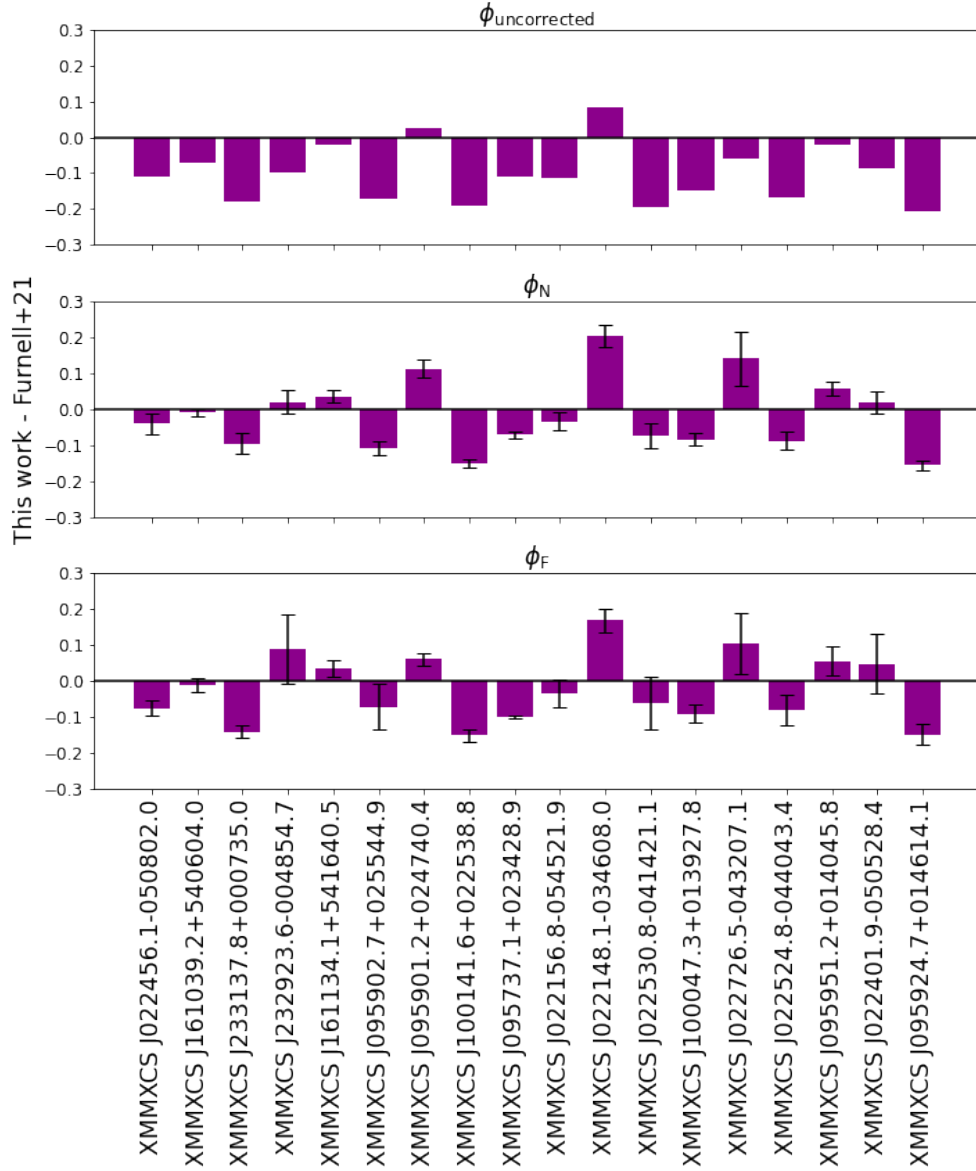
Figure 3.13: The residuals of the XCS sample ICL fractions derived from this work subtracted from those from Furnell et al. (2021) for each cluster. We show the residuals for the uncorrected case and for both corrected cases from this work. For the corrected ICL fractions, we also give the linearly combined errors from both works (we note that the errors given in Furnell et al. 2021 are unrealistically small). Most clusters have nonzero residuals, even taking into account the combined errors.
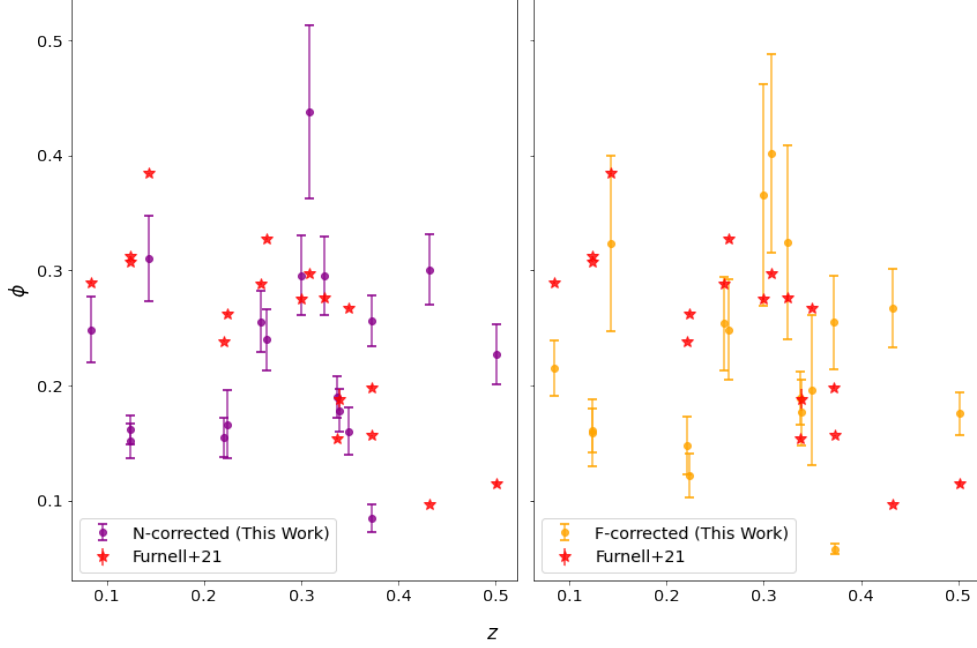
Figure 3.14: The ICL fraction of the XCS-Sample as a function of redshift in the N-corrected case (left) and the F-corrected case (right). Also plotted are the results from Furnell et al. (2021) (red stars). While the work of Furnell et al. (2021) shows a strong anti-correlation between ICL fraction and redshift, no correlation is exhibited by the results of this work.

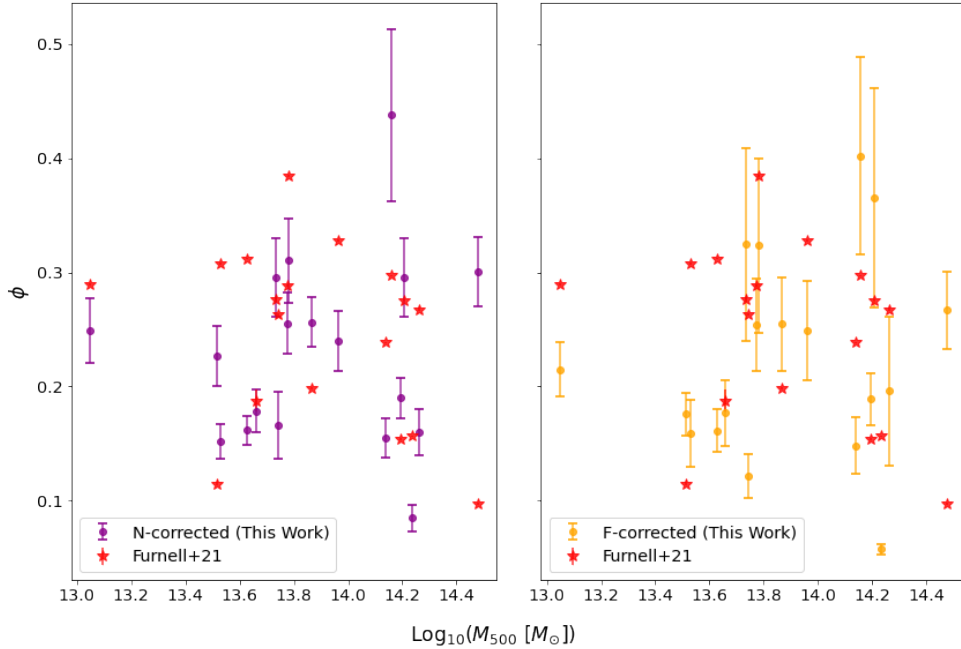**Figure 3.15:** The ICL fraction as a function of cluster mass (M_{500}) in the N-corrected case (left) and the F-corrected case (right). Also plotted are the results from Furnell et al. (2021) (red stars). In both this work and Furnell et al. (2021), no correlation is found between ICL fraction and cluster mass.

3.6.2 The CAMIRA Sample

The ICL profiles of the CAMIRA-detected sample of clusters are given in Figure A.2, which is formatted in the same way as in Figure A.1 but with richness provided instead of M_{500}. Using the R_{500} values derived in Section 3.4.2, we estimate the range in M_{500} values for the CAMIRA sample to be $0.473 < (\frac{M_{500}}{M_\odot} \times 10^{14}) < 3.367$, corresponding to a richness range of $20 < N < 93$; this compares with the range in M_{500} values from the XCS sample of $0.112 < (\frac{M_{500}}{M_\odot} \times 10^{14}) < 3.001$. As with the XCS sample, we detect ICL in every cluster. The average N-corrected(F-corrected) ICL fraction is found to be 0.25(0.24), with a standard deviation of 0.11(0.10). These values are extremely similar to the average ICL fractions from the XCS sample. Note here that the scatter of the ICL fractions is generally larger than the error bars on the individual measurements, meaning that the total scatter is dominated by the differences in ICL fractions between the clusters, rather than by their individual uncertainties. We give the main results of the 54 CAMIRA clusters in Table 3.4.

When plotting the ICL fractions as a function of redshift (Figure 3.16), we find no correlation between the two, with $r_S = 0.19(0.084)$ and $\log_{10}(p_S) = -0.83(-0.28)$ in the N-corrected(F-corrected) case. We also control for richness (as we assume this correlates with M_{500}) and perform partial Spearman analysis and find that there is still no correlation ($r_S = 0.19(0.10)$ and $\log_{10}(p_S) = -0.81(-0.37)$ in the N-corrected(F-corrected) case). When combining the ICL fractions and their respective redshifts with those of the XCS sample, the Spearman analysis produces $r_S = 0.17(0.084)$ and $\log_{10}(p_S) = -0.33(-0.87)$ in the N-corrected(F-corrected) case. We find an average ICL fraction across both samples, for all redshifts, of $\phi_N = 0.25$ and $\phi_F = 0.24$, which is in line with those found in previous studies (Jiménez-Teja et al., 2018; Kluge et al., 2021; Ragusa et al., 2021; Furnell et al., 2021).

In Figure 3.17, we plot the ICL fractions of the CAMIRA-detected sample as a function of richness. We find that these do not correlate, with $r_S = -0.028(0.080)$ and $\log_{10}(p_S) = -0.081(-0.27)$ in the N-corrected(F-corrected) case. This conclusion does not change when controlling for redshift, as partial Spearman's analysis gives $r_S = 0.014(0.10)$ and $\log_{10}(p_S) = -0.037(-0.35)$ in the N-corrected(F-corrected) case. If one assumes that cluster mass and richness are correlated, this agrees with what was found in the XCS sample of clusters in Figure 3.15 and in Furnell et al. (2021).

Table 3.4: The main results for the CAMIRA-detected sample of clusters from this work. We have included, for each cluster, the ICL fraction with no photometric contamination correction ($\phi_{\text{uncorrected}}$), the ICL fractions with photometric corrections set out in Equations 3.15 and 3.17 ($\phi^{N-\text{corr}}$ and $\phi^{f-\text{corr}}$ respectively) and their respective errors ($e_\phi^{N-\text{corr}}$ and $e_\phi^{f-\text{corr}}$).

CAMIRA-HSC ID	$\phi_{\text{uncorrected}}$	$\phi^{N-\text{corr}}$	$e_\phi^{N-\text{corr}}$	$\phi^{f-\text{corr}}$	$e_\phi^{f-\text{corr}}$
HSCJ021528-044041	0.23	0.37	0.04	0.38	0.07
HSCJ021635-042812	0.07	0.08	0.01	0.08	0.01
HSCJ021837-054025	0.27	0.43	0.06	0.44	0.11
HSCJ021942-045231	0.25	0.33	0.02	0.40	0.08
HSCJ022351-053640	0.14	0.20	0.02	0.18	0.02
HSCJ022358-043505	0.12	0.16	0.01	0.15	0.02
HSCJ022433-041419	0.11	0.15	0.01	0.14	0.02
HSCJ022636-040410	0.30	0.43	0.06	0.44	0.09
HSCJ022828-042608	0.09	0.13	0.01	0.13	0.02
HSCJ022933-043948	0.15	0.33	0.06	0.23	0.04
HSCJ023028-043349	0.16	0.33	0.07	0.26	0.05
HSCJ095536+010310	0.18	0.28	0.03	0.26	0.04
HSCJ095606+023650	0.15	0.24	0.02	0.22	0.04
HSCJ095728+033956	0.17	0.35	0.07	0.39	0.15
HSCJ095824+024916	0.16	0.22	0.02	0.21	0.02
HSCJ095918+033052	0.12	0.23	0.05	0.16	0.03
HSCJ100022+022328	0.07	0.10	0.01	0.10	0.02
HSCJ100252+031427	0.14	0.25	0.03	0.27	0.08
HSCJ100300+013152	0.21	0.37	0.06	0.31	0.05
HSCJ100452+025434	0.12	0.19	0.02	0.19	0.03
HSCJ100459+015442	0.13	0.60	0.39	0.29	0.12
HSCJ100532+023518	0.15	0.25	0.03	0.26	0.06
HSCJ160159+552418	0.16	0.32	0.06	0.30	0.08
HSCJ160434+551301	0.10	0.20	0.04	0.20	0.07
HSCJ160439+543137	0.14	0.24	0.03	0.27	0.05
HSCJ160508+545208	0.15	0.31	0.05	0.40	0.21
HSCJ160551+544727	0.10	0.17	0.03	0.14	0.02
HSCJ160600+545854	0.09	0.18	0.03	0.18	0.06
HSCJ160605+542841	0.17	0.29	0.03	0.33	0.11
HSCJ160633+535359	0.10	0.22	0.04	0.18	0.04
HSCJ160639+560806	0.23	0.36	0.03	0.42	0.12
HSCJ160903+534302	0.23	0.43	0.07	0.58	0.31
HSCJ161101+561748	0.07	0.12	0.02	0.20	0.09
HSCJ161112+553451	0.10	0.16	0.02	0.16	0.02
HSCJ161221+532107	0.09	0.33	0.14	0.22	0.08
HSCJ161225+555438	0.07	0.14	0.03	0.15	0.05
HSCJ161249+540837	0.10	0.21	0.04	0.19	0.04
HSCJ161317+560119	0.12	0.19	0.02	0.19	0.04
HSCJ161412+554132	0.08	0.16	0.03	0.14	0.04
HSCJ161415+544328	0.13	0.18	0.02	0.20	0.03

Table 3.4 – continued from previous page

CAMIRA-HSC ID	$\phi_{\text{uncorrected}}$	$\phi^{N-\text{corr}}$	$e_{\phi}^{N-\text{corr}}$	$\phi^{f-\text{corr}}$	$e_{\phi}^{f-\text{corr}}$
HSCJ161434+542551	0.08	0.13	0.01	0.13	0.02
HSCJ161634+553955	0.16	0.31	0.05	0.34	0.10
HSCJ161704+545025	0.08	0.16	0.03	0.14	0.04
HSCJ161826+542543	0.11	0.22	0.04	0.19	0.05
HSCJ161834+551751	0.10	0.17	0.02	0.17	0.03
HSCJ161915+551341	0.13	0.24	0.04	0.20	0.04
HSCJ161925+551436	0.14	0.26	0.03	0.23	0.05
HSCJ232209-012057	0.17	0.29	0.05	0.26	0.05
HSCJ232540-001112	0.09	0.17	0.03	0.13	0.02
HSCJ232732+005634	0.13	0.25	0.04	0.30	0.10
HSCJ233015-011940	0.13	0.19	0.02	0.17	0.02
HSCJ233031+003810	0.08	0.22	0.06	0.22	0.11
HSCJ233128+003654	0.23	0.34	0.03	0.37	0.07
HSCJ233328-000122	0.21	0.36	0.05	0.40	0.13

Figure 3.16: The ICL fraction of the CAMIRA-detected sample as a function of redshift in the N-corrected case (left) and the F-corrected case (right). As in Figure 3.14, no correlation is exhibited by the results of this work.
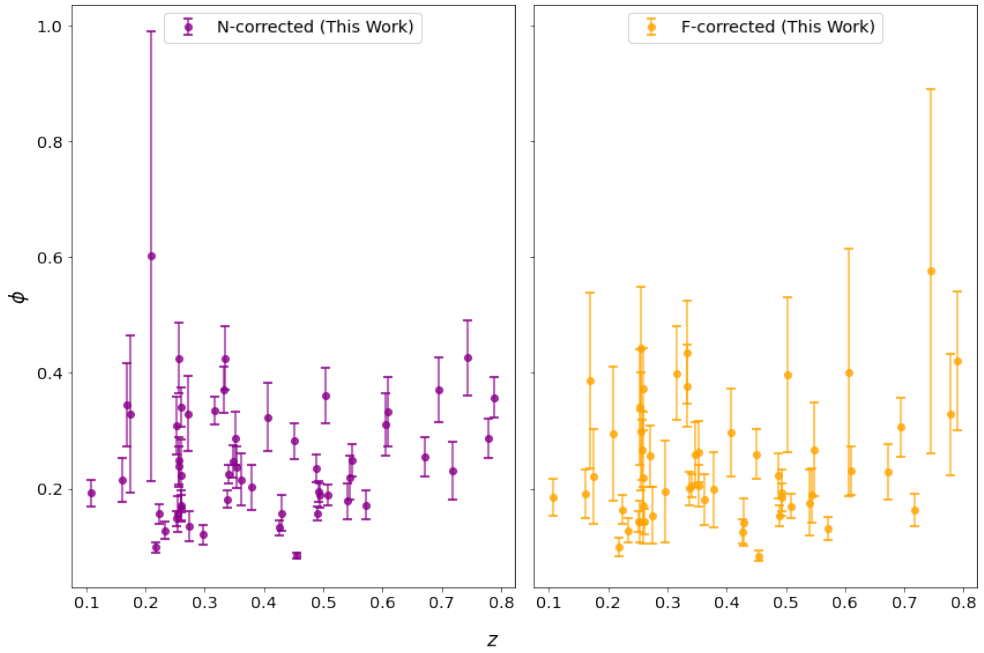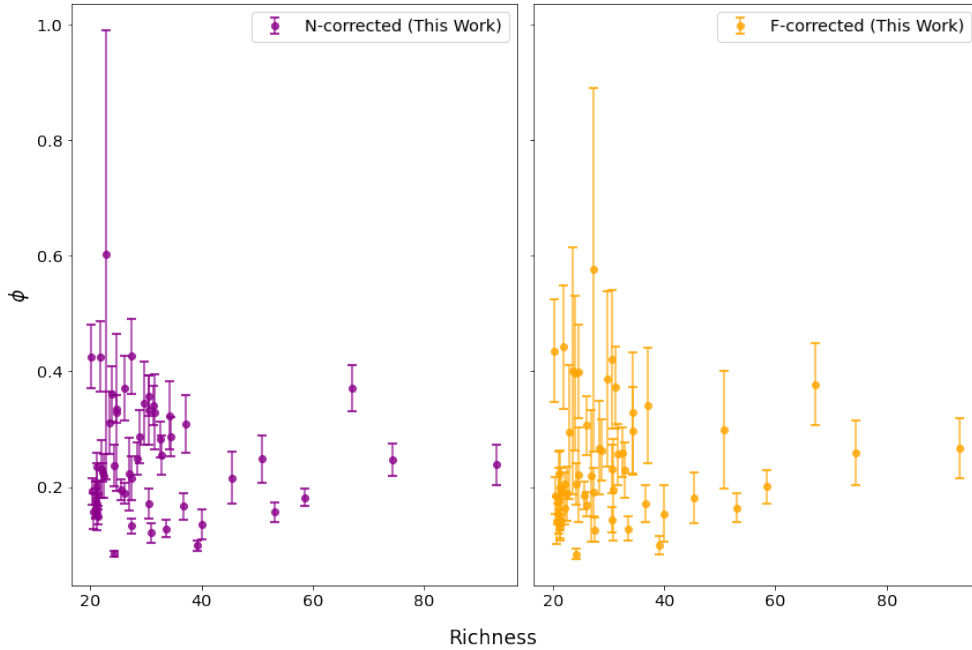
Figure 3.17: The ICL fraction of the CAMIRA-detected sample as a function of richness in the N-corrected case (left) and the F-corrected case (right). No correlation is exhibited in either case; if one assumes richness as a cluster mass proxy, this is in line with Figure 3.15 and the work of Furnell et al. (2021).

3.7 Discussion and Future Work

3.7.1 No Correlation Between ICL Fraction and z

In this work, we have measured convincing ICL profiles for many massive clusters (see Appendix A). Also, we have measured average membership-corrected and flux-corrected ICL fractions of 0.25 and 0.24, respectively, for 72 massive clusters across a redshift range of $0.1 \leq z \leq 0.8$, which agrees with those found in previous works (Jiménez-Teja et al., 2018; Kluge et al., 2021; Ragusa et al., 2021; Furnell et al., 2021).

We find no correlation between the ICL fraction and redshift (Figures 3.14 and 3.16), and our results for the XCS sample disagree with those of Furnell et al. (2021) (Figure 3.13). Theoretical works tend to associate higher ICL fractions with more dynamically evolved clusters, with the ICL being rapidly formed since redshift $z = 1$ (Martel et al., 2012; Contini et al., 2014; Murante et al., 2007). These support the idea that the ICL is formed mainly due to stellar stripping/destruction of galaxies from mergers both onto the BCG and between intermediate-sized satellites. However, these works adopt methods that are not observationally feasible (e.g. tracking the binding energies of stars

in cosmological simulations Murante et al., 2007), and so the observational results are less clear-cut as they use slightly varying definitions of the ICL.

There is disagreement in the literature as to whether the ICL shows significant growth in the redshift range covered in this work. One perspective from observational studies is that the bulk of the ICL is rapidly formed during the period $z = 1$ to present day. For example DeMaio et al. (2020) measured the ICL+BCG light of 42 clusters in the redshift range $z = 0.05$ to $z = 1.75$ and found that, for a fixed mass, the BCG+ICL flux grew within a physical radius of 100kpc by a factor of ~2 between $0.4 \lesssim z \lesssim 1.5$. However, below $z \sim 0.4$, they found no evidence for evolution. Here the authors defined the ICL as the residual light left over after masking all sources, with the masks defined by their `SExtractor`-constructed catalog semimajor and semiminor axis values beyond 7 arcseconds of the BCG, and by eye within 7 arcseconds of the BCG. Burke et al. (2015) used a sample of CLASH clusters to measure the ICL contribution over the redshift range $0.18 \leq z \leq 0.90$, by applying a surface brightness threshold of 25mag arcsec^{-2} in the *B*-band to define the ICL. They found that the ICL exhibited a growth by a factor of 4-5 in this redshift range. Furnell et al. (2021) used a similar method to measure the ICL of 18 XCS clusters in the redshift range $0.1 \leq z \leq 0.5$, using HSC *i*-band data, but had to modify their approach to tailor for the harsh background subtraction in divot corrections. The authors found a similar growth rate in the ICL fraction (2-4) in this redshift range, but noted that they found typically higher ICL fractions with redshift. They attributed their deviations to observational effects associated with differing *k*-corrections (Furnell et al. 2021 used data from a redder observational bandpass) and PSF sizes (Burke et al. 2015 used space-based data while HSC data is from ground-based observations).

On the other hand, other observational studies have found only a mild correlation, if any, between ICL fraction and redshift. Montes & Trujillo (2014) measured the ICL in 6 Hubble Frontier Fields galaxy clusters in the redshift range $0.3 < z < 0.6$. They used a surface brightness threshold of 26mag arcsec^{-2} in the *V*-band to define the ICL contribution, and found no clear correlation to the ICL growth with time. The same conclusion was reached by Guennou et al. (2012), who isolated the ICL of 10 HST ACS clusters in the redshift range $0.4 < z < 0.8$ in two bandpasses (HST/ACS F814W-band and VLT/FORS2 V-band). In this case, wavelet analysis was adopted, which is capable of separating large-scale (ICL) features from small-scale (sources) features. More recently, Golden-Marx et al. (2023) found a lack of evidence for evolution in the stellar mass of the ICL in massive clusters, over a redshift range of $0.2 \leq z \leq 0.8$. The authors used masking based on surface brightness thresholds to isolate the ICL, for their sample of DES-ACT clusters. These results are more consistent with the results presented in Figures 3.14 and 3.16; however, because of the various definitions used

to measure the ICL, along with all the observational considerations in each work, it is difficult to make direct comparisons and it is also impossible to say whether any one work is more credible than the rest. The disagreement in the literature highlights the need for a well-calibrated, deep survey of large numbers of clusters across a wide range of mass and redshift. This is exactly what *Euclid* will provide, and so follow-on work from Chapter 2 will offer a basis for a more accurate representation of the ICL in future studies.

Figure 3.13 shows that, prior to correction, our ICL fractions tend to be lower than those estimated in Furnell et al. (2021) (top plot in Figure 3.13). This suggests a systematic bias that propagates between the two works: it is quite possible that the divot corrections are over-estimating the flux lost from HSC PDR1's data processing pipeline. Even still, after we perform our correction to account for potential contaminant photometric galaxies in our cluster galaxy flux estimates, there does not appear to be a clear offset in our resultant ICL fractions and those from Furnell et al. (2021) (bottom two plots in Figure 3.13). If Furnell et al. (2021) used a similar way of assigning cluster membership to each galaxy as in this work, but did not make the corrections as done in this work, each cluster will have been subject to different levels of contamination, hence the inconsistently different ICL fractions. In order to make better comparisons between the two works, the ICL flux contribution, the cluster galaxy contribution and the constructed cluster-member source catalogs from Furnell et al. (2021) would be needed. Looking at the images in Figure 5 of Furnell et al. (2021) and in Figure A.1 of this work, it is difficult to ascertain whether the strength of masking is a factor in the discrepancies, since the former resembles a zoomed in ($0.4R_{500}$) version of each masked cluster. The BCG masks appears to be larger in the work of Furnell et al. (2021) - this may be due to the fact that we explicitly defined the BCG/ICL boundary by the *i*-band surface brightness threshold, instead of performing source detection and fitting the BCG as a Sérsic (Sérsic, 1963) or de Vaucouleurs profile, or designating the central 50kpc to the BCG (the authors used all three of these approaches to define the BCG).

3.7.2 No Correlation Between ICL Fraction and M_{500}/Richness

Figures 3.15 and 3.17 suggest a lack of a correlation between ICL fraction and cluster mass or richness respectively. From a theoretical standpoint, there is no clear agreement on whether a correlation should exist or not, for example: Murante et al. (2007) found that the fraction of the diffuse stellar component (i.e. the ICL) grew with increasing cluster mass in cosmological hydrodynamical simulations; Contini et al. (2014), on the other hand, found no correlation between ICL fraction and cluster mass in their simulations; Cui et al. (2014) even found that the ICL fraction exhibited an anti-correlation

with cluster mass. Many other theoretical works report a variety of findings (e.g. Purcell et al., 2007; Lin & Mohr, 2004; Dolag et al., 2010; Henriques & Thomas, 2010).

Observationally, most studies find there to be no correlation between ICL fraction and cluster mass or richness. Zibetti et al. (2005), for example, used data from SDSS-DR1 and found that, while the surface brightness of the ICL was higher in richer clusters between $z = 2$ and $z = 3$, the ICL fraction was insensitive to cluster richness. Sampaio-Santos et al. (2021) also found that the ICL fraction did not correlate with cluster mass in their sample of 528 DES clusters between $z = 0.2$ and $z = 0.35$. The same lack of correlation has been found by Furnell et al. (2021), which agrees with the results of this work (although the ICL fractions do not agree with each other in most cases). Although one might think that more massive halos give higher ICL fractions, it is actually the concentration (i.e. number of galaxies/mass of galaxies within a given radius) which is more important: in more concentrated clusters, the tidal interactions between galaxies are stronger and so there is much more stellar stripping (this has been demonstrated in simulations by Contini et al., 2014, see their Figure 3). This is why many studies of groups of galaxies reveal intragroup light (IGL) fractions that are comparable to ICL fractions of massive halos (e.g. Raj et al., 2020; Spavone et al., 2020; Ragusa et al., 2021). Therefore, it would make sense that any future studies should adopt a concentration parameter for groups/clusters when probing the ICL fraction dependence on cluster properties.

3.7.3 Future Work

At this moment of writing, we have two further analyses in mind that would make this study of the ICL more complete. One extension to this work is that we would like to repeat the process in different bands to compare the results and study colours (overall and gradients). Another analysis we would like to do is to fit the ICL radial profiles (Figures A.1 and A.2). This would enable us to quantify the extent of the ICL. Clearly, this would require that the clusters have detectable ICL, which, given the capability of the most recent surveys at this time of writing, we would expect a limit of $z \sim 1$.

3.8 Summary of Chapter

We have presented our measurements of the ICL from a sample of 72 galaxy clusters in the redshift range $0.1 \leq z \leq 0.8$, which were taken from a combination of: the XCS sample of 18 galaxy clusters used in Furnell et al. (2021); and a sample of 54 CAMIRA-detected galaxy clusters. We applied a method of masking and surface

brightness thresholding to isolate the ICL in HSC *i*-band images, allowing us to calculate their radial profiles, and we used spectroscopic and photometric data to assign cluster membership to galaxies, in order to estimate the ICL contribution to the total light of each cluster. We accounted for contaminant photometric cluster galaxies using a prescribed correction technique, which gave membership-corrected and flux-corrected photometric galaxy fluxes. We plotted our ICL fractions as functions of redshift and virial mass/cluster richness and compared with other studies to conclude the following:

- The ICL fractions we computed for the XCS sample of clusters did not align with those from Furnell et al. (2021), who used the same sample. We were unable to come up with definitive answers as to why this may be, as we are not sure how the authors assigned membership to cluster galaxies, or what the resultant fluxes were. We suspect that our correction technique, accounting for contaminant photometric galaxies, coupled with how we mask the central BCG in each cluster may make the largest contribution to these discrepancies (in the latter case, Furnell et al. 2021 fit profiles to the BCG to generate a mask, while we used segmentation data, obtained using a detection threshold of $B = 25$ mag arcsec^{-2}).

- We found no correlation between the ICL fraction and redshift. There is a disagreement in the current literature as to whether the ICL exhibits evolution in this redshift range: some other authors find a significant growth (e.g. Burke et al., 2015; DeMaio et al., 2020; Furnell et al., 2021), while other authors have found the same lack of correlation as in this work (e.g. Guennou et al., 2012; Montes & Trujillo, 2014; Golden-Marx et al., 2023). This disagreement can be accredited to the inconsistent definition of the ICL used in each case, highlighting the need for a single, unified definition of the ICL in order to make better comparisons.

- We found no correlation between the ICL fraction and cluster mass/richness. This is in agreement with what is commonly found in ICL studies (e.g. Zibetti et al., 2005; Sampaio-Santos et al., 2021; Furnell et al., 2021); we have discussed how a cluster concentration proxy would more likely reveal a positive correlation with the ICL fraction, since tidal stripping events occur more frequently between satellite galaxies in regions containing more galaxies, rather than in generally more massive clusters.

Our work presented here is not complete, as we have further analyses in mind. These are: studying the ICL in different bandpasses to compare the results in each band and study colours (overall and gradients); and fitting the ICL radial profiles to quantify the extent of the ICL in different clusters.

As already mentioned, there remains a significant issue with modern studies, in that the ICL is ill-defined. Therefore, even with the advent of the most cutting-edge surveys with the most intricate reduction pipelines (e.g. at this time of writing, JWST and Euclid have begun their missions), studies will always be limited until a solid definition has been established.

Chapter 4

Fitting ICL (*ficl*): A New Automated Code to Measure the ICL in Multiple Clusters

This Chapter forms the final piece of my thesis, and represents the work I began at the start of my journey at the University of Nottingham. The work discussed here is yet to be completed (I could not finish the project due to personal problems I faced during my time at Nottingham) but, when finished, will offer a new, robust method of disentangling the ICL from clusters of galaxies.

4.1 Overview

We have chosen to combine the advantages of surface brightness thresholding, profile fitting and wavelet filtering in a hybrid approach, providing the required combination of accuracy, robustness and computational efficiency. We first mask the brightest pixels that belong to the central regions of galaxies containing excess nuclear light, which may otherwise influence the fitting aspect of our method (this removes the need to include an additional central component to the galaxy light profiles, as discussed in Section 2.3 in Graham, 2013). The image is de-noised using wavelet filtering, which is capable of identifying surface-brightness features on given scales. Then, any remaining compact sources or high-surface-brightness galaxy features (nuclei, spiral arms, etc.) are assigned to a small-scale "non-parametric" component via an iterative combination of profile fitting and wavelet filtering. The influence of the ICL on the fitted galaxy profiles is also ameliorated by another large-scale "non-parametric" component. The

resulting parametric, single component, Sérsic (Sérsic, 1963) models can be used to subtract the remaining, smooth, galaxy light.

Our method separates the original image out into three images: the small-scale features that belong to the galaxies; the smooth, Sérsic models of each galaxy; and the ICL. The ICL image derived using `ficl` is smooth, giving a much higher SNR than the ICL derived from the method used in the previous Chapter (see Figures A.1 and A.2, the masks present in the images can dramatically reduce the ICL signal). This offers a 3D interpretation of the ICL, rather than a 1D radial profile that is constructed using mean values of unmasked pixels in elliptical annuli, which allows for much more complicated analyses of the ICL to be performed (e.g. the ICL as a dark matter tracer in clusters, as found by Montes & Trujillo, 2019). Furthermore, because we do not make any strong assumptions about the ICL in `ficl`, our results are much more representative of the true ICL in clusters - surface brightness thresholding and profile fitting approaches, on their own, make significant assumptions about the brightness and shape of the ICL.

A flow-chart is given in Figure 4.1, showing the workings of our code. In the following, I discuss our progress to date with `ficl`.
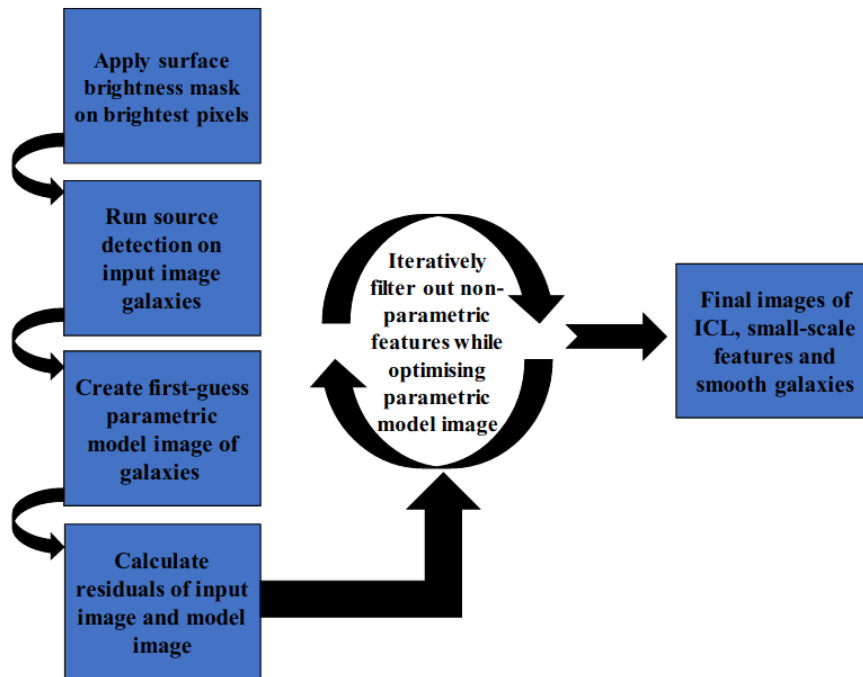

Figure 4.1: Simple flow diagram of our ICL extraction method.

4.2 Source detection, Profile fitting and Filtering

After a sensible surface brightness mask is applied, we perform source detection using `photutils` (Bradley et al., 2016), which is essentially a pythonic version of `SExtractor` (Bertin & Arnouts, 1996). `photutils` detects sources using image segmentation: pixels that have values greater than a chosen multiple of sigmas above the background level are assigned to a source. For overlapping sources, `photutils` also performs deblending[1]. Then, `photutils` produces a source catalog – we compare and calibrate the measured parameters against the true parameters from a simulated cluster image (simulated in a similar fashion to Chapter 2, only this time retaining the BCG parameters from the lightcone for simplicity). The source catalog does not include estimates for the half-light radius or the Sérsic index (n, Sérsic, 1963) for each source. It does, however, provide an estimate of the Kron radius (r_k, Kron, 1980), and `photutils` can estimate the flux within a given number of r_k. Therefore, we measure the flux between $0.2r_k$ and $2.5r_k$ in small increments (the latter value here is deemed an appropriate measure of the total flux of the source, as shown by Graham & Driver, 2005), and interpolate to find the radius that encapsulates half of the total flux - this provides an estimate of the half-light radii. For the Sérsic indices, we just adopt a value of $n = 2$ for every source, since this will be converted into a more accurate value for each galaxy during the fitting process.

With the parameters in the source catalog, we create a model image – simulated using `GalSim` (Rowe et al., 2015) – and subtract this from the original image to obtain a residual image. We then begin the iterative fitting+filtering process: in parallel to optimising each parameter (i.e. minimising the χ^2s), we filter out the large-scale (ICL) and small-scale (nuclei, spiral arms, star-forming regions...) features that may serve to influence the fitting process, at given optimisation steps. We use a gradient descent method for our optimisation algorithm. For this, we are currently calculating the derivatives of χ^2 for each parameter manually; however, we are in the process of developing an automatic differentiation tool using `jax` (Frostig et al., 2018).

We use `PyWavelets` (Lee et al., 2019) to perform wavelet filtering on the small-scale features, and we use a Gaussian-smoothed median filter for the ICL[2] (note, filtering is performed on the residuals at specified iterations during optimisation). Therefore, we iteratively filter out these non-parametric features and deposit them onto separate, initially empty, "non-parametric images". Meanwhile, the fitting of the remaining, smooth galaxies in the 'working image' is more accurate as it is not influenced by these features. The end product: a non-parametric image containing the small-scale features, a

---

[1]The full documentation can be found at `https://photutils.readthedocs.io/en/stable/index.html`.

[2]We are also investigating wavelet-filter approaches

parametric image containing the smooth galaxy models, and a non-parametric image containing our desired ICL.

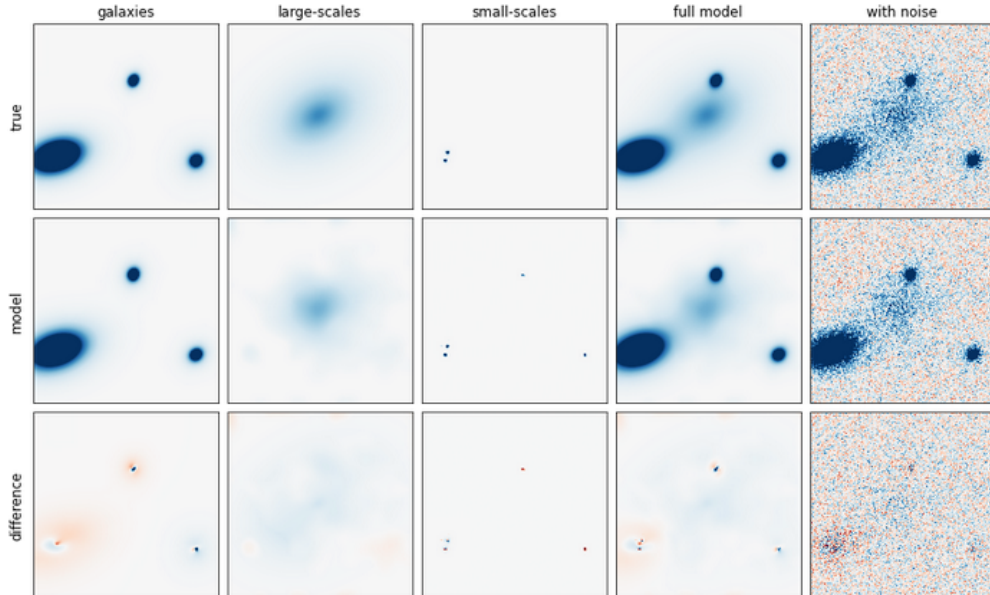## 4.3 Proof-of-concept results

Figure 4.2: Results of our ICL extraction algorithm from a simple toy-model run. This model contains: three simple galaxies (one of which has two star-forming regions) and an overlaid ICL component. The top row shows all of the originally simulated components, the second row shows the resulting model for each component from our algorithm, and the bottom row shows the residuals.

We simulated a simple image containing three galaxies, one of which contained two star-forming regions, and an ICL component. We added a constant background sky-level and added Poisson and CCD noise using the readout noise of *Euclid*'s VIS instrument. We also convolved each profile with a numerical model of *Euclid*'s PSF. The reason we chose to do this is because we wanted to eventually use our method on realistic *Euclid* simulations, so that we could compete against other methods in the ICL working group. The results from our ICL extraction method on this toy model are shown in Figure 4.2.

In Figure 4.2, the star-forming regions from the original model (middle panel of the top row) have been identified by our method (middle panel of the second row). In addition to this, our method has filtered out the central regions of the other two galaxies. Meanwhile, the residuals of the smooth galaxy profiles (left panel of bottom row) are small, showing that the fitting aspect has been reasonably successful. The final ICL profile that our method extracts (second panel of middle row) contains around 60% of

the original ICL profile's flux. This is promising, as we can see that the method is certainly doing as we expected. However, we still have a lot of work to do to get our method working on a full, realistically simulated image.

4.4 Summary and Future Work

In this brief Chapter, I have outlined progress made to date on developing `ficl`, which is an automated ICL fitting code. This method makes use of aspects from three existing techniques: surface brightness thresholding, profile fitting and wavelets. The first two of these methods are based on strong assumptions about the ICL, while the latter struggles to separate the ICL from clusters with galaxies of a similar size to the ICL. However, when used in tandem, we have shown that the ICL can be successfully extracted from clusters with no strong assumptions about the ICL, even if the ICL is of a similar scale to the galaxies.

At current, this method is still in progress. We still need to add in the element of wavelets as, at the moment, we are using median-filtering. Once this has been incorporated into `ficl`, the testing phase can begin, which will allow for further refinements and optimisation. In parallel with this, we are in the process of speeding up the fitting part of `ficl`, by automatically differentiating the gradients in gradient descent, using `jax` (Frostig et al., 2018). This will require a lesser computational demand, and, by making use of GPUs, we can speed up the computations.

To test `ficl`, we will apply it to a variety of simulated images. Firstly, we will apply it to simple images that we simulate using lightcone data (as described in Chapter 2), then we hope to access hydrosimulations of clusters (e.g. C-EAGLE; Barnes et al., 2017). We will also compare `ficl` with more traditional approaches, as applied in Chapter 3. We will hopefully prove from this that we can recover a high proportion of the ICL that was contained within these models. This testing is currently being performed in the *Euclid* ICL group, using descendants of the simulations outlined in Chapter 2. We can then look at applying `ficl` to observational data, where we can make measurements of ICL colours, study the dynamical properties of ICL, compare radial profiles versus other techniques (such as in the previous chapter), and also enable a more systematic study of the 2D spatial structure of the ICL. For this, we will have access to data from some of the most cutting-edge surveys, such as *Euclid*, LSST and JWST.

Chapter 5

Conclusions and Future Work

This work has been concerned with the challenges of simulating and measuring ICL. We have: devised a simple way of simulating realistic ICL, using data lightcone data, which is beneficial for testing methods that measure the ICL; used a surface brightness thresholding method to analyse the ICL in a sample of 72 galaxy clusters in the redshift range $0.1 \leq z \leq 0.8$; and introduced a new code that isolates the ICL, which will be robust against other traditional methods. A summary of each of these elements to this work will be given in the following.

5.1   Simulating Realistic ICL

Using data from the Millennium MAMBO lightcone, we simulated images of clusters that contain ICL (Chapter 2). The lightcone is constructed based on the full dark-matter Millennium simulation (Springel et al., 2005), using semi-analytical models of galaxy formation from Henriques et al. (2015), consisting of realistic galaxy properties from the Empirical Galaxy Generator (EGG; Schreiber et al., 2017). We used *Euclid* instrumentation to generate our images, since I was a part of *Euclid*'s ICL science working group at the time and we ultimately wanted to test our ICL codes.

We modelled galaxies from this lightcone as bulge+disk Sérsic profiles (Sérsic, 1963). In the case of the Brightest Cluster Galaxy, we assumed a single-component Sérsic profile, with the Sérsic index and effective radius taken from observational data (see Appendix **??**) and the ellipticity and orientation being estimated from principle component analysis of the cluster member galaxies (the cluster tends to have a roughly similar shape to the ICL and BCG, Kluge, 2019). A similar process was used to define the ICL parameters, and we varied the ICL fraction, shape and offset from the cluster to generate 18 cluster images. These images were added to a field image that was gener-

ated and processed using *Euclid*'s pipeline. The 18 images were distributed amongst members of *Euclid*'s ICL science working group so that they could test their ICL codes in preparation for data from the upcoming *Euclid* survey.

Upon receiving results from the group, it was discovered that the measured ICL profiles had unusual dips in flux, which were not implemented in the simulated ICL images. Closer inspection revealed that the background mosaic had a patchy background due to a harsh background subtraction. Figure 2.9, provided by C. Bellhouse, explicitly shows a significant loss in the ICL signal when using *Euclid*'s standard reduction pipeline to process raw data. This is common in surveys, particularly for those with pipelines that are not optimised for studies of extended, low surface brightness features. Therefore, any further work was suspended until this issue could be resolved. An alternative background estimator in *Euclid*'s pipeline should be used for ICL science – `NoiseChisel` (Akhlaghi & Ichikawa, 2015; Akhlaghi, 2019) seems particularly promising for this task as it is optimised for processing images that are used to study faint, extended sources. The galaxy evolution and ICL groups of *Euclid* are currently working on an alternative for ICL studies.

5.2 Measuring the ICL by Applying a SB-Threshold

In a similar fashion to previous works (e.g. Burke et al., 2015; Furnell et al., 2021), we applied a combination of surface brightness thresholding and masking to a sample of 72 clusters, using HSC *i*-band data in the redshift range $0.1 \leq z \leq 0.8$ (Chapter 3). The sample consisted of two subsets: the same XCS sample of 18 clusters used in Furnell et al. (2021) and a sample of 54 clusters that were detected using the CAMIRA algorithm (Oguri et al., 2018). We used data from the most recent release of the HSC Subaru Strategic Program (PDR3), an improvement from previous releases as it was processed in a way which was optimal for faint, extended sources (removing the element of 'divots', which had to be accounted for in Furnell et al., 2021). As well as this, we explicitly provided a simple way of estimating the total flux from cluster members, while accounting for potential contaminant photometric cluster galaxies (these arise due to the large uncertainties associated with photo-*z*s).

Our method begins by masking bad pixels and the brightest objects in the frame, which utilises the HSC mask data. We do not simply use the HSC mask image for halo masks, as these include 'dip' features that are often too large. Therefore, we remove these constant-sized masks and double the halo masks to blank out stellar halos from our ICL estimates. We then run a 3σ object detection and use the segmentation data to mask sources in the image. Beneath the blanket of the ICL remains many fainter sources (e.g.

globular clusters or small satellites), so we generate a mask for these by first removing the ICL using a harsh background subtraction, running a 2σ source detection and then using the resulting segmentation data. The BCG is not included in any of these mask layers as we use an isophotal threshold of 25mag arcsec^{-2} (as in Burke et al., 2015; Furnell et al., 2021) to define the BCG/ICL boundary: we perform source detection at the position of the BCG using this threshold, and mask using the resulting segmentation data.

With our masked images, we measure the unmasked pixels as the ICL flux. To account for regions with no data (masked regions), we extrapolate data from nested elliptical annuli that resemble the shape of the ICL, which were estimated using principle component analysis of the unmasked pixels in the central $0.4R_{500}$ region of the image. Thus, we obtain a radial profile for each cluster, and this is integrated to give the total ICL flux.

We use photometric and spectroscopic data from catalogs of sources in each of the HSC deep fields to assign cluster membership within apertures of R_{500}. For spectroscopic data, we define members as those with z_{spec}s that fall within a $3\sigma_v$ slice of the cluster, adopting a typical cluster velocity dispersion of $3\sigma_v = 3000$kms^{-1}. For sources with only photometric data, we use the typical error on photo-zs from the code DEmP (Hsieh & Yee, 2014) to ascertain whether it is possible that, within 3σ, the source could be a cluster member. We sum the fluxes from the potential photo-z members and apply a background-level correction, which estimates the typical membership of field galaxies to a cluster at z_{cl} within an aperture of R_{500}, accounting for potential contaminant photo-z members. This provides two different estimates: corrected using total fluxes within background apertures and corrected using membership to each aperture. We then calculate the ICL fractions using these corrected values, the fluxes from the spectroscopic members and the ICL flux.

Our ICL fractions for the XCS sample did not match those of Furnell et al. (2021), with no consistent offset exhibited that would give a reasonable explanation. A couple of possible causes may be that: we masked the BCG using segmentation data, defined by the isophotal threshold, whereas Furnell et al. (2021) used profile-fitting to mask the BCGs; and we applied a background correction to our photometric cluster member flux, while Furnell et al. (2021) did not (as far as we know).

When plotting all of the ICL fractions against redshift, no correlation was found, disagreeing with various other authors (e.g. Burke et al., 2015; DeMaio et al., 2020; Furnell et al., 2021). However, this is not the only work to output a lack of evidence for ICL growth over time, as Guennou et al. (2012) and Montes & Trujillo (2014) came to the same conclusion when using clusters in the redshift range $0.3 \leq z \leq 0.8$. The lack of consistency between works is perhaps mostly due to the ill-defined ICL, with some

authors using surface brightness thresholds (e.g. Montes & Trujillo, 2014; Burke et al., 2015; Furnell et al., 2021, note that the value used for the threshold in the first work here was different to the other two), wavelet analysis (e.g. Adami et al., 2005; Guennou et al., 2012; Ellien et al., 2021), or profile-fitting (e.g. Gonzalez et al., 2005; Zhang et al., 2019; Kluge et al., 2021; Montes et al., 2021).

Our sample of clusters' ICL fractions did not correlate with cluster mass/richness either, a result which is commonly found in ICL studies (e.g. Zibetti et al., 2005; Sampaio-Santos et al., 2021; Furnell et al., 2021). This is likely due to the fact that the concentration of galaxies in the cluster, an important factor in the process of tidal stripping and forming the ICL, has little dependence on the total cluster mass. Therefore, one may wish to explore this further by defining a concentration parameter for groups/clusters, and plotting the ICL fraction dependence.

5.3 A New Code to Measure the ICL: ficl

The inconsistent results among works in ICL studies are largely due to the lack of grounding for a 'well-defined' ICL. We have, therefore, set out to address this issue by outlining a new code for isolating and measuring the ICL (Chapter 4), which makes no major prior assumptions that may compromise results. `ficl` combines the best aspects of the three major ICL detection methods (surface brightness thresholding, profile fitting and wavelet analysis) in a hybrid, fast (using jax-based implementation Frostig et al., 2018) automated approach. Upon completion, we will make `ficl` an open-source user-friendly software, with applications even beyond ICL studies (e.g. it will also provide a new, powerful code for galaxy profile-fitting).

Firstly, the brightest pixels are masked, as these can influence the profiles that we fit to sources in an image. Then, we detect and deblend sources using `photutils` (Bradley et al., 2016) and construct a catalog of detected sources. An initial model image is constructed using the parameters and the residuals are calculated. After this, an iterative fitting and filtering process commences: while the parameters are optimised in gradient descent, large-scale (ICL) and small-scale (nuclei, spiral arms, star-forming regions etc.) features are slowly pulled out of the working image, which increasingly improves the fitting process.

Once complete, the original image is separated out into images of the fitted galaxy profiles, the small-scale features and the ICL. The ICL image that is produced in `ficl` is smooth, unlike the ICL from simple masking methods, and so may be interpreted in three dimensions without extrapolating pixels in masked regions. Because we do not make any prior assumptions about the shape and/or profile of the ICL or the BCG (as

one does in purely fitting methods), we get a more accurate picture of the ICL too. This method is more powerful than those which are purely based on wavelets because we remove the difficulty of separating out the ICL and large central galaxies, which may become otherwise confused with each other.

We have used an unfinished version of `ficl` on a simple toy model, as a proof of concept. This has proved that we are already able to successfully output the three images of galaxy profiles, small-scale features and ICL, with a recovered ICL signal of 60% of the input. However, this version of `ficl` is yet to have the wavelet component implemented, since this is one of the more intricate elements to the code. We are confident that, after implementing wavelets, testing our code and subsequently optimising, `ficl` will offer an unbiased, accurate view of the ICL, which will revolutionise the field.

5.4   Future Work

The work presented in this thesis is by no means complete, and we will build on the latter two chapters in particular.

In Chapter 3, while we obtained radial profiles of each cluster's ICL, we did not perform any further analysis on them. We aim to fit the profiles to quantify the extent of the ICL, for clusters out to a redshift of $z \sim 0.1$ (provided the clusters have measurable ICL). Furthermore, we would like to make measurements in multiple bandpasses, so that we can compare the results in each band and study the colours of the ICL (overall colours and colour gradients).

As already mentioned, our work in Chapter 4 is due to be completed, as it requires implementation of wavelets and testing and optimisation. Once `ficl` is up and running, we will test our algorithm on simulated images (data from both lightcones, as in Chapter 2, and hydrosimulations, e.g. Barnes et al., 2017) and then observational data. We will compare our method against other present methods (for example, Chapter 3 and DAWIS Ellien et al., 2021), and we will show that `ficl` is both computationally efficient and more accurate than the other codes. We will offer `ficl` as an open-source, user-friendly program, which will set the stage for more intricate studies of the ICL.

The dawn of new simulations dedicated to accurately modelling the processes in clusters, together with data from the most cutting-edge surveys (such as JWST, *Euclid* and LSST), which will allow the ICL to be probed in many thousands of clusters, spanning wide ranges in mass and redshift, gives an exciting outlook on advances in our understanding of the ICL over the next few years.

Bibliography

Adami C., et al., 2005, A&A, 429, 39

Aguerri J. A. L., Castro-Rodríguez N., Napolitano N., Arnaboldi M., Gerhard O., 2006, A&A, 457, 771

Ahumada R., et al., 2020, ApJS, 249, 3

Aihara H., et al., 2011, ApJS, 193, 29

Aihara H., et al., 2018a, PASJ, 70, S4

Aihara H., et al., 2018b, PASJ, 70, S8

Aihara H., et al., 2019, PASJ, 71, 114

Aihara H., et al., 2022, PASJ, 74, 247

Akhlaghi M., 2019, arXiv e-prints, p. arXiv:1909.11230

Akhlaghi M., Ichikawa T., 2015, ApJS, 220, 1

Albareti F. D., et al., 2017, ApJS, 233, 25

Alonso Asensio I., Dalla Vecchia C., Bahé Y. M., Barnes D. J., Kay S. T., 2020, MNRAS, 494, 1859

Arnaboldi M., et al., 1996, ApJ, 472, 145

Arnaboldi M., Ventimiglia G., Iodice E., Gerhard O., Coccato L., 2012, A&A, 545, A37

Arp H., Bertola F., 1969, Astrophys. Lett., 4, 23

Bahé Y. M., McCarthy I. G., Balogh M. L., Font A. S., 2013, MNRAS, 430, 3017

Barnes D. J., et al., 2017, MNRAS, 471, 1088

Baum W. A., 1959, PASP, 71, 106

Bayliss M. B., Hennawi J. F., Gladders M. D., Koester B. P., Sharon K., Dahle H., Oguri M., 2011, ApJS, 193, 8

Bayliss M. B., Johnson T., Gladders M. D., Sharon K., Oguri M., 2014, ApJ, 783, 41

Beers T. C., Flynn K., Gebhardt K., 1990, AJ, 100, 32

Bernardi M., Fischer J. L., Sheth R. K., Meert A., Huertas-Company M., Shankar F., Vikram V., 2017, MNRAS, 468, 2569

Bernstein G. M., Nichol R. C., Tyson J. A., Ulmer M. P., Wittman D., 1995, AJ, 110, 1507

Bertin E., Arnouts S., 1996, A&AS, 117, 393

Blakeslee J. P., 1999, AJ, 118, 1506

Bosch J., et al., 2018, PASJ, 70, S5

Bradley L., et al., 2016, Photutils: Photometry tools, Astrophysics Source Code Library, record ascl:1609.011 (ascl:1609.011)

Bradshaw E. J., et al., 2013, MNRAS, 433, 194

Bruzual G., Charlot S., 2003, MNRAS, 344, 1000

Burke C., Hilton M., Collins C., 2015, MNRAS, 449, 2353

Cavagnolo K. W., Donahue M., Voit G. M., Sun M., 2009, ApJS, 182, 12

Chabrier G., 2003, PASP, 115, 763

Chun K., Shin J., Smith R., Ko J., Yoo J., 2022, ApJ, 925, 103

Coil A. L., et al., 2011, ApJ, 741, 8

Colless M., et al., 2003, arXiv e-prints, pp astro–ph/0306581

Collins C. A., et al., 2009, Nature, 458, 603

Contigiani O., Vardanyan V., Silvestri A., 2019, Phys. Rev. D, 99, 064030

Contini E., De Lucia G., Villalobos Á., Borgani S., 2014, MNRAS, 437, 3787

Contini E., Yi S. K., Kang X., 2018, MNRAS, 479, 932

Contini E., Yi S. K., Kang X., 2019, ApJ, 871, 24

Cool R. J., et al., 2013, ApJ, 767, 118

Cooper M. C., et al., 2011, ApJS, 193, 14

Cooper M. C., et al., 2012, MNRAS, 419, 3018

Cui W., et al., 2014, MNRAS, 437, 816

Da Rocha C., Ziegler B. L., Mendes de Oliveira C., 2008, MNRAS, 388, 1433

Davis M., et al., 2003, in Guhathakurta P., ed., Society of Photo-Optical Instrumentation Engineers (SPIE) Conference Series Vol. 4834, Discoveries and Research Prospects from 6- to 10-Meter-Class Telescopes II. pp 161–172 (`arXiv:astro-ph/0209419`), doi:10.1117/12.457897

De Lucia G., Blaizot J., 2007, MNRAS, 375, 2

DeMaio T., Gonzalez A. H., Zabludoff A., Zaritsky D., Connor T., Donahue M., Mulchaey J. S., 2018, MNRAS, 474, 3009

DeMaio T., et al., 2020, MNRAS, 491, 3751

Deason A. J., et al., 2021, MNRAS, 500, 4181

Di Matteo P., Pipino A., Lehnert M. D., Combes F., Semelin B., 2009, A&A, 499, 427

Dolag K., Murante G., Borgani S., 2010, MNRAS, 405, 1544

Drinkwater M. J., et al., 2010, MNRAS, 401, 1429

Dubinski J., 1998, ApJ, 502, 141

Duc P.-A., et al., 2015, MNRAS, 446, 120

Edwards L. O. V., Alpert H. S., Trierweiler I. L., Abraham T., Beizer V. G., 2016, MNRAS, 461, 230

Eigenthaler P., Zeilinger W. W., 2013, A&A, 553, A99

Ellien A., et al., 2021, A&A, 649, A38

Feldmeier J. J., Mihos J. C., Morrison H. L., Harding P., Kaib N., Dubinski J., 2004, ApJ, 609, 617

Frostig R., Johnson M., Leary C., 2018. `https://mlsys.org/Conferences/doc/2018/146.pdf`

Furnell K. E., et al., 2021, MNRAS, 502, 2419

Gaia Collaboration et al., 2018, A&A, 616, A1

Garilli B., et al., 2014, A&A, 562, A23

Giallongo E., Menci N., Grazian A., Fassbender R., Fontana A., Paris D., Pentericci L., 2015, ApJ, 813, 68

Golden-Marx J. B., et al., 2023, MNRAS, 521, 478

Gonzalez A. H., Zabludoff A. I., Zaritsky D., 2005, ApJ, 618, 195

Gonzalez A. H., George T., Connor T., Deason A., Donahue M., Montes M., Zabludoff A. I., Zaritsky D., 2021, MNRAS, 507, 963

Graham A. W., 2013, in Oswalt T. D., Keel W. C., eds, , Vol. 6, Planets, Stars and Stellar Systems: Extragalactic Astronomy and Cosmology. p. 91

Graham A. W., Driver S. P., 2005, PASA, 22, 118

Gu M., et al., 2020, ApJ, 894, 32

Guennou L., et al., 2012, A&A, 537, A64

Guzzo L., et al., 2014, A&A, 566, A108

Hasinger G., et al., 2018, ApJ, 858, 77

Hatch N. A., Overzier R. A., Röttgering H. J. A., Kurk J. D., Miley G. K., 2008, MNRAS, 383, 931

Henriques B. M. B., Thomas P. A., 2010, MNRAS, 403, 768

Henriques B. M. B., White S. D. M., Thomas P. A., Angulo R., Guo Q., Lemson G., Springel V., Overzier R., 2015, MNRAS, 451, 2663

Hsieh B. C., Yee H. K. C., 2014, ApJ, 792, 102

Huang S., Leauthaud A., Greene J. E., Bundy K., Lin Y.-T., Tanaka M., Miyazaki S., Komiyama Y., 2018, MNRAS, 475, 3348

Iodice E., et al., 2017, ApJ, 851, 75

Jiménez-Teja Y., et al., 2018, ApJ, 857, 79

Jiménez-Teja Y., et al., 2019, A&A, 622, A183

Jones D. H., et al., 2004, MNRAS, 355, 747

Jones D. H., et al., 2009, MNRAS, 399, 683

Kennedy R., et al., 2016, MNRAS, 460, 3458

Kluge M., 2019, in Light in the Suburbs: Structure and Chemodynamics of Galaxy Halos. p. 9

Kluge M., et al., 2020, ApJS, 247, 43

Kluge M., Bender R., Riffeser A., Goessl C., Hopp U., Schmidt M., Ries C., 2021, ApJS, 252, 27

Krick J. E., Bernstein R. A., 2007, AJ, 134, 466

Krick J. E., Glaccum W. J., Carey S. J., Lowrance P. J., Surace J. A., Ingalls J. G., Hora J. L., Reach W. T., 2012, ApJ, 754, 53

Kron R. G., 1980, ApJS, 43, 305

La Barbera F., Ferreras I., de Carvalho R. R., Bruzual G., Charlot S., Pasquali A., Merlin E., 2012, MNRAS, 426, 2300

Laporte C. F. P., White S. D. M., Naab T., Gao L., 2013, MNRAS, 435, 901

Le Fèvre O., et al., 2013, A&A, 559, A14

Lee G., Gommers R., Waselewski F., Wohlfahrt K., O'Leary A., 2019, The Journal of Open Source Software, 4, 1237

Lee M. G., Bae J. H., Jang I. S., 2022, ApJ, 940, L19

Lidman C., et al., 2012, MNRAS, 427, 550

Lidman C., et al., 2013, MNRAS, 433, 825

Lilly S. J., et al., 2009, ApJS, 184, 218

Lin Y.-T., Mohr J. J., 2004, ApJ, 617, 879

Liske J., et al., 2015, MNRAS, 452, 2087

Longobardi A., Arnaboldi M., Gerhard O., Pulsoni C., Söldner-Rembold I., 2018, A&A, 620, A111

Mancone C. L., Gonzalez A. H., 2012, PASP, 124, 606

Martel H., Barai P., Brito W., 2012, ApJ, 757, 48

Masters D. C., Stern D. K., Cohen J. G., Capak P. L., Rhodes J. D., Castander F. J., Paltani S., 2017, ApJ, 841, 111

Masters D. C., et al., 2019, ApJ, 877, 81

Matthews T. A., Morgan W. W., Schmidt M., 1964, ApJ, 140, 35

Mattila K., 1977, A&A, 60, 425

McLure R. J., et al., 2013, MNRAS, 428, 1088

Mehrtens N., et al., 2012, MNRAS, 423, 1024

Melnick J., White S. D. M., Hoessel J., 1977, MNRAS, 180, 207

Melnick J., Giraud E., Toledo I., Selman F., Quintana H., 2012, MNRAS, 427, 850

Mihos J. C., Harding P., Feldmeier J., Morrison H., 2005, ApJ, 631, L41

Miyazaki S., et al., 2018, PASJ, 70, S1

Mohammed I., Saha P., Williams L. L. R., Liesenborgs J., Sebesta K., 2016, MNRAS, 459, 1698

Momcheva I. G., et al., 2016, ApJS, 225, 27

Montes M., 2022, Nature Astronomy, 6, 308

Montes M., Trujillo I., 2014, ApJ, 794, 137

Montes M., Trujillo I., 2018, MNRAS, 474, 917

Montes M., Trujillo I., 2019, MNRAS, 482, 2838

Montes M., Brough S., Owers M. S., Santucci G., 2021, ApJ, 910, 45

Murante G., et al., 2004, ApJ, 607, L83

Murante G., Giovalli M., Gerhard O., Arnaboldi M., Borgani S., Dolag K., 2007, MNRAS, 377, 2

Navarro J. F., Frenk C. S., White S. D. M., 1996, ApJ, 462, 563

Navarro J. F., Frenk C. S., White S. D. M., 1997, ApJ, 490, 493

Neto A. F., et al., 2007, MNRAS, 381, 1450

Newman J. A., et al., 2013, ApJS, 208, 5

Oemler A., 1973, ApJ, 180, 11

Oguri M., 2014, MNRAS, 444, 147

Oguri M., Bayliss M. B., Dahle H., Sharon K., Gladders M. D., Natarajan P., Hennawi J. F., Koester B. P., 2012, MNRAS, 420, 3213

Oguri M., et al., 2018, PASJ, 70, S20

Pâris I., et al., 2018, A&A, 613, A51

Peng E. W., et al., 2011, ApJ, 730, 23

Pentericci L., et al., 2018, A&A, 616, A174

Piffaretti R., Arnaud M., Pratt G. W., Pointecouteau E., Melin J. B., 2011, A&A, 534, A109

Presotto V., et al., 2014, A&A, 565, A126

Puchwein E., Springel V., Sijacki D., Dolag K., 2010, MNRAS, 406, 936

Purcell C. W., Bullock J. S., Zentner A. R., 2007, ApJ, 666, 20

Ragusa R., et al., 2021, A&A, 651, A39

Raj M. A., et al., 2020, A&A, 640, A137

Romer A. K., Viana P. T. P., Liddle A. R., Mann R. G., 2001, ApJ, 547, 594

Rowe B. T. P., et al., 2015, Astronomy and Computing, 10, 121

Rudick C. S., Mihos J. C., McBride C., 2006, ApJ, 648, 936

Rudick C. S., Mihos J. C., Frey L. H., McBride C. K., 2009, ApJ, 699, 1518

Rudick C. S., Mihos J. C., Harding P., Feldmeier J. J., Janowiecki S., Morrison H. L., 2010, ApJ, 720, 569

Rudick C. S., Mihos J. C., McBride C. K., 2011, ApJ, 732, 48

Sampaio-Santos H., et al., 2021, MNRAS, 501, 1300

Schreiber C., et al., 2017, A&A, 602, A96

Seigar M. S., Graham A. W., Jerjen H., 2007, MNRAS, 378, 1575

Sérsic J. L., 1963, Boletin de la Asociacion Argentina de Astronomia La Plata Argentina, 6, 41

Silverman J. D., et al., 2015, ApJS, 220, 12

Singhal A., et al., 2021, MNRAS, 507, 4983

Skelton R. E., et al., 2014, ApJS, 214, 24

Slezak E., Durret F., Gerbal D., 1994, AJ, 108, 1996

Sommer-Larsen J., Romeo A. D., Portinari L., 2005, MNRAS, 357, 478

Spavone M., et al., 2020, A&A, 639, A14

Springel V., et al., 2005, Nature, 435, 629

Straatman C. M. S., et al., 2018, ApJS, 239, 27

Struble M. F., Rood H. J., 1999, ApJS, 125, 35

Tanaka M., et al., 2018, PASJ, 70, S9

Thuan T. X., Kormendy J., 1977, PASP, 89, 466

Trujillo I., Ferreras I., de La Rosa I. G., 2011, MNRAS, 415, 3903

Vallat R., 2018, The Journal of Open Source Software, 3, 1026

Visvanathan N., Sandage A., 1977, ApJ, 216, 214

Yoo J., et al., 2022, ApJS, 261, 28

Zacharias N., Monet D. G., Levine S. E., Urban S. E., Gaume R., Wycoff G. L., 2004, in American Astronomical Society Meeting Abstracts. p. 48.15

Zackrisson E., Micheva G., Östlin G., 2009, MNRAS, 397, 2057

Zaritsky D., Kennicutt Robert C. J., Huchra J. P., 1994, ApJ, 420, 87

Zhang Y., et al., 2016, ApJ, 816, 98

Zhang Y., et al., 2019, ApJ, 874, 165

Zibetti S., White S. D. M., Schneider D. P., Brinkmann J., 2005, MNRAS, 358, 949

Zwicky F., 1933, Helvetica Physica Acta, 6, 110

Zwicky F., 1937, ApJ, 86, 217

Zwicky F., 1951, PASP, 63, 61

de Vaucouleurs G., 1960, ApJ, 131, 585

de Vaucouleurs G., de Vaucouleurs A., 1970, Astrophys. Lett., 5, 219

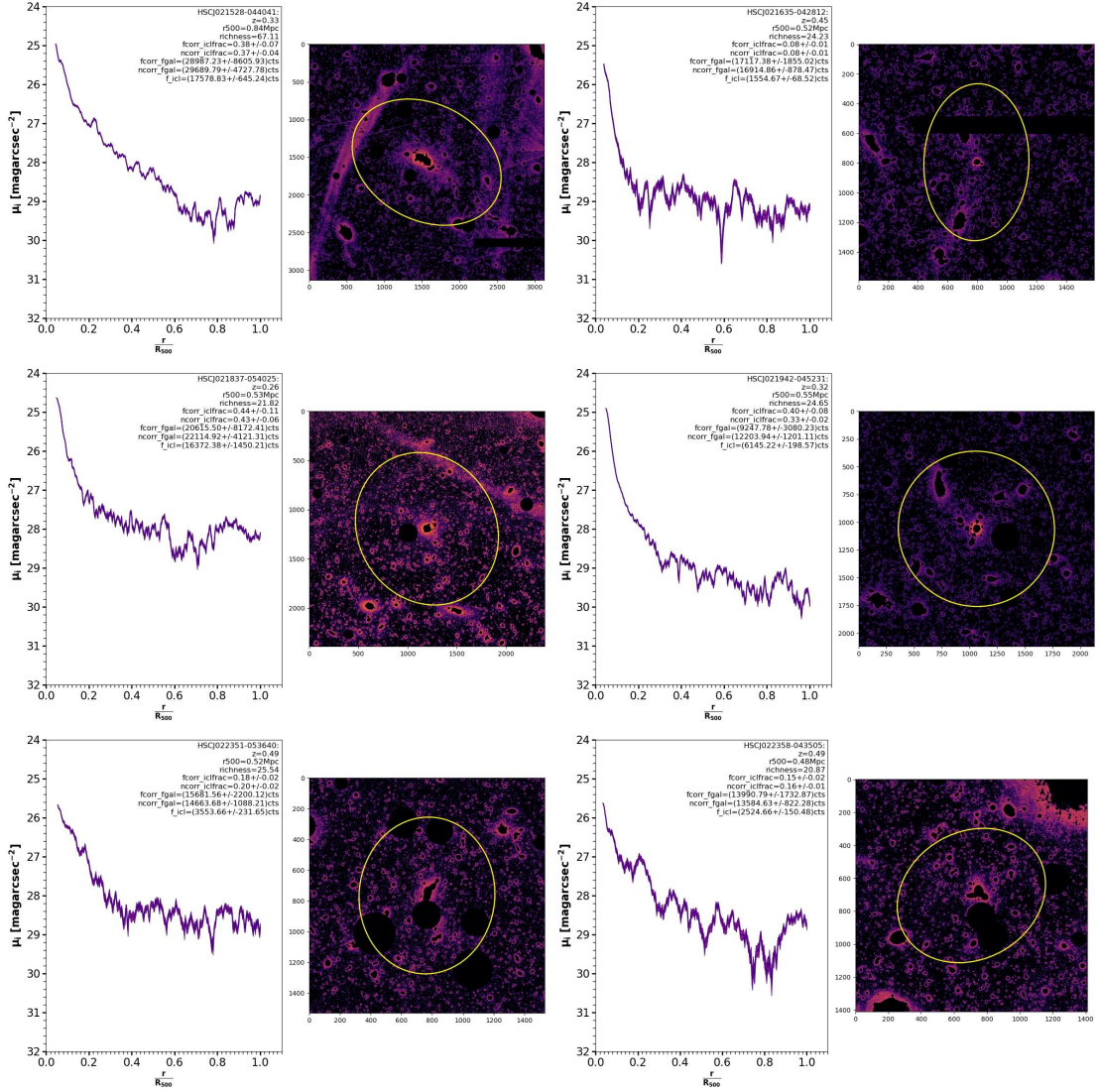# Appendices

Appendix A

Cluster ICL Profiles

A.1 XCS Sample
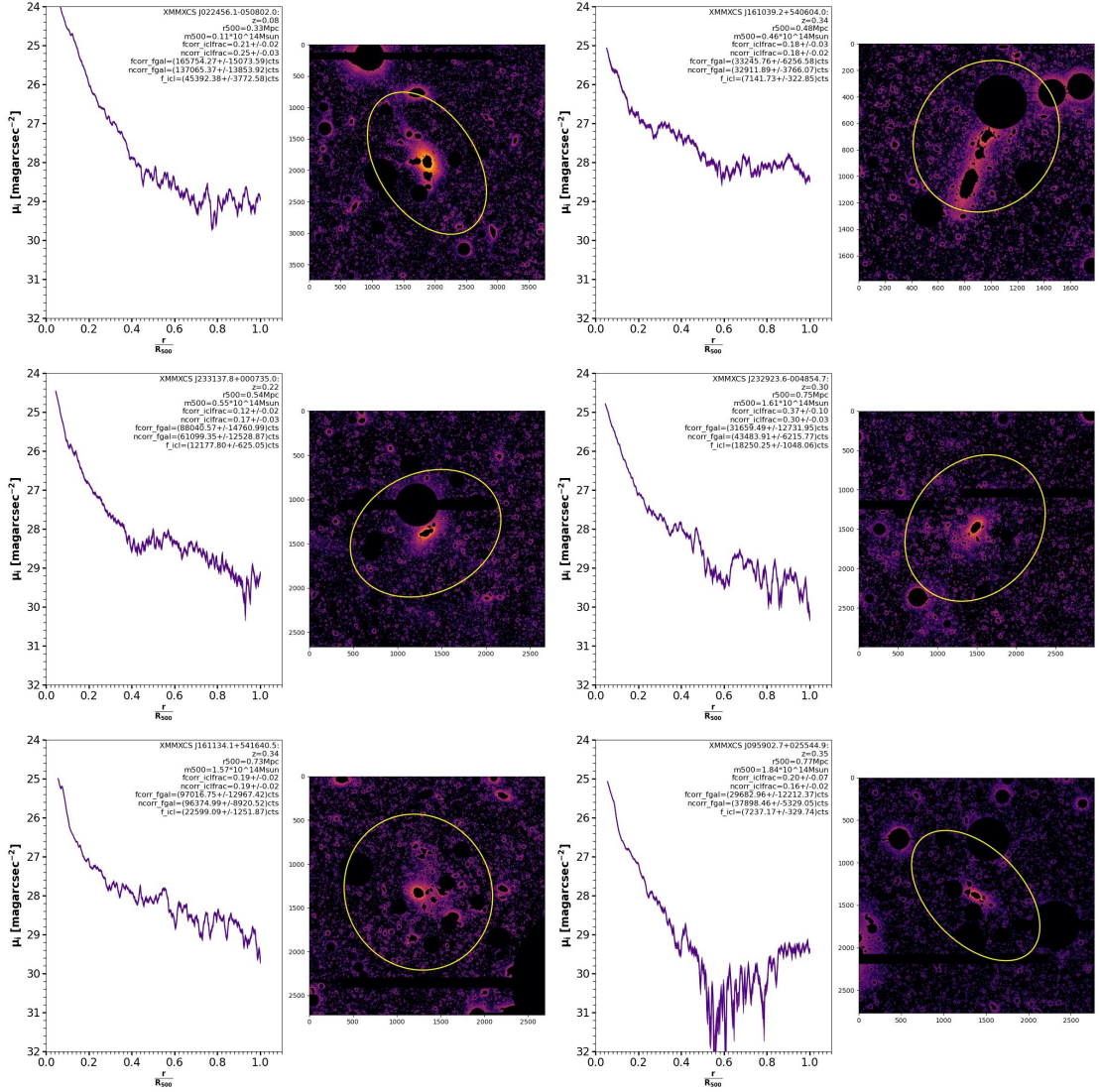
Figure A.1: The observed *i*-band ICL surface brightness profiles of the XCS clusters to the left of their respective masked image. Relevant input and output parameters are included on each plot. A yellow ellipse with the derived ICL shape parameters, going out to R_{500} is overlaid on each masked image.
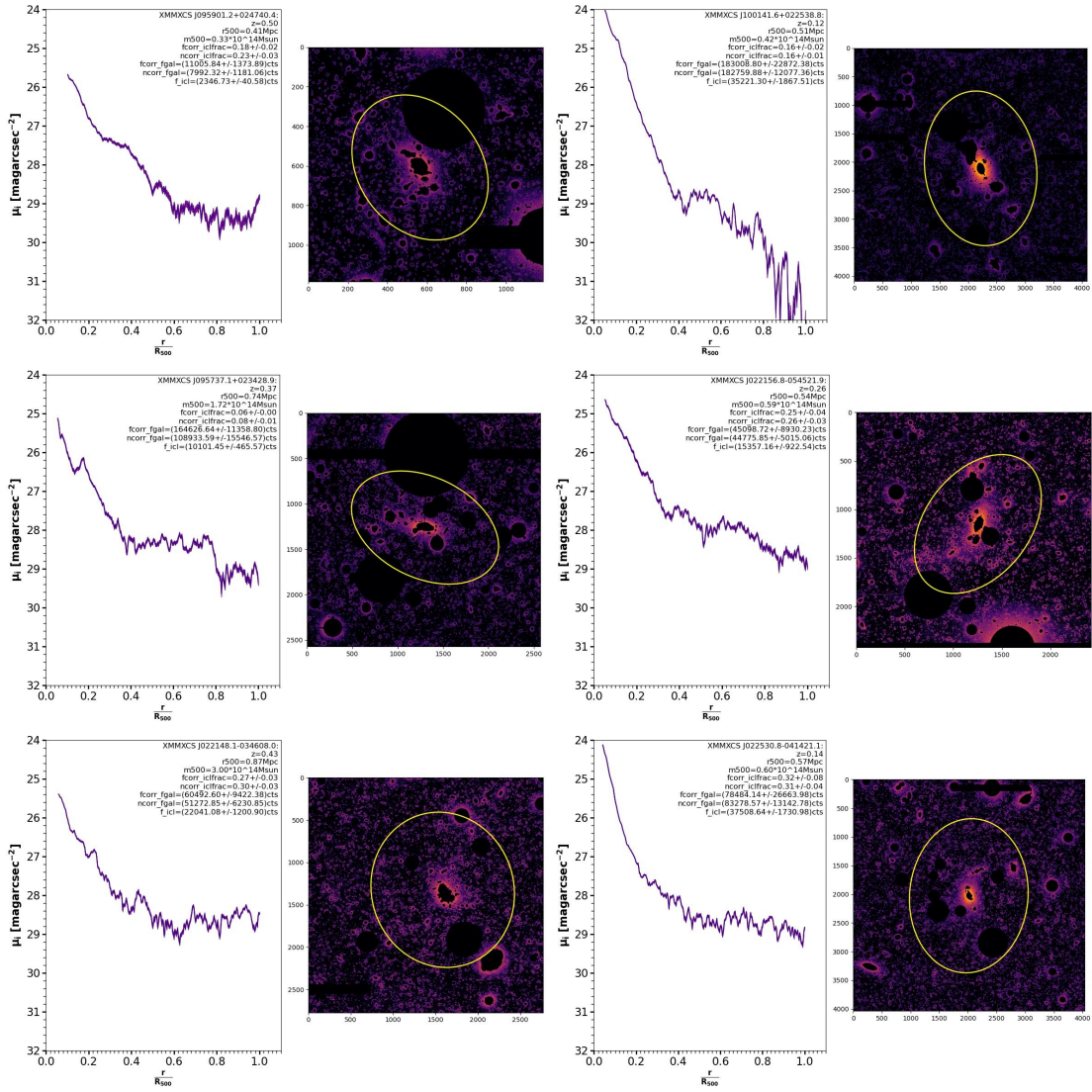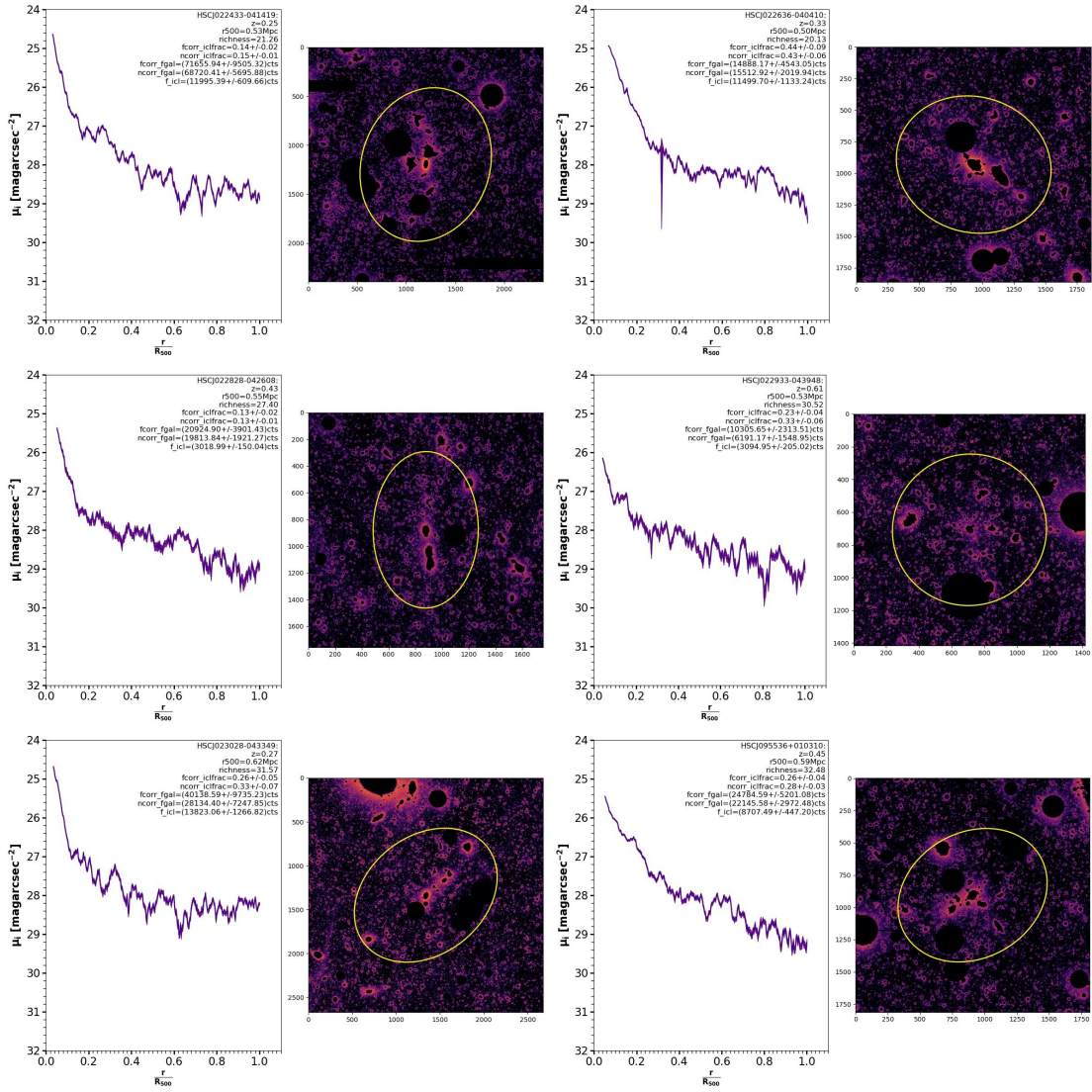
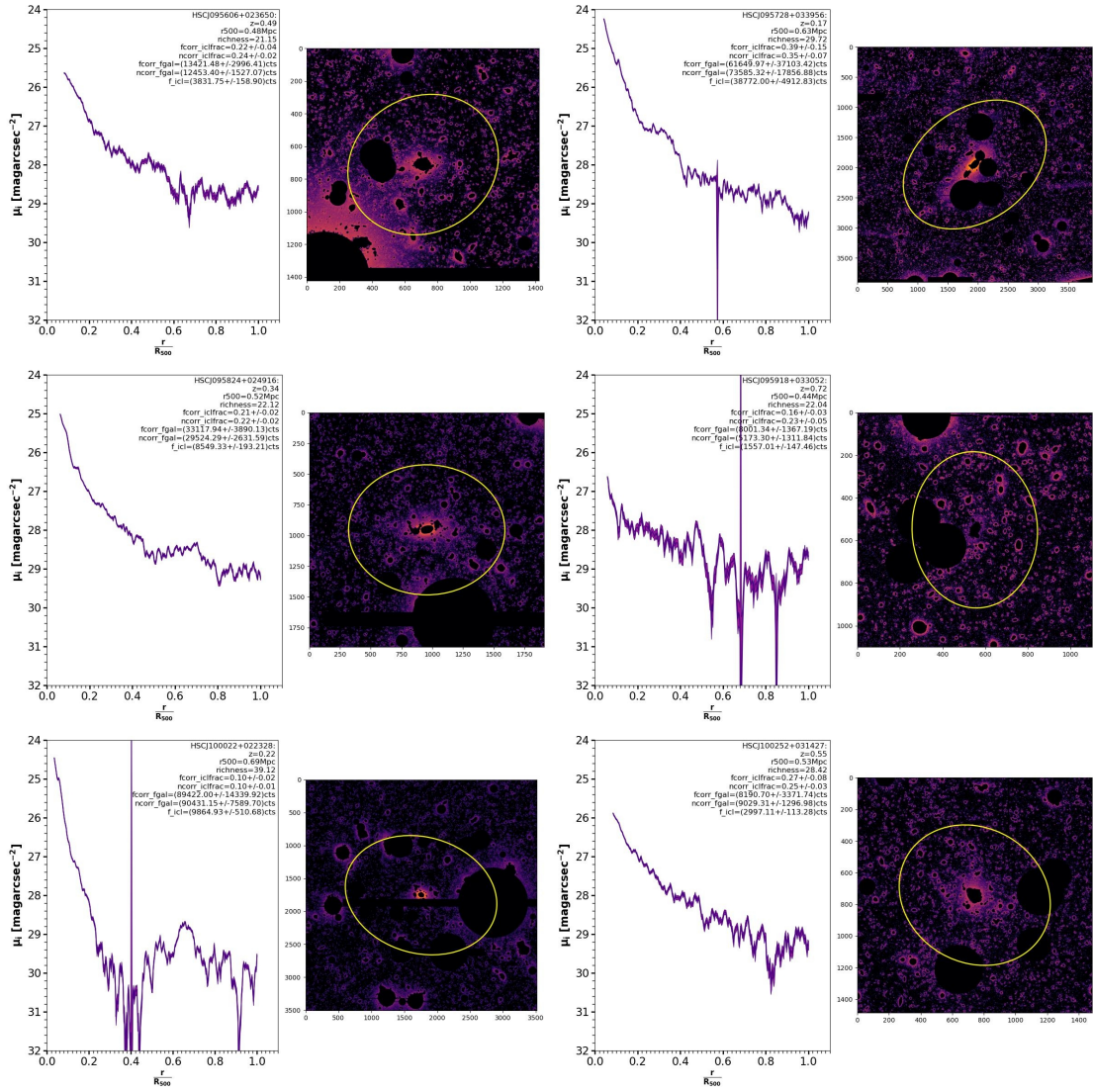**Figure A.1:** Continued from previous page.
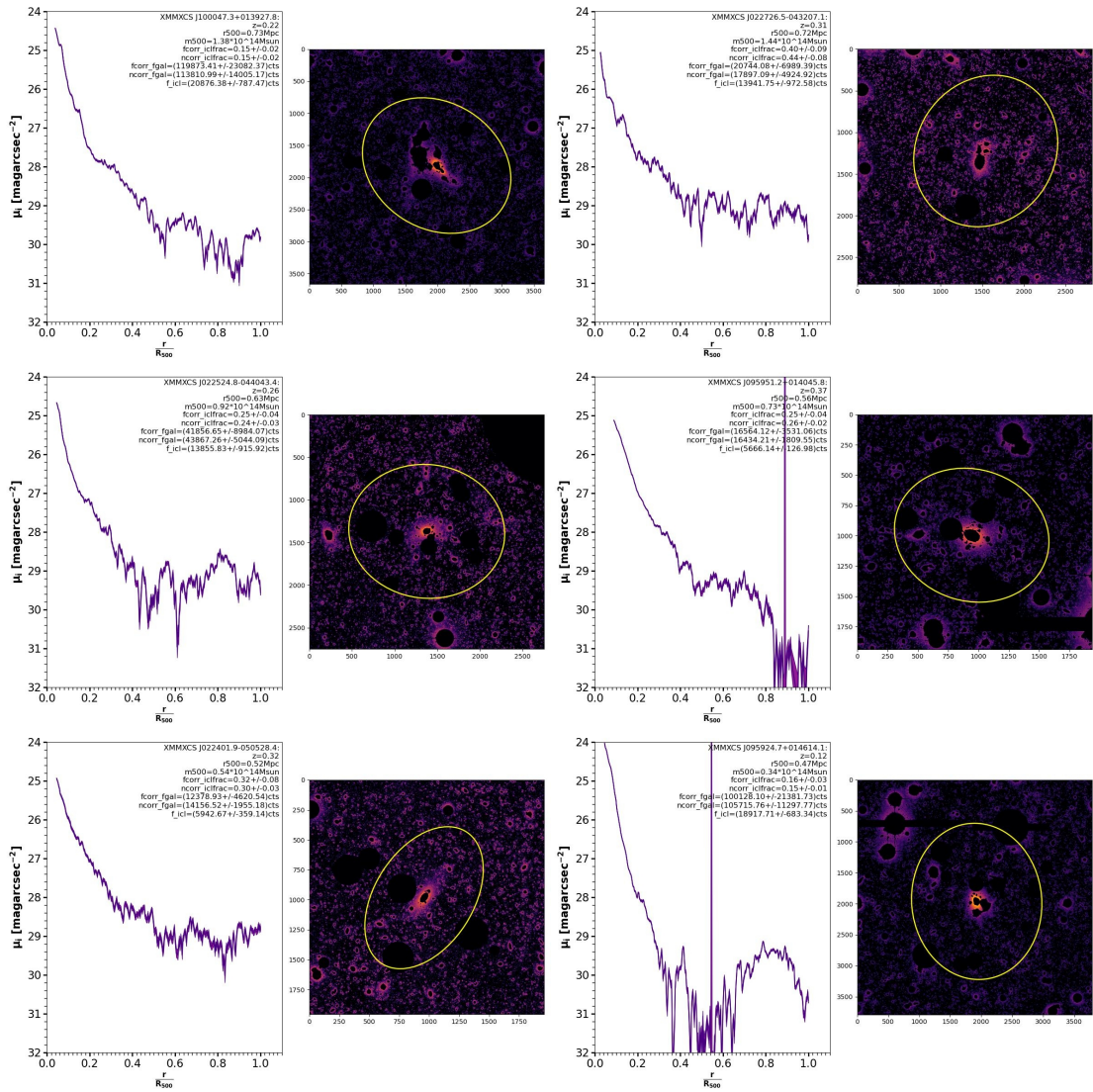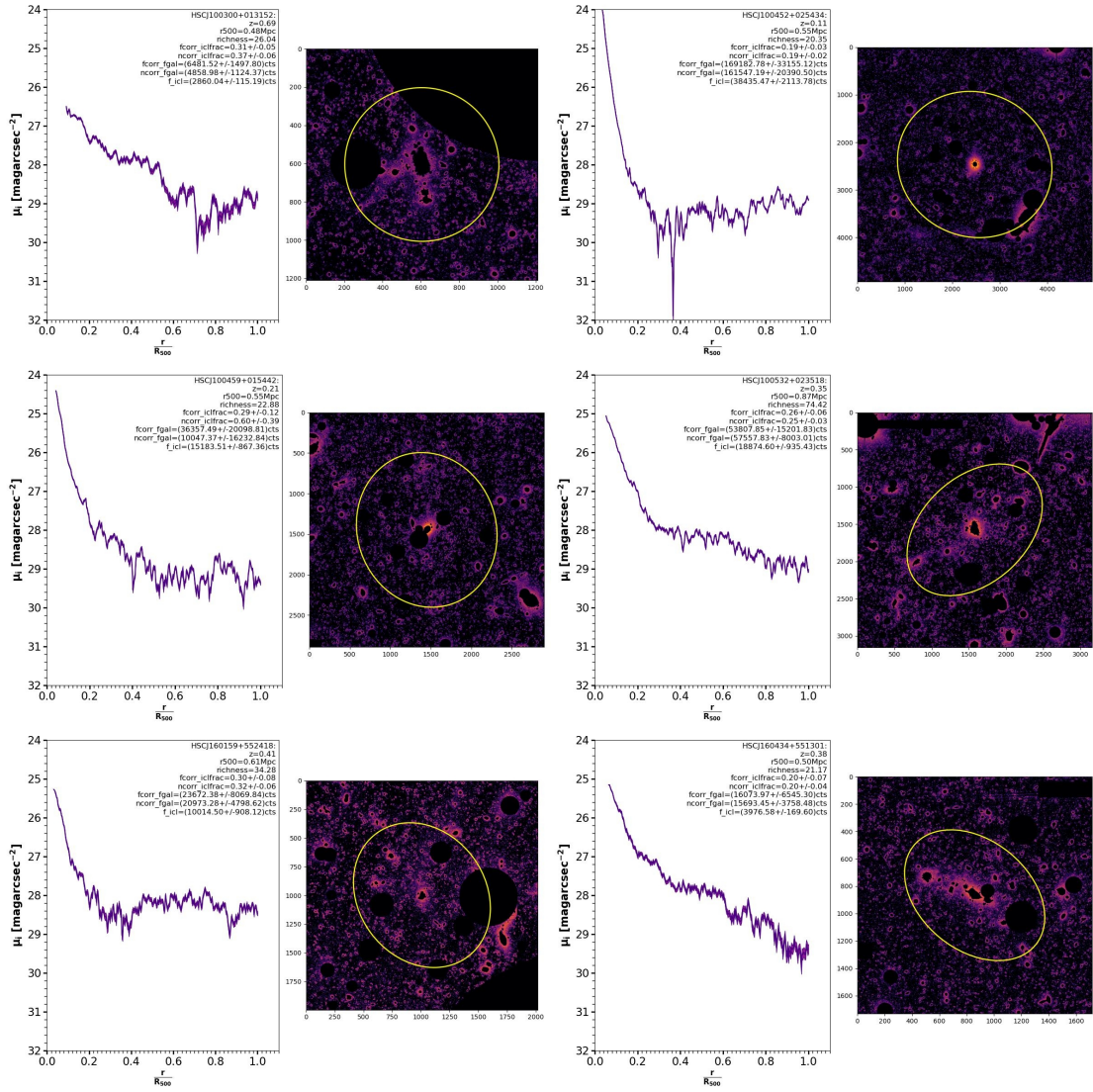
Figure A.1: Continued from previous page.

A.2 CAMIRA Sample

Figure A.2: The observed *i*-band ICL surface brightness profiles of the CAMIRA-detected clusters to the left of their respective masked image. Relevant input and output parameters are included on each plot. A yellow ellipse with the derived ICL shape parameters, going out to R_{500} is overlaid on each masked image.
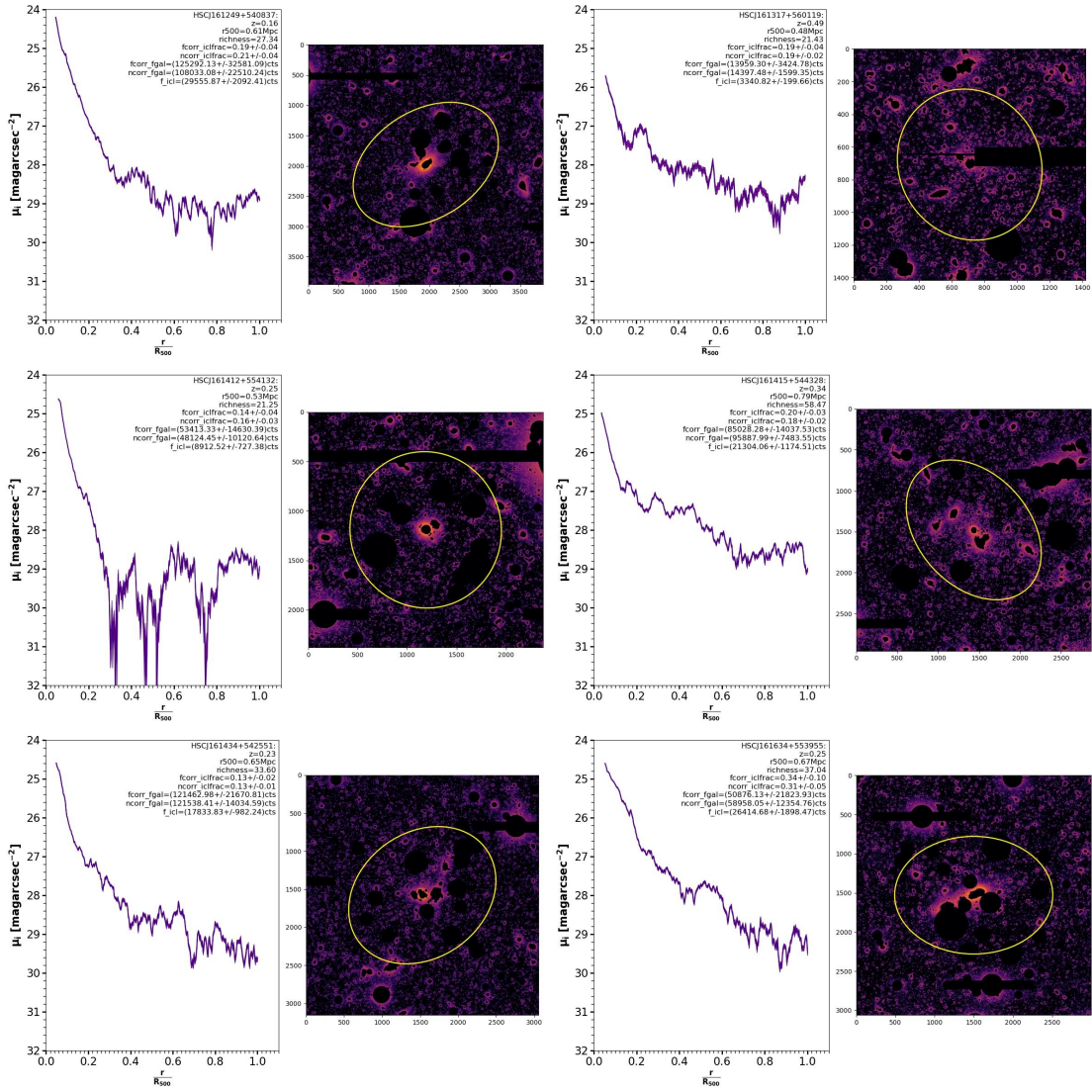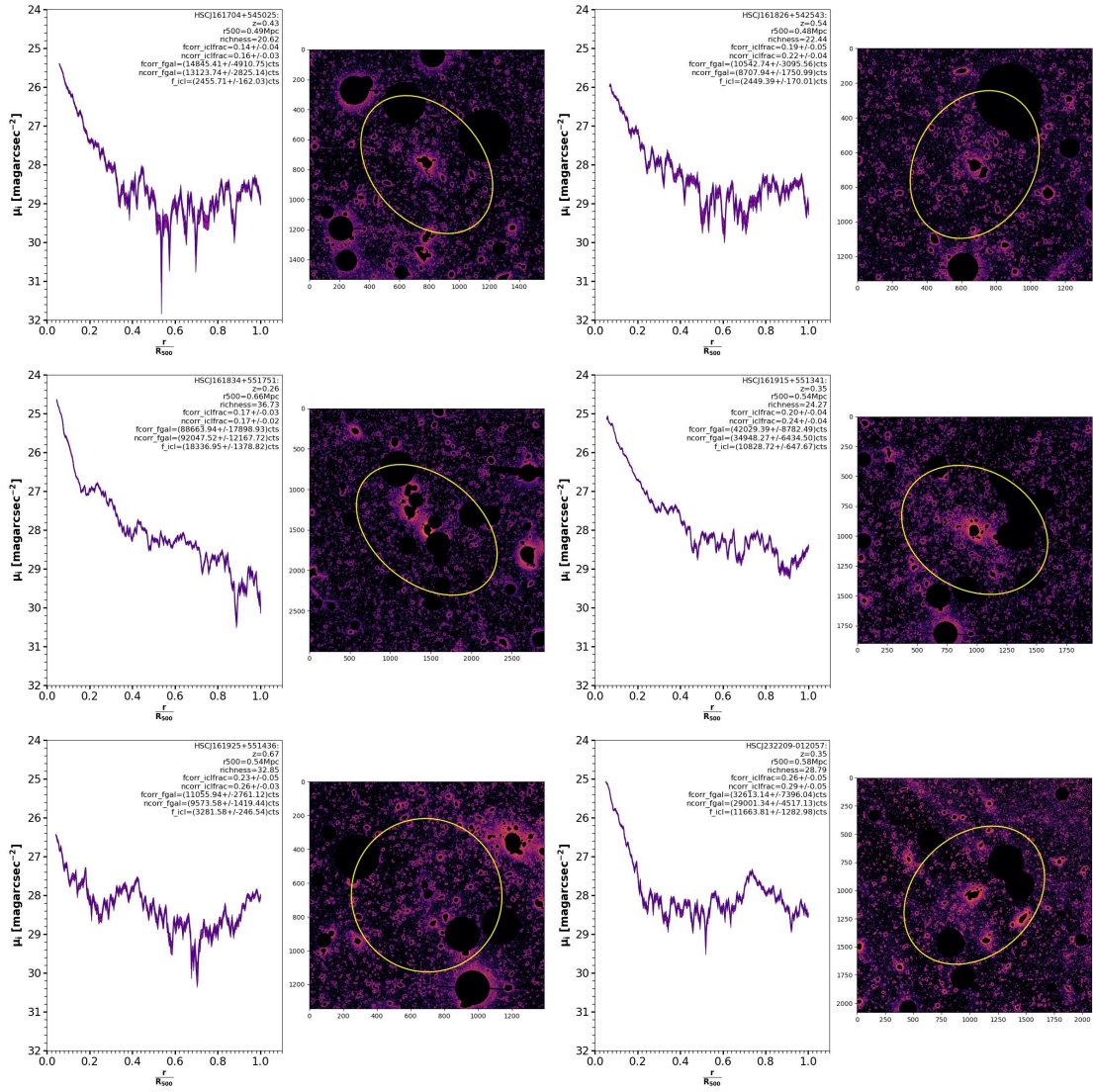
Figure A.2: Continued from previous page.

Figure A.2: Continued from previous page.

Figure A.2: Continued from previous page.

Figure A.2: Continued from previous page.

Figure A.2: Continued from previous page.

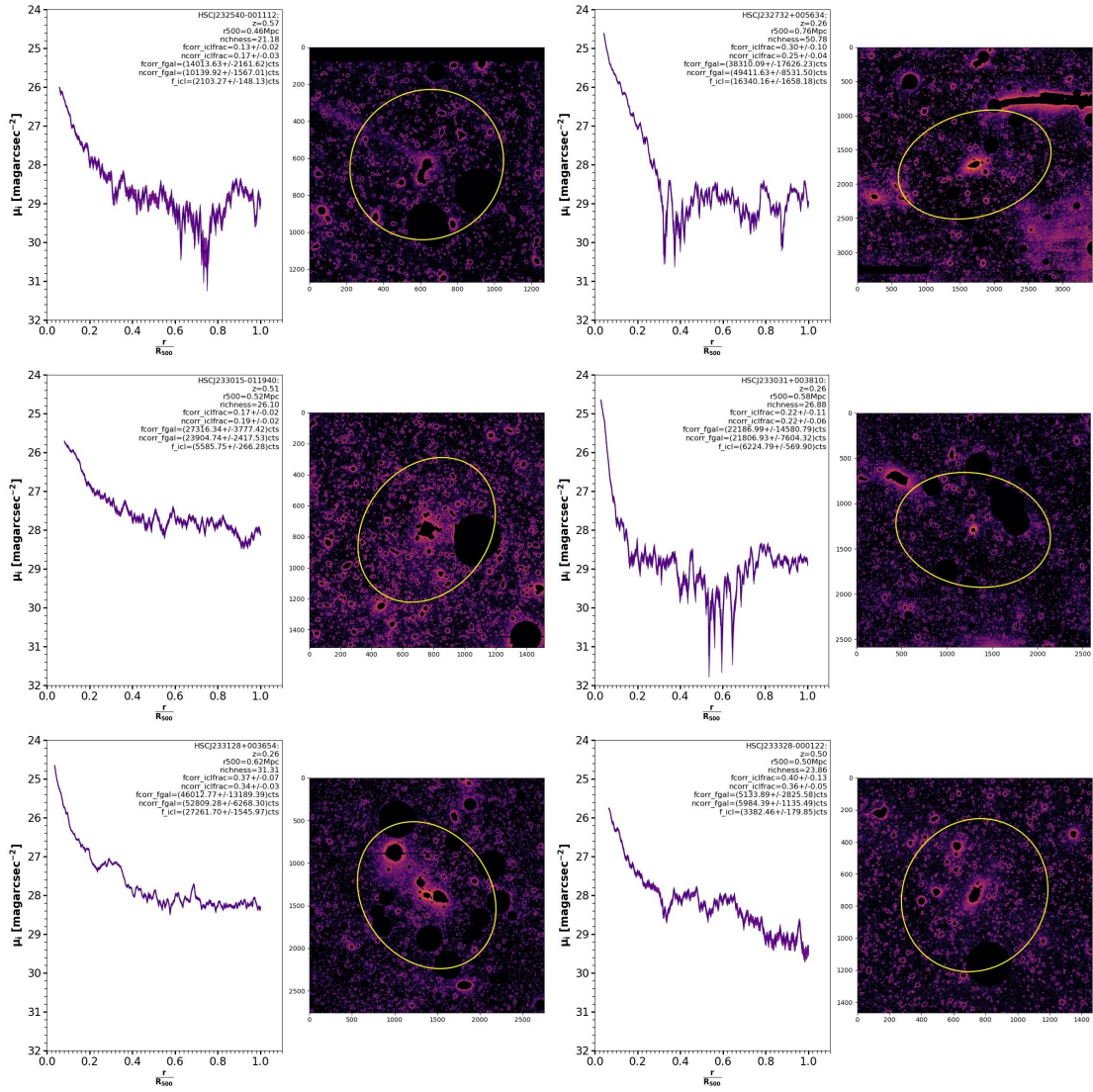**Figure A.2:** Continued from previous page.

Figure A.2: Continued from previous page.

Figure A.2: Continued from previous page.